

Development and Usage of Micro- and Nanofluidic Devices for Nanoparticle Trapping, Sorting and Biosensing

Inauguraldissertation

zur
Erlangung der Würde eines Doktors der Philosophie
vorgelegt der
Philosophisch-Naturwissenschaftlichen Fakultät
der Universität Basel

von

Deepika Sharma

von Indien

2023

Originaldokument gespeichert auf dem Dokumentenserver der Universität Basel

edoc.unibas.ch

Genehmigt von der Philosophisch-Naturwissenschaftlichen Fakultät
auf Antrag von

Fakultätsverantwortlicher: Prof. Roderick Y.H. Lim

Dissertationsleiter: Dr. Yasin Ekinici

Korreferent: Prof. Dr. Michel Calame

Basel, den 25. Mai 2021

Prof. Dr. Marcel Mayor
Dekan

Abstract

Microfluidics has revolutionized life sciences by introducing the tools to perform complex scientific studies in a simpler yet robust and reliable way. Miniaturization of bench-top processing tools using micro- and nanofluidic devices enables handling biological samples in a physiologically relevant environment to execute complex studies that were not possible before. Organ-on-a-chip, lab-on-a-chip, point-of-care diagnosis, biosensing, miniaturized PCR tools, etc., are some of the previously inconceivable examples in a portable device form. Due to the scale of the device dimensions in such microfluidic devices, small volume handling and processing have become noticeably effortless.

Among various applications of micro- and nanofluidic devices, molecular sensing, nanoparticle-separation, -sorting, -trapping, and -processing are of significant impact due to their feasibility of implementation in most of the fluidic devices. Single-particle trapping is an effective approach to study the fundamental properties of molecules in their physiological environment. Various active and passive methods exist to execute single-particle studies, such as optical tweezers, magnetic tweezers, dielectrophoretic trapping, hydrodynamic trapping, geometrical trapping, and electrostatic trapping. In the case of active methods, such as optical- and magnetic-tweezers, precise control of molecular motion is possible at the cost of a complex setup with external-force sources. However, high-throughput single-particle trapping and manipulation are not feasible in a way that can be achieved using passive methods such as geometry-induced-electrostatic (GIE) trapping and geometrical trapping.

This thesis focuses on developing integrated micro- and nanofluidic devices for 1) high-throughput contact-free electrostatic trapping of single nanoparticles and 2) size-based nanoparticle separation, -sorting, and -trapping for biosensing applications. The high-throughput single-particle trapping was achieved by developing fluidic devices utilizing the GIE trapping. A GIE-trapping fluidic device comprises nanochannels embedded with nanostructures, such as slits, cylinders, and grids. These nanostructures enable the formation of electrostatic potential traps inside the nanoindentations, forcing negatively charged nano-objects to attain a position inside them to minimize their self-energy. In conventional GIE-trapping devices, negatively charged molecules, such as DNA, viruses, and gold nanoparticles (Au NPs), can be easily trapped in the electrostatic traps.

This thesis presents the development and fabrication of GIE-trapping devices using 1) glass substrate and 2) polydimethylsiloxane (PDMS) polymer. These substrates attain a net negative surface charge density in an aqueous solution ($\text{pH} > 2$) due to the self-dissociation of terminal silanol groups. Therefore, glass- and PDMS-based fluidic devices are only usable for the confinement of negatively charged nano-objects. In this work, the scope of these fluidic devices was extended to the trapping of positively charged nano-objects by using surface modification methods for both glass- and PDMS-based fluidic devices. The surface modification of glass-based nanofluidic devices was achieved by modifying the inside of the GIE-trapping device by the adsorption of a single layer of polyelectrolyte

(poly(ethyleneimine), PEI). The PEI layer modifies the negatively charged glass surface to a positively charged surface and allows for the trapping of positively charged nanoparticles. However, the surface modifying procedure for the glass-based GIE-trapping device was demanding and required 4 to 5 days. To have an efficient surface modification process, PDMS-based GIE-trapping devices were introduced.

The introduction of PDMS-based fluidic devices for positively charged nano-objects has improved the throughput for device fabrication and surface modification. Furthermore, two-polyelectrolyte layers (1: poly(ethyleneimine) and 2: poly(styrenesulfonate)) deposition is presented in this work using PDMS-based devices to demonstrate the possibility of achieving homogeneously charged surface using multi-polyelectrolyte layers. The efficiency of these devices with surface charge reversal was comparable to native GIE-trapping devices, demonstrating the successful and homogeneous surface modification.

The trapping efficiency and device performance of a GIE-Trapping device rely on the geometry of the device and the interaction between the charged particle and the device surface. Therefore, extensive optimization of the device geometry is essential to achieve efficient GIE trapping in a fluidic device. In this work, two different approaches, 1) charged particle inclusive simulation and 2) point charge approximation simulation, are presented to optimize the geometrical parameters of a GIE-trapping device numerically. To compare numerical results with experimental data, a cylindrical nanopocket design was used to represent a nanotrap to confine a charged gold nanoparticle.

The charged-particle inclusive simulations are demanding, but provide more accurate results for attainable particle stiffness constant using crucial geometrical parameters of the device, size and charge of the particle of interest, and the salt concentration of the solution. Comparatively, point-charge approximation simulations are faster and give appropriate results of particle trapping stiffness constant, residence time, etc. Here, point-charge approximation simulations are used for efficiently identifying the trends of trapping strength of a device based on critical geometrical parameters, i.e., the height of the nanochannel and the nanopocket and the diameter of the nanopocket. The point charge approximation simulations demonstrated that the trapping strength of a particle inside a nanotrap could be enhanced by increasing the trap height or reducing the channel height. Additionally, the trapping strength of a nanotrap can be modified by changing the diameter of the nanopocket; however, reduction or enlargement of the pocket diameter from the optimum diameter reduces the trapping strength of the nanotrap. For effective GIE trapping, it is important to use a solution with low ionic or salt concentration ($< 0.5\text{mM}$ for trapping stiffness constant $> 10^{-4}$ pN/nm) in order to avoid screening of the electrostatic field from the charged device surface. A detailed comparison of both approaches, numerical calculations, and experimental results are presented, demonstrating their advantages and disadvantages.

While there are many advantages of GIE-trapping devices for molecular trapping, one major disadvantage is the reduced functionality of the devices for body fluids that contain high salt concentrations. Due to the high ionic concentration in the body fluids, the electrostatic effect

of the charged device surface gets screened, leading to no potential trap for the confinement of charged nano-objects. Therefore, a new design of the fluidic device is developed for biosensing applications that can use body fluids to extract the target molecules for molecular sensing. The fluidic device exploited geometrical sieving, deterministic lateral displacement (DLD) arrays, and geometrical trapping for particle separation, sorting, and trapping, respectively. The separation of unwanted macro- and micro-particles was achieved in the separation chamber, followed by the size sorting of target-molecule-adsorbed nanoparticles and, later, the size-based trapping of these nanoparticles in the detection area. The motion of the solution and nanoparticle throughout the device was observed using interferometric scattering detection (iSCAT) microscopy, whereas, for molecular sensing, Raman spectroscopy was used at the detection area to achieve a few pg/ml detection limit. The device has the potential for applications in early multi-disease diagnosis for diseases that can be detected using antigen-antibody complex formation on antibody-coated nanoparticles.

The presented GIE-trapping devices can be used to achieve high-throughput single-nanoparticle trapping, whereas geometrical particle trapping devices can be used to perform size-selective nanoparticle trapping for molecular sensing. Both methods are effective for studies conducted in an aqueous environment and have the potential to be used in molecular studies, disease diagnosis, biological studies, etc., for research and commercial purposes. Demonstrated device fabrication methods and surface modification procedures allow improved productivity and yield of the GIE-trapping devices. The device geometry of a GIE-trapping device can be optimized further using the presented numerical calculations. Therefore, the work presented here advances the research in the field of GIE trapping and geometrical trapping and opens up new possibilities for both basic and applied research in several fields, such as biophysics, molecular dynamics, diagnostics, and molecular detection.

Declaration

Self-Citations

Five research papers were published from my doctoral work at the University of Basel and the Paul Scherrer Institut, one European patent application was accepted, and one manuscript was recently accepted. All three first-author papers and patented work are implemented in this thesis as separate chapters.

Chapter 3

This chapter is a transcript of the published manuscript: *Single positively charged particle trapping in nanofluidic systems*, **D. Sharma**, M. A. Gerspach, T. Pfohl, R. Y. H. Lim, Y. Ekinci, *Microelectronic Engineering* **175**, 43-49, (2017).

Chapter 4

This chapter is a transcript of the accepted manuscript: *Surface-Modified Elastomeric Nanofluidic Devices for Single Nanoparticle Trapping*, **D. Sharma**, R. Y. H. Lim, T. Pfohl, Y. Ekinci, *Microsystems & Nanoengineering*, (2021).

Chapter 5

This chapter is a transcript of the published manuscript: *Optimization of Nanofluidic Devices for Geometry-Induced Electrostatic Trapping*, **D. Sharma**, R. Y. H. Lim, T. Pfohl, Y. Ekinci, *Particle & Particle Systems Characterization* **38** (2), (2021).

Chapter 6

This chapter focuses on an initial prototype of an integrated microfluidic device for microparticle separation and nanoparticle trapping for molecular detection. The work is patented as *Device and Method for Size-Selective Particle Separation, Trapping, and Manipulation of Micro and Nanoparticles for Molecular Detection*, **D. Sharma**, Y. Ekinci, European Patent Application, EP19192141, (2019).

Individual Contributions

D. Sharma fabricated integrated micro- and nanofluidic devices, designed and performed experiments and simulations, analyzed and illustrated data, wrote the thesis, patent application, and manuscripts, and co-authored three other manuscripts.

T. Pfohl and Y. Ekinci assisted in experimental designs, discussed results, and co-authored publications.

R. Y. H. Lim assisted in experimental designs and initial learning on biomimetic nuclear pore complexes using protein patterning. Additionally, he co-authored publications on nanofluidic devices.

M. A. Gerspach assisted in the fabrication of fluidic devices and co-authored publications. Further, M. A. Gerspach co-wrote the following manuscripts, performed the experiments, and analyzed and illustrated data related to the following manuscripts.

1. *Nanofluidic Lab-on-a-chip Trapping Devices for Screening Electrostatics in concentration gradients*, M. A. Gerspach, N. Mojarad, **D. Sharma**, T. Pfohl, Y. Ekinici, *Microelectronic Engineering*, **175**, 17-22 (2017).
2. *Soft Electrostatic Trapping in Nanofluidics*, M. A. Gerspach, N. Mojarad, **D. Sharma**, T. Pfohl, Y. Ekinici, *Microsystems & Nanoengineering* **3**, 17051 (2017).
3. *Pneumatically Controlled Nanofluidic Devices for Contact-Free Trapping and Manipulation of Nanoparticles*, M. A. Gerspach, N. Mojarad, **D. Sharma**, Y. Ekinici, T. Pfohl, *Particle & Particle Systems Characterization*, 1800161, (2018).

Table of Contents

ABSTRACT.....	III
DECLARATION.....	VII
ABBREVIATIONS.....	XI
CHAPTER 1. INTRODUCTION	13
CHAPTER 2. NANOPARTICLE TRAPPING, TRACKING AND DETECTION IN FLUIDIC DEVICES.....	19
2.1 GEOMETRY-INDUCED ELECTROSTATIC TRAPPING INSIDE A FLUIDIC DEVICE	19
2.2 PARTICLE TRACKING USING INTERFEROMETRIC SCATTERING DETECTION TECHNIQUE	21
2.3 ISCAT PRINCIPLE.....	21
2.4 ISCAT SETUP.....	23
2.5 ISCAT DATA PROCESSING.....	24
2.6 NUMERICAL SIMULATIONS FOR GIE-TRAPPING DEVICES	26
2.7 FINITE ELEMENT METHOD AND COMSOL.....	27
2.8 PRINCIPLE OF DLD ARRAYS FOR DIRECTIONAL PARTICLE MOTION	28
2.9 PRINCIPLE OF RAMAN SPECTROSCOPY AND ITS USAGE FOR MOLECULAR DETECTION	30
2.9.1 Raman Spectroscopy	30
2.9.2 Surface-enhanced Raman Spectroscopy	31
CHAPTER 3. SINGLE POSITIVELY CHARGED PARTICLE TRAPPING IN NANOFUIDIC SYSTEMS	33
3.1 INTRODUCTION	34
3.2 MATERIAL AND METHODS	37
3.2.1 Fabrication of glass-glass-based GIE-trapping device.....	37
3.2.2 Functionalization of GIE-trapping devices.....	40
3.2.3 Sample preparation.....	42
3.2.4 Experimental setup.....	42
3.3 RESULTS AND DISCUSSION	42
3.3.1 Trapping negatively charged particles	42
3.3.2 Trapping positively charged particles.....	44
3.4 CONCLUSIONS.....	46
CHAPTER 4. SURFACE-MODIFIED ELASTOMERIC NANOFUIDIC DEVICES FOR SINGLE NANOPARTICLE TRAPPING.....	49
4.1 INTRODUCTION	50
4.2 MATERIALS AND METHODS	52
4.2.1 Device Patterning and Replica Molding	52
4.2.2 Particle Sample Preparation.....	54
4.2.3 Non-functionalized PDMS Device	55
4.2.4 Functionalized PDMS Device.....	55
4.2.5 Particle Detection and Tracking	57
4.3 RESULTS.....	58
4.3.1 Electrostatic Single Particle Trapping	58
4.3.2 Single to multiparticle trapping.....	63
4.3.3 Experimental comparison for functionalized and nonfunctionalized devices.....	64
4.4 DISCUSSIONS	67
CHAPTER 5. OPTIMIZATION OF NANOFUIDIC DEVICES FOR GEOMETRY-INDUCED ELECTROSTATIC TRAPPING	69

Table of Contents

5.1 INTRODUCTION	70
5.2 THEORY	72
5.3 PARAMETRIC STUDY OF GIE TRAPPING.....	73
5.3.1 <i>Point-Charge Approximation Simulation Results</i>	75
5.3.2 <i>Particle Inclusive Simulation Results</i>	80
5.4 CONCLUSIONS.....	83
5.5 ACKNOWLEDGMENTS	83
5.6 SUPPORTING INFORMATION	84
5.6.1 <i>Optimal pocket diameter for stiffer particle trapping</i>	84
5.6.2 <i>Impact of particle surface charge on stiffness constant</i>	84
5.6.3 <i>Difference between experimental and numerical results from particle-based simulations</i>	85
CHAPTER 6. NANOFUIDIC DEVICES FOR PARTICLE TRAPPING AND MOLECULAR SENSING	87
6.1 INTRODUCTION	87
6.2 MATERIALS AND METHODS	89
6.2.1 <i>Device Design</i>	89
6.2.2 <i>Device Development</i>	90
6.2.3 <i>Experiment Preparation</i>	92
6.2.4 <i>Optical Detection</i>	93
6.3 RESULTS AND DISCUSSIONS	93
6.3.1 <i>Micro-Particle Separation</i>	93
6.3.2 <i>Nanoparticle Directed Displacement</i>	93
6.3.3 <i>Nanoparticle Size-based Trapping</i>	94
6.3.4 <i>Molecular Sensing</i>	95
6.4 CONCLUSIONS.....	97
CHAPTER 7. CONCLUSIONS AND OUTLOOK	99
7.1 CONCLUSIONS AND PROSPECTIVE APPLICATIONS OF ELECTROSTATIC TRAPPING.....	99
7.2 CONCLUSIONS AND PROSPECTIVE APPLICATION OF GEOMETRICAL TRAPPING.....	101
BIBLIOGRAPHY.....	105
PUBLICATIONS	123
ACKNOWLEDGEMENTS.....	125
CURRICULUM VITAE	127

Abbreviations

2D	Two-dimensional
3D	Three-dimensional
AO	Analog output
Au NPs	Gold nanoparticles
BC	Boundary condition
BOE	Buffered oxide etch
COC	Cyclic olefin copolymer
Cr	Chromium
CV	Coefficient of variation
DI	Deionized
DLD	Deterministic lateral displacement
E-beam	Electron beam
EDL	Electric double layer
FEA	Finite element analysis
FEM	Finite element method
GC	Gouy-Chapmann
GIE	Geometry-induced electrostatic
HGP	Human genome project
IPA	Isopropyl alcohol
iSCAT	Interferometric scattering detection
LD	Lateral displacement
LoC	Lab on a chip
LSPR	Localized surface plasmon resonance
MIBK	Methyl-isobutyl-ketone
MSD	Mean square displacements
MWR	Method of weighted residuals
N₂	Nitrogen
NA	Numerical aperture
ND	Neutral density
NPs	Nanoparticles
OD	Optical density
PB	Poisson-Boltzmann
PC	Polycarbonate
PDE	Partial differential equation
PDMS	Poly(dimethylsiloxane)
PEI	Poly(ethyleneimine),
PET	Polyethylene terephthalate
PMMA	Poly-(methylmethacrylate)
PS	Polystyrene
PSS	Poly(styrenesulfonate)

Abbreviations

RCF	Relative centrifugal force
RIE	Reactive ion etching
SERS	Surface-enhanced Raman spectroscopy
UV	Ultraviolet
ZZ	Zigzag

Chapter 1. Introduction

Microfluidics deals with fluidic systems with critical dimensions between 100 nm and 1 mm^{1,2}, where the factors such as surface tension^{3,4}, capillary force⁵⁻⁷, energy dissipation, fluidic resistance⁸, and molecular diffusion⁹ dominate the behavior of the fluid. These dominating forces and increased surface-to-volume ratio are exploited in microfluidics to drive fluids without pumps and to achieve faster reaction rates⁹, separation of different liquids^{4,10}, predictable laminar flow⁸ based mathematical modeling, rapid molecular diffusion¹¹, rapid thermal transport¹², and Dean flow^{13,14}.

Emerging from the field of manufacturing technologies for semiconductors², microfluidics has significantly impacted life sciences and has revolutionized this field. The first working demonstration of a microfluidic device dates back to 1965 when Richard Sweet introduced inkjet printing¹⁵. Later in 1977, Bassous et al.¹⁶ showed the large-scale manufacturing potential of microfluidic devices using then-established semiconductor device manufacturing techniques – photolithography and etching. After the initial work towards the development of microfluidic valves¹⁷⁻²¹ and pumps²²⁻²⁴, microfluidics attracted significant interest from various frontiers, mainly for portable biological and chemical detection devices^{2,25} that led to an increased focus on the development of functional and integrated microfluidic devices²⁶. With the inception of the Human Genome Project (HGP)²⁷ in 1990 aiming to sequence the entire human genome, researchers focused on factors such as availability and cost of material, the viability of manufacturing processes and techniques for mass production, portability of the device, detectability through or within a microfluidic device, and bonding of substrate to achieve a 3D device. The 13-year period of the project played a pivotal role in advancing the microfluidics field and establishing the usefulness of microfluidic devices with a wide range of functionality that can also be used in other applications.

Initially, silicon was the primary material that was used for microfluidic devices; however, due to its opaque nature, high cost, brittle nature, complex silicon-silicon bonding process, and unavailability to researchers of all disciplines, glass came as a better alternative that can be processed using similar techniques as used in the microelectronics industry. Furthermore, the optical transparency of glass substrates enabled the integration of the light-based detection methods with the microfluidic devices²⁸⁻³¹. However, with the increased demand for a cheaper material that allows for simpler manufacturing of fluidic devices, the elastomeric material poly(dimethylsiloxane) (PDMS), first used by G. Whiteside et al.^{32,33}, quickly became popular in the field. PDMS-based device production is simpler because it requires a patterned master that can be used for pattern transfer to PDMS using replica molding techniques. In replica molding, structures down to sub-100 nm can be cast with ease in the PDMS substrates³⁴. Additionally, PDMS is soft and elastic to give tunability for valves and pumps, and it is easier to bond with PDMS, glass, and many other materials to seal the PDMS-based fluidic devices³⁵⁻³⁸. Chemically, PDMS is permeable to gases, making it a popular choice for microfluidic device manufacturing for live-cell studies³⁹⁻⁴². Therefore, PDMS has been widely used in various research fields to develop complex and sophisticated microfluidic analytical

systems³². The transition of these devices to market has been a struggle due to the a priori requirement of cleanroom fabrication facilities and fabrication processes that are not scalable to meet commercial demand for cost-effectiveness and high throughput capacity. However, to achieve high throughput capacity and reduced production cost, several techniques, such as embossing^{43,44}, nanoimprint lithography, rapid prototyping, and micro-injection molding^{45,46}, have been developed using different elastomeric materials, including UV curable PDMS and thermoplastics such as poly(methyl methacrylate) (PMMA), polycarbonate (PC), polystyrene (PS), cyclic olefin copolymer(COC), polyethylene terephthalate (PET).^{1,2,47,48}

Many of the developed microfluidic device manufacturing techniques are capable of producing structures on the nanometer scale.^{44,48-50} Thus, to expand the applicability of microfluidic systems for nano-object handling and analysis, integrated micro- and nanofluidic devices are developed, which include nanostructures with at least one characteristic dimension less than 100 nm.⁵¹⁻⁵⁴ In nanofluidics, the relevant dimension of nanostructures is kept in the order of the range of the surface and interfacial forces in liquids. At the nanoscale, additional forces, such as electrostatics, van der Waals, and steric interactions, become dominant to drive the physics of the processes for fluid and nanoparticle transport and interactions.⁵⁵⁻⁵⁷ This makes the nanofluidic systems an ideal platform for investigating fundamental physical and chemical phenomena such as concentration polarization⁵⁸⁻⁶², nanocapillarity and negative pressure^{63,64}, nonlinear electrokinetic flow and ion focusing^{65,66}, electrical double layer overlap^{54,57}, and mass transport in geometrically confined spaces⁶⁷. Furthermore, exploiting these fundamental properties of nanofluidics, researchers have developed various platforms with nanopores, nanochannels, and nanoslits for several applications, such as the transport of ions and biomolecules through confined space^{65,68-70}, single molecule analysis⁷¹, entropic trapping of biomolecules^{72,73}, DNA electrophoresis⁷², and molecular pre-concentration^{62,74}.

Integration of micro- and nanofluidics has played a significant role in the development of tools and systems for various applications and studies, such as protein analysis⁷⁵, DNA-protein interaction^{76,77}, particle sorting and separation⁷⁸⁻⁸¹, single particle trapping⁸²⁻⁸⁵, molecular sensing⁶⁵, and cell screening^{10,86}. Additionally, integrated fluidic devices have expanded the applicability of the fluidic devices towards the direction of handling nanoscale objects, such as proteins⁷⁷, viruses⁸⁷, DNA⁸⁸⁻⁹¹, vesicles^{92,93}, nanoparticles, and nanorods⁹⁴.

In recent years, particle trapping and sensing have become focal areas of research in the field of micro- and nanofluidics. Mostly existing integrated micro/nanofluidic devices are miniaturized versions of existing bench-top processes allowing efficient and faster processing of small sample volumes in a sterilized environment to avoid contamination during the sample processing. By integrating the fluidic devices with measuring, sensing, and actuating components, the devices are used in disease detection and diagnosis⁹⁵⁻⁹⁹, food testing⁹⁵, memory storage¹⁰⁰⁻¹⁰², security tags¹⁰³, digital sample processing^{104,105}, and molecular analysis¹⁰⁶⁻¹⁰⁸.

To perform particle trapping and sensing at the single molecular level, researchers have developed both active and passive nanofluidic devices; for active devices, fluidic systems are coupled with laser, magnetic fields, electric field, etc., to trap single nano-objects using the force field gradients, whereas passive devices use hydrodynamic forces, electrokinetics, and electrostatic forces generated at the nanoscopic level by the design and surface charge of the fluidic device surface. While active fluidic devices require a complex setup, passive integrated fluidic devices are advantageous in manufacturing cost and design simplicity.

This thesis reports on the high-throughput passive integrated micro- and nanofluidic devices for single nanoparticle trapping and sorting to allow device applications for molecular sensing, early disease diagnosis, and new drug discovery. To carry out the trapping of nanoparticles, two different approaches are used: (1) geometry-induced electrostatic (GIE) trapping and (2) size-selective geometrical trapping. GIE-trapping devices exploit the electrostatic interaction between a charged nano-object and the charged device surface to achieve contact-free trapping of a charged nano-object. Generally, a GIE-trapping device contains nanochannels with nanoindentations in the form of nanopockets, nanogrids, or nanoslits that allow the formation of a potential well in each nanoindentation where a charged nano-object can get trapped due to the electrostatic repulsive forces between charged device walls and the nano-object.

GIE trapping allows high-throughput contact-free confinement of single nanoparticles individually. In contrast, size-selective geometrical trapping provides for the confinement of multiple nanoparticles of the same size at a predetermined location to achieve enhanced signal from trapped nano-objects. Both approaches have their benefits according to the use of the devices. GIE trapping provides an opportunity to analyze a large population of isolated confined nano-objects, creating opportunities to capture their dynamic, chemical, biological, and statistical information. It also opens up the possibility of carrying out molecular-molecular interaction studies. On the other hand, size-selective geometrical trapping focuses on the size-based nanoparticle sorting and collection of same-sized particles at the same location, which helps to collect enhanced signals from all trapped nanoparticles and can be used for molecular sensing.

As part of this work, novel GIE-trapping devices were developed to widen the scope of their applicability. Their performance was examined quantitatively through experiments using gold nanoparticles (Au NPs). The development of GIE-trapping devices for negatively charged nanoparticle trapping using silicon and glass substrates had been demonstrated earlier.^{94,109-113} The devices were designed to harness the electrostatic forces of the device surface for the contact-free trapping of charged single nanoparticles. In earlier studies, only negatively charged particles were used for single particle trapping due to the intrinsic nature of the used substrates that lead to a negatively charged surface on the device owing to its contact with an aqueous solution.¹¹⁴⁻¹¹⁸ Therefore, new glass-based integrated nanofluidic devices were developed and processed with a surface modification procedure using polyelectrolytes to overcome this constraint and employ the technology for positively charged nanoparticles. The modified surface provided a positively charged surface in the nanofluidic device and enabled

contact-free trapping of positively charged nanoparticles. Using the developed devices, we demonstrated the successful confinement of positively charged 60 nm diameter Au NPs. A comparative study is presented in this thesis, demonstrating the trapping of positively and negatively charged particles in glass-based devices with and without surface modification, respectively. However, the time-consuming fabrication and surface-modification procedure and the requirement of high-end nanofabrication facilities restrict the widespread development and use of the technology and device. To simplify the development of devices for both positively and negatively charged particles trapping, we developed fluidic devices based on poly-dimethylsiloxane using soft-lithography techniques and a new surface modification procedure. To compare the performance of PDMS-based GIE-trapping devices before and after the surface modification, two polyelectrolyte layers were used to modify the surface charge density of the device surface first from negative to positive and then from positive to negative – leading to an overall net negative surface charge density after the surface modification process. Au NPs were used to examine the trapping efficiency of the devices with and without surface modification, demonstrating the successful trapping with comparable efficiency. Experimental results were compared with simulated results, and a good agreement was found.

Since the efficiency of GIE-trapping depends on the geometrical parameters, it is essential to understand the influence of different critical geometrical parameters and the salt concentration of the solution used to perform particle trapping. To do so, extensive numerical simulations were performed, and observed particle trapping trends for each critical parameter are presented in this thesis. For numerical simulations, two approaches are presented: 1) charged particle inclusive simulations and 2) point charge approximation. Charged particle inclusive simulations are time-consuming, but provide more realistic trapping efficiency. In contrast, the point charge approximation approach is time efficient since it uses a point charge at the place of a charged particle in the simulation to speed up the simulation process and achieve approximate values for trapping parameters, such as depth of the potential trap, particle residence time, trapping strength, and electrostatic potential distribution inside the GIE-trapping device. These numerical calculations are very beneficial for optimizing the GIE-trapping device geometry based on the target trapping efficiency for specific charged particles, which reduces the experimental and device fabrication efforts for the fluidic device and helps optimize of experimental conditions.

Although GIE-trapping devices are very useful for high-throughput single particle trapping, they are nearly impractical to be used in aqueous solutions of high salt concentrations such as seawater, blood, and other body fluids since in these solutions, salt ions suppress the electrostatic effect of the charged surface required for the trapping. Therefore, to conduct molecular sensing in physiological conditions, a new device was developed using geometrical trapping for size-selective particle sorting and trapping. For nanoparticle sorting and separation from macro-sized molecules in the solution, deterministic lateral displacement (DLD) arrays were incorporated, which worked both for the sieving of the nanoparticles and their directional motion inside the device. The device performance was analyzed using Au NPs of different sizes ranging from 60 nm to 250 nm in diameter, and a directional motion of

nanoparticles and a successful size-based particle trapping were achieved. The method and device can potentially be used for early diagnosis of various diseases that can be identified based on antigen-antibody complex formation.

Thesis outline and overview

This doctoral work focuses on: 1) the optimization of GIE-trapping devices for high-throughput particle trapping and analysis and extending their applicability for both academic and industrial research and 2) the development of integrated micro- and nanofluidic devices for size-selective particle sorting and trapping for molecular sensing using optical methods such as iSCAT, Raman spectroscopy, and fluorescence microscopy. All conducted research and studies are presented in Chapters 2 to 6, with a final summary and outlook in Chapter 7. The overview of each chapter is as follows:

Chapter 2 provides an overview of all the techniques, methods, and theories used throughout the research work for both electrostatic trapping and geometrical trapping. The principle of geometrically-induced electrostatic trapping, the concept of direction particle motion using DLD arrays, interferometric scattering (iSCAT) detection technique for particle tracking and its advantages, Raman spectroscopy and its advantage in molecular sensing are the main topics that are addressed in this chapter.

Chapter 3 explains why glass-based devices can only enable the electrostatic trapping of negatively charged nano-objects and what should be done to use these devices for positively charged nanoparticles. It, furthermore, focuses on the fabrication of integrated micro- and nanofluidic devices using glass substrates and their surface modification using polyelectrolytes. A comparison study between the trapping of negatively charged Au NPs in a glass-based GIE-trapping device and positively charged Au NPs in a surface modified device is presented to analyze the performance of GIE-trapping devices before and after surface modification. The device performance was examined by detecting and tracking trapped nanoparticles using the iSCAT method. It is further explained how the detected motion of a particle inside the electrostatic trap is used to calculate the trapping stiffness constant to quantify the strength of the potential trap. The procedure for preparing Au NPs samples used for the above experiments is also described in detail.

Chapter 4 takes the surface modification of GIE-trapping devices a step further and presents how multi-polyelectrolyte layers can be used to achieve homogeneous surface charge density inside the fluidic device. To make the surface modification procedure less complex and time effective, we introduced PDMS-based GIE-trapping devices and utilized them for surface modification. Using PDMS-based fluidic devices not only reduces the fabrication time but also reduces surface modification time by almost a factor of ten. In this work, two layers of polyelectrolytes were used to achieve an overall negative surface charge density so that the trapping efficiency of the modified devices can be compared with the non-modified PDMS devices. The chapter presents the successfully achieved comparable device performance. Furthermore, it demonstrates how multiple particles can be trapped in larger nanopockets

and how these multi-occupancies can be identified with the help of iSCAT data. The experimental data are successfully compared with the numerical results.

Chapter 5 presents the simulation of GIE trapping to examine how different geometrical parameters and salt concentrations of the used solutions during experiments affect the final trapping efficiency. The impacts of these crucial parameters on particle trapping were studied using two different approaches to perform numerical simulations. In the first approach, the trapped charged particle was replaced by a point charge with the same charge as the net surface charge of the particle used in the experiments. This helps to speed up the simulations and collect approximate values of the stiffness constant for the GIE trapping. The stiffness constant represents the confinement force experienced by the particle in the trap. The point charge approximation was also used to observe the trend of the stiffness constant of the trapped particle with respect to all critical parameters. In the second approach, a charged particle was used in the simulations with the assumption that all charges of the particle were residing on the surface of the particle. This approach is more realistic and gives a more accurate stiffness constant; however, the approach is time consuming. Results from both simulation approaches are presented and compared with experimental data, and a theoretical explanation is given on how these simulations are performed and how the potential well's depth and width affect the trapped particles' residence time and stiffness constant.

Chapter 6 introduces a new method of particle trapping, which is based on size-selective particle sorting and trapping. The method targets applications where physiological conditions are required to examine the presence of specific molecules in the solution. These applications require a high signal-to-noise ratio and the possibility of separating unwanted biomolecules from the final sample collection for measurement. All these requirements cannot be fulfilled in GIE-trapping devices as the electrostatic behavior of the device surface is screened due to the high ionic nature of body fluids. The chapter includes the fabrication procedure used for the development of the fluidic device with the new trapping method. The performance of the device was demonstrated experimentally using Au NPs of different sizes in a high salt concentration solution. For particle tracking and detection, the iSCAT technique was used in combination with Raman spectroscopy, where Raman spectroscopy was used to collect molecular-specific signals from the trapped nanoparticles.

Chapter 7 summarizes the work presented in the previous chapters and presents an outlook to address potential applications and future research work to further develop the fluidic devices in the direction of a highly efficient and multiplexed lab-on-a-chip device that can be used for multiple applications from molecular sensing to biological studies under physiologically relevant conditions.

Chapter 2. Nanoparticle trapping, tracking and detection in fluidic devices

2.1 Geometry-induced electrostatic trapping inside a fluidic device

Substrates like silicon dioxide, glass, and PDMS that contain silanol (Si—OH) groups on the surface attain a net negative surface charge density in contact with an aqueous solution (pH > 2).^{118,119} The introduction of a negative surface charge density is due to the deprotonation of the terminal silanol group inside the aqueous environment. The charged surface causes the redistribution of ions in the solution, forming an electric double layer (EDL), which consists of two parallel layers of ions from the solution. The EDL can be modelled using the Stern or Gouy-Chapmann (GC) representation. In the Stern representation, ions are considered to have a finite size; therefore, the double layer is divided into two parts 1) Stern Layer and 2) Diffuse Layer. The Stern layer comprises ions that are charged oppositely to the charged substrate surface and stay immobile (see Figure 2.1). The diffuse layer comprises the free ions in the solution attached to the surface via Coulomb interaction; therefore not firmly attached to the surface. Consequently, ions in the diffuse layer can move in the fluid under the influence of thermal motion. In the GC representation, charged particles are considered as point charges; therefore, only the diffuse layer is considered for EDL (see Figure 2.2). In the Stern layer, the electrostatic potential decays linearly, whereas in the diffuse layer, the electrostatic potential decays exponentially.

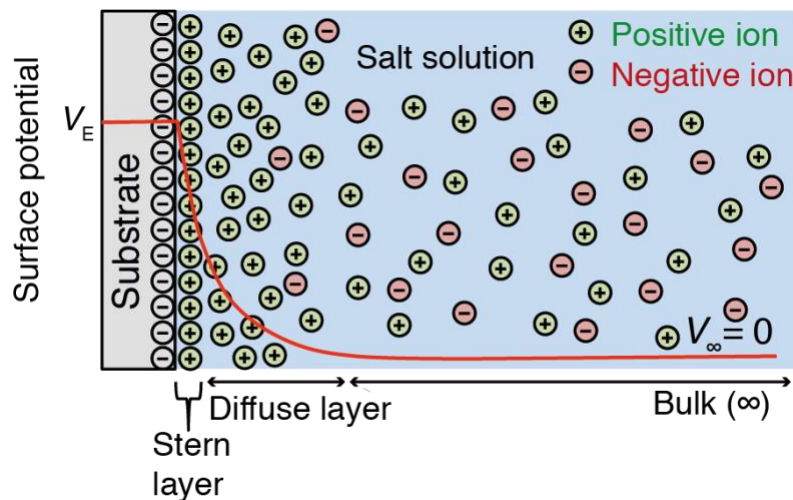


Figure 2.1 Stern representation of an electric double layer formation due to a charged substrate inside an aqueous solution. The electrostatic potential decays linearly in the Stern layer and exponentially in the diffuse layer.

The GC representation gives a simplified approximation of the EDL in a solution with reasonable accuracy. Therefore, for the simplicity of numerical calculations, the GC representation is used in this study, where only the exponential decay of potential is

considered, as shown in Figure 2.2(a). The electrostatic potential of an EDL is in the range of a few tens to a few hundreds of nanometers. The electrostatic potential distribution in the diffuse layer can be expressed by the Poisson-Boltzmann (PB) equation that can be further used for numerical calculations¹¹² as described in Chapter 5.

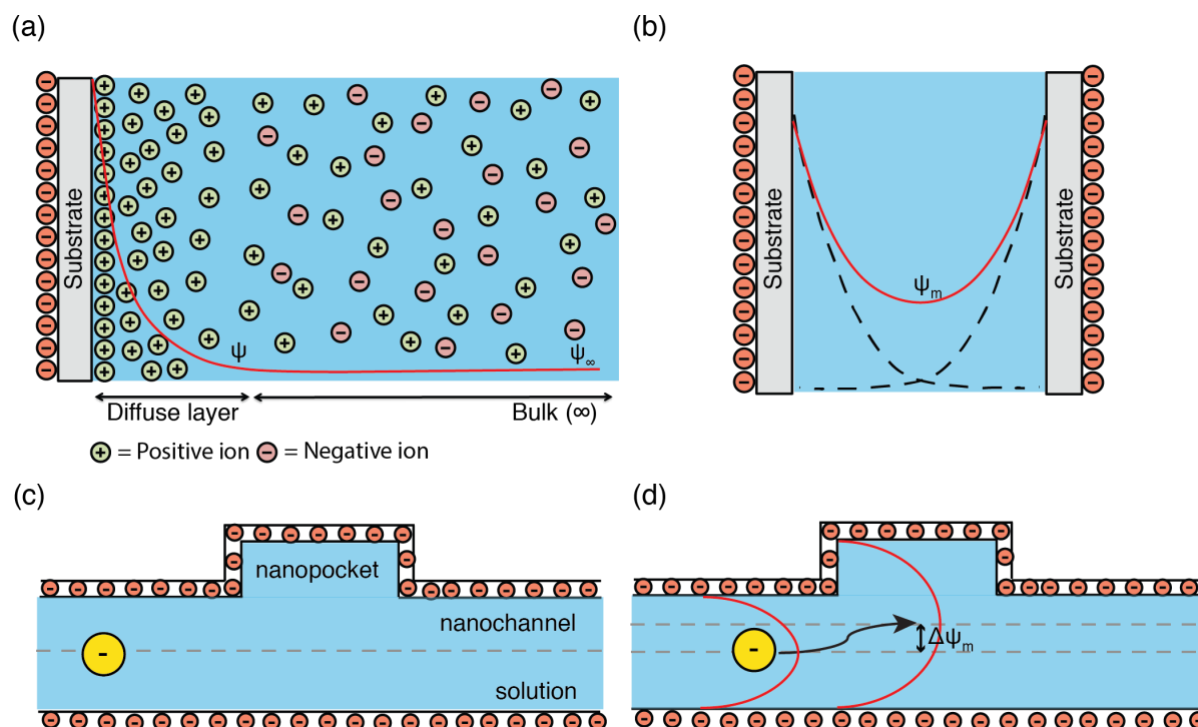


Figure 2.2 Demonstration of geometry-induced electrostatic trapping of a charged nanoparticle: (a) electrostatic potential distribution from a negatively charged surface in an aqueous solution due to redistribution of ions inside the solution, (b) formation of a potential well between two charged surfaces due to the overlap of electrostatic potential distribution from both the charged surfaces, (c) schematic of a geometry-induced electrostatic trapping device for contact-free trapping of negatively charged gold nanoparticle, (d) demonstration of the potential minima shifting from the midplane of the nanochannel at the location of the nanopocket, because of that the charged particle moves towards the nanopocket from the nanochannel midplane.

When two charged surfaces are brought together, as shown in Figure 2.2(b), it forms a potential well between them due to the overlap of electrostatic potentials from both surfaces. To use this phenomenon for electrostatic trapping of charged nanoparticles, a fluidic device requires nanochannels embedded with nanoindentations such as nanopockets. The potential distribution inside the nanochannel keeps a negatively charged nanoparticle at the midplane of the channel and allows a contact-free diffusion of a charged particle along the nanochannel. When such a particle comes in contact with a nanoindentation embedded in the nanochannel, the particle moves towards the nanoindentation, also known as the nanotrap, to attain the least possible potential energy. The formation of a harmonic potential inside the nanopockets is presented in detail in Chapter 3. If the potential well created inside a nanotrap has a potential depth ($\Delta\psi_m$) of more than $10 k_B T$ ^{120,121} that can compensate the thermal fluctuations of the particle, a particle in thermal equilibrium condition gets trapped

inside the electrostatic nanotrap in a contact-free manner. The nanotrap has a harmonic potential well inside it due to the overlap of electrostatic potential from the charged surfaces of the nanotrap. This potential well shifts the position of the minimum potential energy from the midplane of the nanochannel to an inner position of the nanotrap. The amount of this shift depends on the geometry of the nanopocket and the salt concentration of the solution used for the particle trapping experiment. The influence of geometrical parameters of a nanotrap on the final shift in the position of the minimum potential energy and final particle trapping efficiency are discussed in detail in Chapter 5.

2.2 Particle tracking using interferometric scattering detection technique

To examine the particles and molecules in their native state in a label-free manner, iSCAT method comes as a very effective method for particle detection. In comparison to other widely known methods for single molecular studies and detection, such as fluorescence, which requires molecular labeling and is strongly affected by photobleaching, thus limiting the photoemission from molecules under detection, iSCAT solely depends on the interference of light scattered by the particle and light reflected from the device surfaces. Therefore, unlike fluorescence microscopy, the iSCAT technique does not get limited in the observation time and signal due to photobleaching in which fluorophores lose their ability to fluoresce. Additionally, the iSCAT method works for the whole object under the focus and gives complete information about the object's movement and fluctuation. However, the same is not possible in fluorescence microscopy, wherein each molecular component needs to be labeled with specific fluorophores for detection. Therefore, iSCAT comes as a breakthrough in the field of label-free single molecule detection. In the past two decades, the technology has been used for the detection of single dye molecules, viruses, semiconductor quantum dots, molecular motors, vesicles, lipids, DNA, bacteria, etc.¹²²

2.3 iSCAT Principle

In an iSCAT microscopy, label-free detection is done based on the interference of light scattered from the particle under inspection and the reference light collected from the reflections of the incident light beam from the interfaces, as shown in Figure 2.3. The setup alignment is done to obtain a sharp interference image is obtained at the detector. The iSCAT setup can be built in multiple configurations as presented in recent works¹²²⁻¹²⁴.

The working principle of iSCAT detection is shown in Figure 2.3, where a trapped gold nanoparticle is under observation for its motion under the influence of an electrostatic trap inside a GIE-trapping device. As shown in Figure 2.3, the incident field (E_i) is partially reflected at the cover glass-solution interface ($E_{r1} = R_1 E_i$) and the solution-substrate interface ($E_{r2} = R_2 E_i$) and scattered by the object in focus ($E_s = S E_i$). Here, the reflectivity for the interface of cover glass and water solution is $R_1 = 0.42\%$ and for the interface of water solution and PDMS substrate (refractive index ~ 1.4) is $R_2 = 0.06\%$. As the reflectivity for the glass-water interface is higher than the PDMS-water interface, the mean contrast and signal-to-noise ratio (SNR) is relatively better for glass-based GIE-trapping devices^{113,125}. The scattering coefficient (S)

depends on the polarizability (α) of the particle¹²⁶ that is linked to the diameter of the particle (D_p), the dielectric constant of the particle (ϵ_p), and the dielectric constant of the medium (ϵ_m) as:

$$S(\lambda) = \eta\alpha(\lambda) = C_s \epsilon_m(\lambda) \frac{\pi D_p^3}{2} \frac{\epsilon_p(\lambda) - \epsilon_m(\lambda)}{\epsilon_p(\lambda) + 2 \epsilon_m(\lambda)} \quad (2.1)$$

where, C_s is the proportionality constant and λ is the wavelength of the laser light used for the detection.

Since the objective lens focuses on the particle inside the nanopocket, the reflected field E_{r2} would serve as the main reference field (E_r) at the detector, where the total field is given as: $E_d = E_r + E_s$. The corresponding intensity (I_d) collected at the camera is:

$$I_d = |E_r + E_s|^2 = |E_i|^2 \{R^2 + S^2 - 2R|S| \sin \theta\} \quad (2.2)$$

where, θ is the phase of the scattered field $S = |S|e^{i\theta}$.

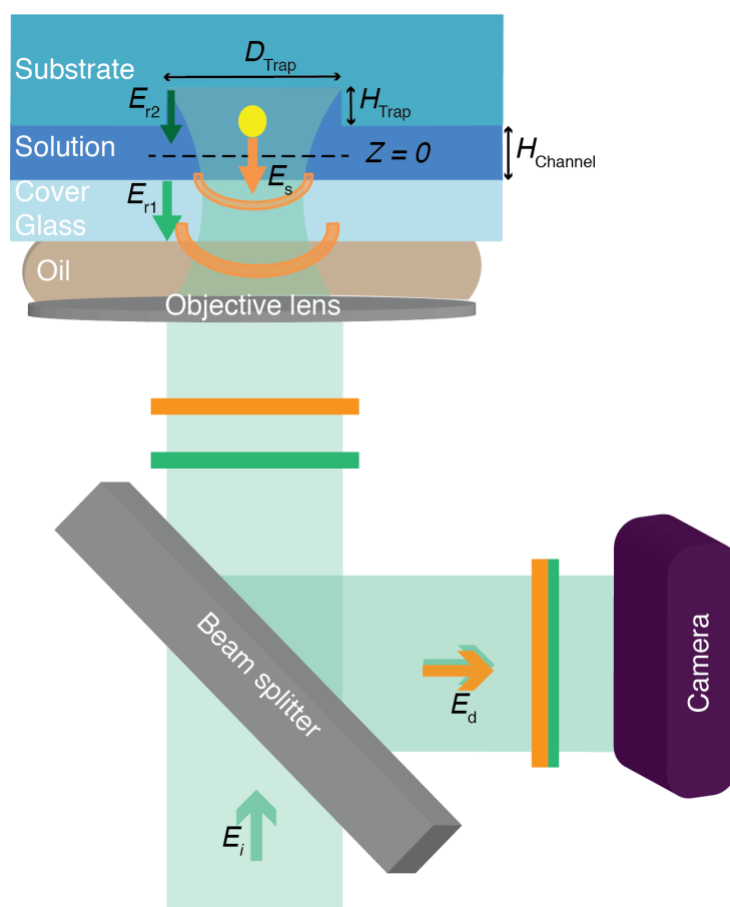


Figure 2.3 Working principle of interferometric scattering microscopy for detecting a nanoparticle inside a fluidic device. The camera detects the signal from the interference of light scattered by the object and light reflected at the interface between the aqueous solution and the device surface. The schematic diagram represents a gold nanoparticle trapped in a nanopocket inside a nanofluidic device containing a nanochannel of height H_{Channel} with an embedded nanotrap of diameter D and height H_{Trap} .

In equation 2.2, R^2 represents the background signal, and S^2 denotes the scattering signal that scales with the particle diameter as D_p^6 . The interference term $2R|S|\sin\theta$ scales with D_p^3 . With the reduction in the size of the nanoparticle, the interference term starts dominating the pure scattering term, allowing the detection of molecules and nanoparticles down a few nanometers.^{123,124}

2.4 iSCAT Setup

To track the motion of nanoparticles inside the nanofluidics devices with a high spatiotemporal resolution, a home-built iSCAT setup was used, as shown in Figure 2.4. The setup used a 300 mW, 532 nm emission wavelength solid-state laser (MGL-III-532, CNILaser) to generate the incident light beam. The laser beam was used to create an illumination area of $25\ \mu\text{m} \times 25\ \mu\text{m}$ on the sample surface by deflecting it in the x and y directions using a two-axis deflector system (GVS002, Thorlabs Inc.) running at the maximum frequency of 1 kHz frequency. To control the intensity of the incident beam on the sample surface, a neutral density (ND) filter with adjustable optical density (OD) was incorporated in the optical path. The incident beam was directed towards a Leica Microscope that consists of a telescopic lens system, a beam splitter, and a 100x / 1.3 numerical aperture (NA) oil objective lens. In order to collect the signal from the sample, a CMOS camera (Photon Focus, MV-D1024-160-CL-12) is connected at one of the camera ports of the microscope. The deflector system and camera were synchronized to a four-channel analog output (AO)-LabView controller (cDAQ-9171/NI 9269, LabView) to synchronize image acquisition and mirror deflection. A LabView platform is custom-developed to control image acquisition rate, illumination area, and exposure time during the experiment.

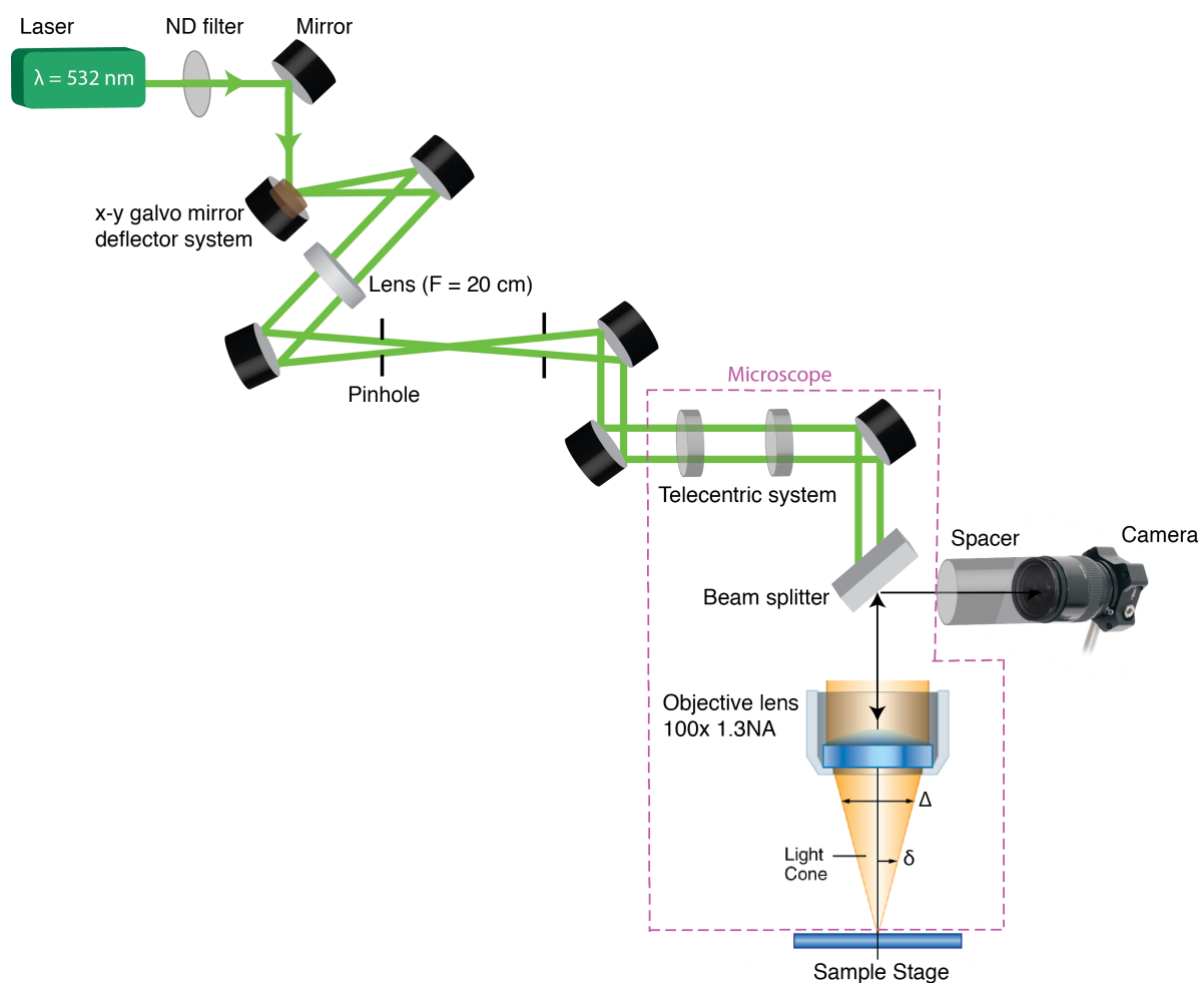


Figure 2.4 Schematics of the in-house built iSCAT setup. The setup is designed for a 532 nm laser light and consists of an optical path to bring the incident light beam inside a microscope that includes a telecentric lens system to focus the incident light beam, a beam splitter, a 100x / 1.3 NA oil objective lens, and a sample stage. One microscope exit is connected with a spacer and a camera to capture the reflected beam from the sample surface and the scattered beam from the object under focus. To increase the detection area on the sample surface, an xy mirror deflector system is incorporated in the initial optical path.

2.5 iSCAT data processing

In the thesis, iSCAT detection was used for the tracking of nanoparticles in the nanofluidic device. In the case of GIE trapping, the particle motion inside the electrostatic potential trap was recorded using iSCAT, and collected images were processed to obtain the particle positions and trajectories and to analyze the strength of the electrostatic potential trap, trapping time, and the depth of the potential trap. For single nanoparticle trapping analysis, iSCAT images were collected at 111 Hz frequency with a 1 ms exposure time. Each recorded image was processed to collect the intensity profile of the trapped particle and use that information to obtain the particle center (x, y) by Gaussian fitting of the particle intensity profile.^{111,113} The particle center location from each recorded frame was used to determine

the particle displacement from one frame to the other and eventually to record the particle motion over time t .

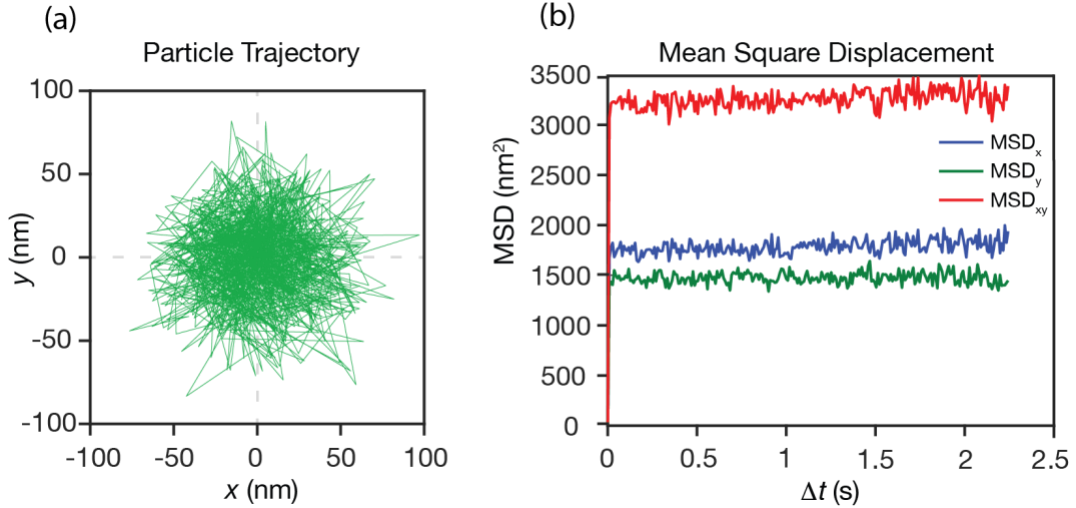


Figure 2.5 (a) Trajectory of a particle trapped inside an electrostatic potential trap in a nanofluidic device. The particle trajectory was obtained from the analysis of images collected using the iSCAT technique. (b) The measured trajectory was further used to calculate mean square displacement of the particle as a function of time.

As shown in Figure 2.5, recorded particle trajectory was used further to calculate mean square displacement (MSD) of the particle in x , y and the radial direction ($r = \sqrt{x^2 + y^2}$). The MSD describes the diffusion motion of an object in an aqueous solution and is linked with the diffusion coefficient of the object and lag time Δt . MSD in x , y , and the radial directions are¹²⁷:

$$\text{MSD}_x = \langle [\Delta x (\Delta t)]^2 \rangle \quad (2.3)$$

$$\text{MSD}_y = \langle [\Delta y (\Delta t)]^2 \rangle \quad (2.4)$$

$$\text{MSD}_r = \text{MSD}_x + \text{MSD}_y \quad (2.5)$$

$$\text{MSD}_r = \langle [\Delta r (\Delta t)]^2 \rangle = \langle [\Delta x (\Delta t)]^2 \rangle + \langle [\Delta y (\Delta t)]^2 \rangle = 4D\Delta t \quad (2.6)$$

where D is the two-dimensional diffusion coefficient. The one-dimensional diffusion coefficient for the x and y directions can be calculated by finding the slope value of the respective MSD- Δt curve at $\Delta t = 0$. Additionally, the diffusion coefficient of the spherical particle in an aqueous solution can be calculated by the Stokes-Einstein equation^{110,125,128}:

$$D = \frac{k_B T}{3\pi\eta D_p} \quad (2.7)$$

where, η is the dynamic viscosity of the liquid, and D_p is the particle diameter.

In the case of particle confinement inside a potential trap, the maximum particle diffusion from the center of the trap is limited by the trap boundaries; therefore, the mean square displacement of a trapped particle reached a plateau for larger lag times, as shown in Figure 2.5. This restricted Brownian diffusion of the particle in the cylindrical nanotrap is equivalent to the particle diffusion inside an infinitely high cylindrical potential. The radial MSD value at the plateau $[MSD_r]_{plateau}$ is $\langle[\Delta r]_p^2\rangle$. The $[MSD_r]_{plateau}$ value is correlated with the radial stiffness constant (k_r) by:

$$\langle[\Delta r]_p^2\rangle = 4k_B T/k_r, \quad (2.8)$$

where k_B is the Boltzmann constant and T is the absolute room temperature¹¹⁰.

In addition to the radial stiffness constant of the electrostatic potential trap, other parameters are also important to analyze the performance of a GIE-trapping device. These parameters are: (a) depth (Q) of the potential well and (b) mean residence time of the particle ($\bar{\tau}_k$) inside the trap also known as Kramers time^{110,125,129}. To obtain the Kramers time of a nano-object, particle tracking data is used to identify the residence times of many particles inside the electrostatic traps. This data provides a residence time probability distribution $P(\tau)$ as a function of residence time τ , which is used to determine the Kramers time of the particle:

$$P(\tau) = C e^{\frac{-\tau}{\bar{\tau}_k}} \quad (2.9)$$

The Kramers time of the particle is used then to determine the trap depth (Q) of the potential trap by:

$$\bar{\tau}_k \cong \tau_R e^{Q/k_B T}, \quad (2.10)$$

where, τ_R is the relaxation time of the particle in the potential well denoting the time required by a particle to freely diffuse through a distance equivalent to the width of the trap. The relaxation time of a particle is calculated using the diffusion coefficient of the particle and radial trapping stiffness constant by¹²⁵:

$$\tau_R = \frac{k_B T}{D k_r} \quad (2.11)$$

These three parameters allow to effectively analyze the performance of an electrostatic potential well and hence the trapping efficiency of a geometry-induced electrostatic trapping fluidic device.

2.6 Numerical simulations for GIE-trapping devices

Optimization of a GIE-trapping device for a stiffer particle trapping based on experimental results is a very expensive and demanding process. Thus, it is important to optimize geometrical parameters of a fluidic device using numerical simulations, based on the final application, charge and size of the particle, and salt concentration of the solution to be used for particle trapping. To optimize the device design, the potential distribution inside the fluidic device in the absence and presence of particle needs to be calculated, and later on, used to identify the impact of the potential trap on the electrostatic self-energy of the charged particle and the Helmholtz free energy of the system during trapping. The Helmholtz free energy distribution with respect to the particle position inside and outside the potential trap gives information about the particle residence time and particle trapping strength of the device. To perform such complex and demanding numerical calculations and iterations, the finite element method (FEM) is one of the most efficient tools that can be used. FEM is a numerical computation method for solving partial differential equations (PDEs) and integral equations. Since in GIE-trapping devices the electrostatic potential is dominated and exploited for particle trapping, partial differential equations for potential distribution inside the device need to be computed. Thereafter, integrals must be solved numerically to calculate the system's free energy and entropy. Therefore, to simplify the computational process COMSOL Multiphysics simulation software is used, which is based on the finite element method (FEM).

2.7 Finite element method and COMSOL

The FEM is based on Galerkin weighted residual technique¹³⁰ or variational approach¹³¹ to solve boundary value problems. In the variational method, a PDE is formulated as a function that has an energy interpretation, and to achieve the minimum potential value, the function is minimized. The Galerkin method is a special case of the method of weighted residuals (MWR), in which minimization of a weighted error is performed on the domain, making it a universally applicable method^{132,133}. In FEM, the computational domain is divided into small elements using the mesh generation techniques. Generally, these elements are triangular shaped in the case of the two-dimensional (2D) domain and tetrahedral shaped for the three-dimensional (3D) simulation domain. Since tetrahedral shapes can fill any 3D volume, it is a commonly used element shape for finite element analysis (FEA) in 3D space. In this work, tetrahedral elements were used for 3D simulations to approximate the potential distribution inside the fluidic device geometry. To solve a PDE using FEM, appropriate and sufficient boundary conditions (BCs) must be placed to allow the transformation of a PDE into an algebraic equation that can be solved over the computational domain to get the final value of the function. To perform the 3D simulations, commercial simulation platform COMSOL Multiphysics 4.2 was used, which has built-in solvers based on the physics used for the numerical calculations. The platform allows for easy structure design and automated rendering and grid formation with the possibility of fine-tuning the grid to achieve better convergence of the numerical calculations.

To simulate GIE trapping in COMSOL Multiphysics 4.2, a 3D model of a nanochannel with one nanopocket and a charged particle was used. In the case of point charge approximation

simulations, the charged particle was replaced by a single point charge; therefore was not considered in the simulations for the potential distribution calculations. To reduce the computational burden, the 3D model was cut in half owing to the symmetry of the potential distribution. For potential distribution inside the GIE-trapping device, a Poisson-Boltzmann (PB) equation was solved using the electrostatic interface of COMSOL. To ensure the convergence of the simulation for an accurate computation result, the element size limit was kept between 0.6 nm – 10 nm. During numerical calculations using FEM, element size and distribution along the computational domain plays an important role in the convergence of the simulation. The computed potential distribution inside the fluidic device was used further to calculate system free energy and entropy to identify the trapping strength of the electrostatic trapping, as described in detail in Chapter 6.

2.8 Principle of DLD arrays for directional particle motion

Deterministic lateral displacement (DLD) is a commonly used technique for size-based particle separation and directional motion of particles using post arrays symmetric to the flow in a channel.^{79,134-136} The post arrays are placed at an angle (θ) with respect to the flow direction, which allows the angular displacement of the particles larger than the critical diameter ($D_{critical}$). The particles smaller than the $D_{critical}$ move along the flow in the channel. The value of the critical diameter depends on the geometrical characteristics of the DLD arrays, such as the shape of the pillars, pillar interspacing, orientation of the pillars, angular and spatial shift between array rows.¹³⁷⁻¹³⁹

Among DLD arrays a spherical particle can have two different modes of motion: 1) lateral displacement (LD) also known as bumping mode and 2) zigzag (ZZ) trajectory.^{79,134,135,139} A LD mode is considered when a particle motion is along a train of DLD pillars with a constant angle close to the gradient angle ($\theta = \tan^{-1} \lambda/\Delta\lambda$) of the DLD pillars, whereas a ZZ trajectory is considered when a particle shifts from one DLD pillar channel to another with its angle close to zero. Particles smaller than $D_{critical}$ show ZZ trajectory and particles bigger than $D_{critical}$ move in the LD trajectory.

As shown in Figure 2.6, the gap between two array posts is G , and distance between the centers of two pillars is λ . The lateral and angular shift in the consecutive rows is $\Delta\lambda$ and θ , respectively. Therefore, the row shift fraction $\epsilon_{row} = \Delta\lambda/\lambda$, which, furthermore, gives the number of flow streams that pass through the gap of DLD posts $n_{flow\ stream} = 1/\epsilon_{row} = \lambda/\Delta\lambda$. Each flow stream passing through the gap carriers equals fluid flux.¹³⁹

In the case of circular DLD pillars, $D_{critical}$ for spherical particles can be calculated using the pillar gap and the period of DLD arrays ($N = \lambda/\Delta\lambda$)¹³⁷:

$$D_{critical} = 1.4GN^{-0.48} \quad (2.12)$$

In addition to circular DLD pillars, other pillar designs have also been used to improve the particle separation efficiency^{137,140,141}. However, for the determination of $D_{critical}$ in the case of non-spherical pillars a shape factor α_{DLD} is introduced:

$$\alpha_{DLD} = \frac{1}{N} k(\eta) + b(\eta) \quad (2.13)$$

where $\eta = b/a$, and k and b are functions of η ¹³⁷.

For micro particle separation using DLD pillars, the influence of electrostatic forces from device walls and particles is negligible. However, in the case of nanoparticle DLD separation, electrostatic effects become important for accurate separation efficiency and particle critical diameter calculation. Due to the electrostatic interactions between particle and pillars, the effective diameter of the particle becomes $D_{apparent} = D_{particle} + d_{EF}$, where d_{EF} is the displacement caused by the electrostatic force between the particle and the pillar¹³⁴.

Therefore, in the case of deterministic displacement of nanoparticles it is important that $D_{apparent} > D_{critical}$.

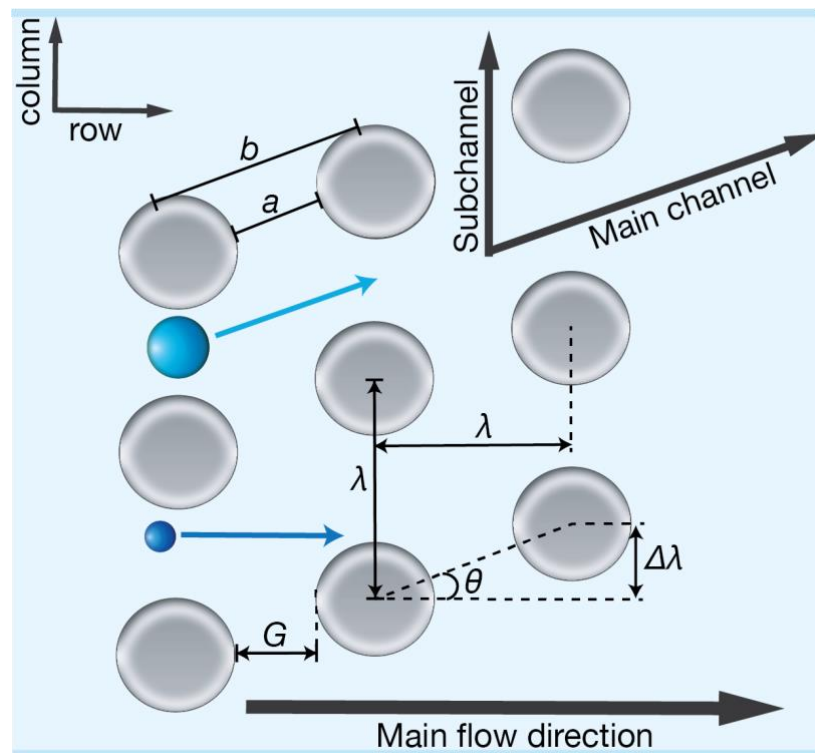


Figure 2.6 Deterministic lateral displacement post array with gradient angle θ and spatial shift between consecutive rows $\Delta\lambda$. The gap between two posts is G and the distance between the center of two posts both along the row and channel is λ . The larger particle ($D_{particle} > D_{critical}$) moves along the main channel and follows

lateral displacement mode, whereas the smaller particle ($D_{\text{particle}} < D_{\text{critical}}$) takes a zigzag trajectory and follows the laminar flow in the direction of the main fluid flow. The width of the subchannel is denoted by a and b .

2.9 Principle of Raman spectroscopy and its usage for molecular detection

2.9.1 Raman Spectroscopy

Raman spectroscopy exploits the interactions of radiation with molecular vibrations and rotations. It relies on Raman scattering inelastic light scattering of photons from the molecule under observation. The Raman signal from a molecule is used to determine the vibrational modes of the molecule, which serves as a molecular fingerprint. Additionally, Raman spectra provide molecular structure, dynamic, and environment information^{142,143}. There are multiple variants of Raman spectroscopy such as surface-enhanced Raman¹⁴⁴, tip-enhanced Raman¹⁴⁵, stimulated Raman¹⁴⁶, hyper Raman¹⁴⁷, and resonance Raman spectroscopy¹⁴⁸.

When a molecule is excited with laser light, the photon excites the sample and puts the molecule into a virtual energy state. The lifetime of the molecule in the virtual energy state is very short. Due to the instability of the molecule at the virtual energy state, it returns to the stable energy state and therefore scatters photons corresponding to the final energy state. When the energy of scattered and incident photons is the same, it is known as Rayleigh or elastic scattering, whereas when the energy of the scattered photon is higher or lower than the incident photon, the scattering is called inelastic scattering, also known as Raman scattering. The schematic of the scattering process is shown in Figure 2.7. After the inelastic scattering, the molecule reaches a different rotational or vibrational state with respect to the initial state. For Raman scattering, the shift in photon energy is independent of the incident photon energy. This phenomenon can be explained in terms of the interaction of the laser light with the molecular vibrations and other excitations in the molecular system, resulting in the shift of the energy of the scattered photon.

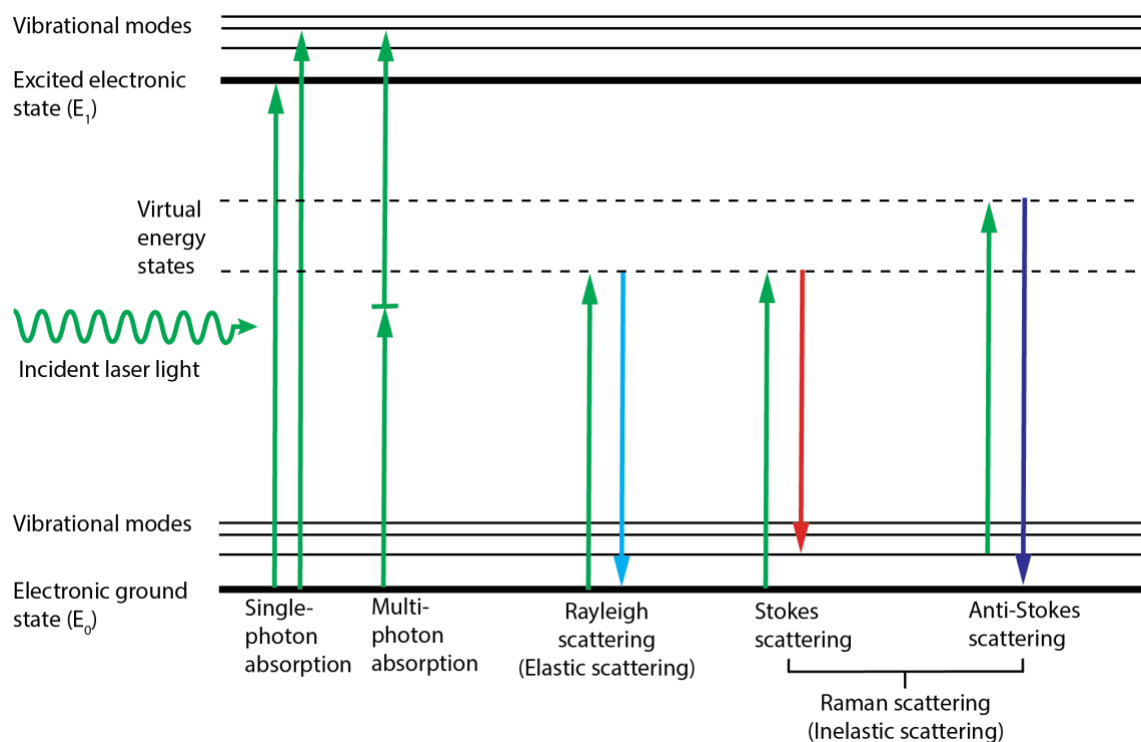


Figure 2.7 Energy-level diagram of photon absorption and scattering phenomena when a molecular system is exposed to the continuous wave laser light. In the case of absorption, laser photons excite the system to a higher electronic state or vibrational mode using single or multi-photon absorption. In the case of scattering, incident photons excite the system to a virtual energy state that leads to elastic or inelastic scattering based on the energy states involved in excitation and the scattering phenomenon. When the scattered photon has a higher or lower energy compared to the incident photon, it is known as Raman scattering, whereas when the scattered photon has the same energy as the incident photon, it is known as Rayleigh scattering.

The Raman scattering provides characteristic fundamental vibration signals of molecules, associated with the molecular structure and can be employed to identify the molecule. While other vibrational spectroscopies¹⁴⁹ can also be used for elucidating the molecular structure of the sample, Raman spectroscopy is best to detect symmetric vibrations of nonpolar groups. However, despite its enormous advantage in molecular detection, the Raman scattering technique was not recognized as a practical biosensing tool^{150,151} until the discovery of surface-enhanced-Raman scattering (SERS)^{152,153} due to the low probability of Raman scattering (1 in 10^7 photons)^{154,155}.

2.9.2 Surface-enhanced Raman Spectroscopy

In Raman scattering, when a molecule is impinged with laser light, it excites molecular vibrations leading to the formation of a dipole due to the charge motion in the vibration.^{156,157} The dipole created is proportional to the polarizability of the molecule and the amplitude of the incident electric field. Therefore, the Raman signal can be increased by increasing either the molecular polarizability or the amplitude of the incident electric field¹⁵⁸.

Surface-enhanced Raman scattering is a surface sensitive phenomenon that enhances the Raman scattering signal of a molecule adsorbed on or in the vicinity of nanostructured or rough metallic surfaces with roughness at a nanometer scale (10 – 100 nm)¹⁵⁸. To achieve the SERS signal of a molecule, metallic nanoparticles or a patterned array of nanoparticles can also be used in place of nanostructured surfaces. There are two independent enhancement mechanisms leading to the SERS phenomenon, 1) chemical enhancement^{148,159} and 2) electromagnetic enhancement, which are linked with the molecular polarizability and electric field amplitude enhancement, respectively¹⁵⁶. However, it is difficult to separate these effects when the SERS signal is collected using a system that supports electromagnetic enhancement.

In the chemical theory for SERS enhancement, the electronic state of the molecule gets modified due to either the charge transfer between a metallic surface and the molecule or the formation of a metal-molecule complex.¹⁶⁰ However, the impact of chemical effects is negligible compared to the electromagnetic effect.¹⁵⁶⁻¹⁵⁸ As per the electromagnetic theory of SERS enhancement, the rough metallic surface enhances the electric field leading to an increase of the Raman scattering signal for the adsorbed molecule. The electric field enhancement on the roughened surface or metallic nanostructure is directly related to the optical properties of the SERS substrate. Several processes can be involved in the final electromagnetic enhancement of Raman scattering, such as the excitation of localized surface plasmons (LSP) which is the collective oscillation of the electron cloud within the nanostructure¹⁵⁷, electromagnetic coupling between nanostructures with a gap less than 10 nm¹⁶¹, and accumulation of charges at the tip of nanostructure leading to the lightning rod effect¹⁶². To achieve the SERS effect, nanoparticles are also employed in molecular detection studies as they provide a surface that can allow collective localized plasmonic oscillations and field enhancement between the nanoparticles in the case of a nanoscale gap. To optimize the SERS signal, different shapes, such as nanospheres, nanostars, and nanotriangles, and sizes of nanoparticles have been in use for molecular detection¹⁶³. It has been noted that SERS on metal nanoparticles is hugely dominated by the enhancement from hot spots, which are fissures and interstices in or between nanostructures or nanoparticle and underlying metal surface.¹⁶⁴⁻¹⁶⁶ There have been various studies where nanoparticles were used for molecular detection using the SERS spectrum^{167,168} and also enabled multiplex SERS bioimaging¹⁶⁹⁻¹⁷¹. The SERS method also used for biomedical studies¹⁵¹, pathogen detection¹⁷², and disease diagnostics using various SERS active substrates, including nanoparticles and patterned nanostructures.^{173,174}

Chapter 3. Single Positively Charged Particle Trapping in Nanofluidic Systems

Deepika Sharma ^{a,b,c,*}, Michael A. Gerspach ^{a,b,d}, Thomas Pfohl ^{a,e}, Roderick Y.H. Lim ^{a,c}, Yasin Ekinci ^{a,b,*}

^a Swiss Nanoscience Institute, 4056 Basel, Switzerland

^b Laboratory for Micro and Nanotechnology, Paul Scherrer Institute, 5232 Villigen, Switzerland

^c Biozentrum, University of Basel, 4056 Basel, Switzerland

^d Chemistry Department, University of Basel, 4056 Basel, Switzerland

^e Biomaterials Science Center, University of Basel, 4123 Allschwil, Switzerland

*corresponding author: deepika.sharma@psi.ch

ABSTRACT

High-throughput and contact-free trapping of single nano-objects in an aqueous solution is of substantial interest for fundamental and applied research. One of the several trapping methods is geometry-induced electrostatic (GIE) trapping, which allows for passive spatial confinement of single nanoparticles in nanofluidic devices. In aqueous environments (pH > 2), glass and silicon dioxide surfaces acquire a net negative surface charge density due to the self-dissociation of terminal silanol groups. Thus, with native glass/silicon-based GIE-trapping devices, only negatively charged nano-objects can be trapped, limiting the applications of this method. In this work, we have performed surface modifications of glass-based GIE-trapping nanofluidic devices to enable the trapping of positively charged nanoparticles. For surface functionalization of the devices, a layer transfer of poly-(ethyleneimine) electrolytes was used, which provides a net positive surface charge density. We demonstrate the successful confinement of positively charged 60 nm gold nanoparticles inside the functionalized devices and present a comparison study between trapping of negatively- and positively charged particles in native and functionalized devices, respectively.

Keywords: Geometry-induced electrostatic trapping; Nanofluidic device, Contact-free trapping; Nanoparticles; Surface functionalization; Interference scattering detection method.

3.1 Introduction

Contact-free trapping and handling of single nano-objects in solution are of significant interest for potential applications in chemistry, biophysics, biotechnology, and clinical medicine¹⁷⁵. A contact-free trapped nano-object can be studied in a more controlled manner and for longer time intervals to provide information on local dynamics and on chemical or biological properties of the object of interest. Several active trapping methods, such as optical^{120,176}, magnetic^{177,178}, and acoustic tweezers^{179,180}, have demonstrated successful trapping of single objects ranging from ~ 10 nm to ~ 100 μ m in size^{120,181}. In these methods, the restoring force is proportional to their respective field gradient, to the volume of the trapped object, and other object properties such as polarizability (α) for optical tweezers, magnetic susceptibility for magnetic tweezers, and compressibility and density for acoustic tweezers^{120,181,182}. Reduction in the size of the trapped nano-object attenuates polarizability, susceptibility, and other volume dependent particle properties, which results in the requirement of very high field gradients. Thus, these methods are not very effective for smaller objects (< 100 nm). With relatively complex setups, optical tweezers allow for the trapping of nano-objects down to ~ 10 nm^{120,176,183-185} and a spatial resolution of a few Angstroms^{186,187}. An alternative to these methods is geometry-induced electrostatic (GIE) trapping, which allows for contact-free confinement of nano-objects down to tens of nanometers.^{112,113} GIE trapping is a passive confinement method in aqueous environments that is achieved through spatially modulated electrostatic potential wells by tailoring the surface of a nanofluidic device. The stiffness and stability of the electrostatic trapping are dependent on the charge of the confined object, the geometry of the system, and the concentration of the ionic buffer solution. Thus, it allows for the trapping of various particles ranging from single gold nanoparticles (Au NPs) to lipid vesicles independent of their mass.¹¹² Significant investigations were performed to achieve the immobilization of various objects in different geometries and orientations using GIE trapping.^{94,188}

GIE-trapping nanofluidic devices are mainly based on SiO₂ or glass substrate.^{112,113} The presence of silanol groups on selected substrates generates a negative surface charge density when the substrate is in contact with an aqueous solution ($\text{pH} > 2$) due to the deprotonation of terminal silanol groups.^{118,119} The resulting negatively charged surface causes the redistribution of coions and counterions in the aqueous solution, which leads to the formation of an electric double layer (EDL), as shown in Figure 3.1(a). In the presence of an EDL, the electrostatic potential decays linearly in the Stern layer and exponentially in the diffuse layer¹⁸⁹, where the electrostatic potential distribution beyond the Stern layer can be expressed by the Poisson-Boltzmann (PB) equation¹¹². When two charged surfaces are brought close to each other in a buffer solution, due to an overlap of the electrostatic potentials from both the surfaces, an electrostatic potential distribution is formed, where the minimum of the potential distribution lies in the middle of the two surfaces (Figure 3.1(b)). The presence of a potential minimum forces a negatively charged particle to acquire the lowest potential energy position at the midplane of the two surfaces. Tailoring the topography of one side of the fluidic device brings a shift in the location of potential minimum away from the midplane, which creates a local potential well and thus imposes confinement

of the particle towards the pocket, as shown in Figure 3.1(c). The difference of the potential energy inside the pocket and at the midplane of the two surfaces away from the pocket structure should be sufficiently higher than the thermal energy of the particle for a successful GIE trapping. The potential distribution in the presence of a nanopocket is shown in Figure 3.1(c), where the shift in the potential minimum can be seen clearly. The shape of the potential well inside the pocket

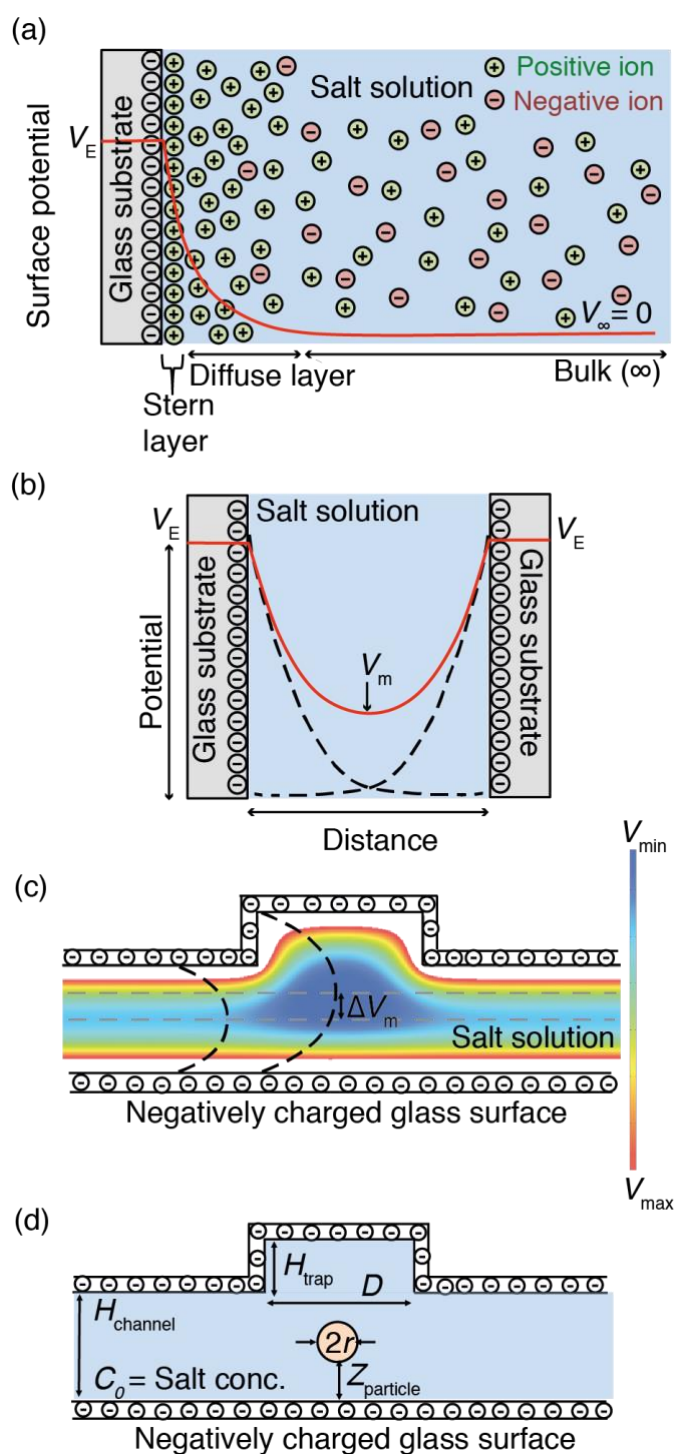


Figure 3.1 (a) Stern representation of an electrostatic potential distribution in an aqueous medium due to the self-dissociation of terminal silanol groups of the glass substrate. (b) Generation of a potential minimum in between two charged surfaces in an aqueous medium, from the overlap of two exponentially decaying electrostatic potentials. (c) Shift in the position of the electrostatic potential minimum, and the formation of a local potential well inside a nanopocket in the tailored topographic surface of the GIE-trapping device. (d) Parameters of a GIE-trapping device that directly influence the trapping stiffness of the particle inside the nanopocket.

can be tuned by geometric parameters of a GIE-trapping device, such as the channel height, trap height, and trap diameter, or by the salt concentration of the buffer solution inside the device as highlighted in Figure 3.1(d). A deeper electrostatic well gives high residence times, whereas a deeper and steeper potential well allows for a stiffer trapping for the confined particles.¹¹² To track the motion of a trapped object in the pockets, interferometric scattering detection (iSCAT) technique^{123,190} was employed in the present study. In several excellent studies, iSCAT has been shown to be a powerful technique for the observation of nano-objects such as Au NPs, viruses¹⁹¹, polymer beads, lipid vesicles^{94,112}, and motor proteins¹⁹². It relies on the coherent detection of the interference signal between the reflected light from the fixed geometries and elastically scattered light from the particles. Thus, iSCAT allows for simultaneous imaging of both the particle and the nanostructured surface.

In contrast to other trapping methods, GIE-trapping devices have been used exclusively for negatively charged objects to date. To employ GIE-trapping devices for positively charged particles, it entails modification of the device surface. Glass-based GIE-trapping devices in their native state allow only the trapping of negatively charged objects. In order to trap positively charged objects, an effective and stable functionalization of the inner surface of the device with a layer of a net positive surface charge density is needed.

In this work, we demonstrate the reliable contact-free trapping of positively charged Au NPs of 60 nm diameter in glass-based nanofluidic GIE-trapping devices. It is achieved by the functionalization of the device surface with positively charged polyelectrolytes to acquire a net positive surface charge density at the inner surface. We characterize the device performance by analyzing the particle lateral movements and comparing them to negatively charged Au NPs trapped in the non-functionalized glass-based devices. This work will further expand the possibilities for trapping and handling of nanoparticles and biomacromolecules that have a net positive surface charge.

3.2 Material and methods

3.2.1 Fabrication of glass-glass-based GIE-trapping device

GIE-trapping nanofluidic devices can be achieved from both silicon and glass substrates. However, in silicon-based devices, the highly reflective Si-SiO₂ interface brings in several detection challenges, whereas glass-based devices provide a high signal-to-noise ratio in iSCAT detection technique¹¹³. Therefore, in this work, we exploit glass-based GIE-trapping devices that are fabricated with conventional lithography processes on a 500- μ m-thick borosilicate glass wafer (Borofloat[®] 33, Plan Optik). A final device consists of two micro- and several nanofluidic channels with embedded nanopockets. The two microfluidic channels are connected by the nanofluidic GIE-trapping channels and thus allow in- and outflow of buffer and sample solutions, as shown in Figure 3.2.

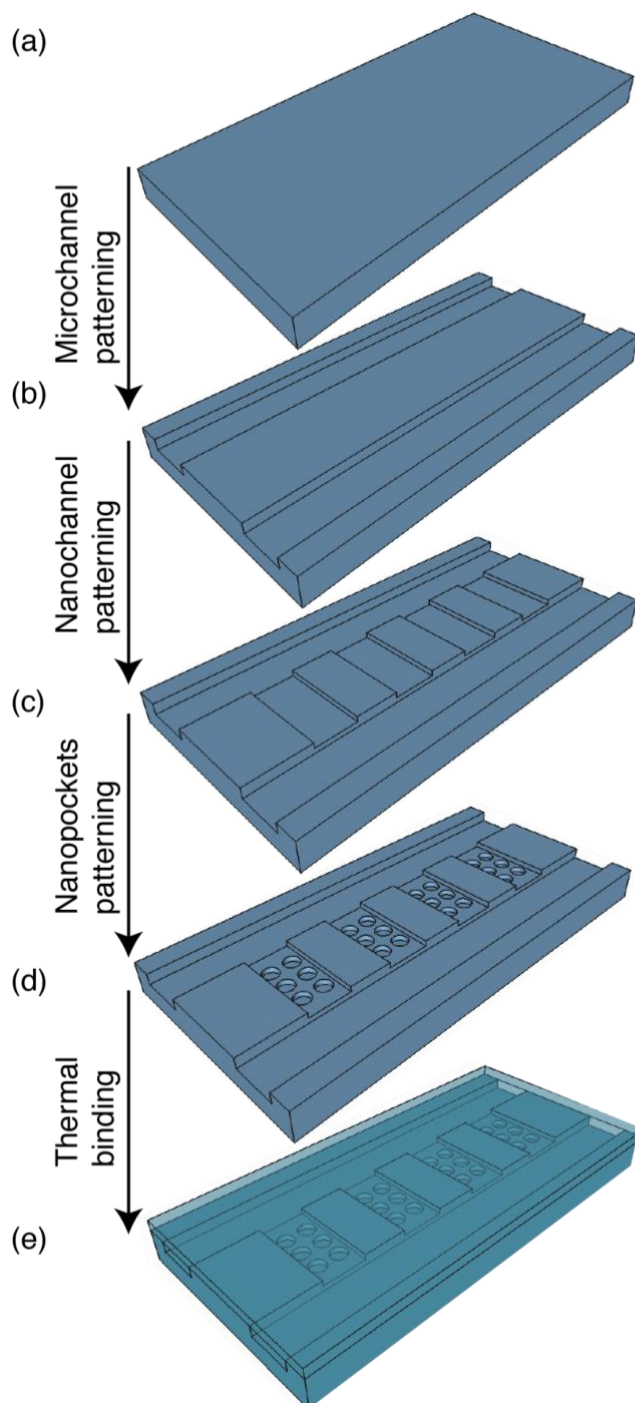


Figure 3.2 Schematics of fabrication steps of a glass-based nanofluidic GIE-trapping device. (a) Patterning of microchannels using optical lithography and buffer oxide etch (BOE 7:1) etching. (b) Patterning of nanochannels using e-beam lithography and reactive ion etching (RIE). (c) Patterning of nanopockets inside the nanochannels using e-beam lithography and RIE. (d) Thermal binding of coverslip glass and patterned glass surface.

The complete fabrication process was conducted in several steps. To start with, a wafer was cleaned with acetone in a sonication bath for 10 min and then with freshly prepared piranha

solution (H_2SO_4 (%) : H_2O_2 (%) = 2 : 1) for 20 min, which was followed by deionized (DI) water cleaning and drying under a nitrogen gas stream (N_2).

To pattern the microfluidic channels, a 5-nm-thick chromium (Cr) layer (adhesion layer), and a 150-nm-thick Au layer was evaporated (Univex 450, Cr rate: 1 \AA/s , Au rate: 1 \AA/s) on both sides of the wafer. Next, a photoresist (Microposit S1813, Shipley) was spin-coated on both sides of the wafer (2000 rpm, 500 rpm/s, 40 s) and baked after each coating at $115 \text{ }^\circ\text{C}$ for 90 s. Subsequently, the freshly coated and pre-baked side of the wafer was exposed to UV light (Suess MA 6, $\lambda = 365 \text{ nm}$, 120 mJ/cm^2) using a Cr mask with $200 \text{ }\mu\text{m}$ wide and 10 mm long microchannels. The exposed resist was afterward developed in MF-24A (Shipley, Megaposit MF-24A) for 40 s followed by DI rinsing and N_2 gas drying. The exposed pattern was transferred into the Au layer and the Cr layer using a gold etcher solution (200 g KI+50 g I_2 in 5 l DI water) for 90 s and a chromium etcher solution (Chrome Etch No. 1, Technic) for 15 s, respectively. The unprotected glass surface in the patterned region was etched in a 7 : 1 buffered oxide etch (BOE, General Chemical Corporation) solution for 6 h to achieve $10 \text{ }\mu\text{m}$ deep microchannels. During BOE etching, resist, Au, and Cr layer altogether worked as a protective layer for the unpatterned glass surface. In subsequent steps, the photoresist (S1813) was removed by sonication in acetone for 10 min, and the wafer was cleaned in piranha solution at $90 \text{ }^\circ\text{C}$ for 10 min followed by DI water rinsing and N_2 gas drying. The Au and Cr layers were removed in Au and Cr etcher solution, and the wafer was rigorously rinsed by DI water and dried under a N_2 gas stream.

Before the next patterning step, the wafer was cleaned once again in an acetone sonication bath for 10 min, a freshly prepared piranha solution for 20 min and subsequently rinsed with DI water and dried with N_2 gas. To etch the $2\text{-}30 \text{ }\mu\text{m}$ wide and 1 mm long nanofluidic channels in between the patterned microchannels, a 25-nm-thick Cr layer was evaporated (BAK 600 evaporator, 1 \AA/s) on the patterned surface to serve as a conducting layer for electron beam (e-beam) lithography (Vistec EBP 5000 Plus) and as a hard mask during reactive ion etching (RIE). The wafer was then spin-coated (4000 rpm, 500 rpm/s, 60 s) with a positive e-beam resist, i.e., poly-(methylmethacrylate) (PMMA 950 K, Allresist; 4% in ethylacetate), and pre-exposure baked at $175 \text{ }^\circ\text{C}$ for 4 min. The nanofluidic channels were exposed into the PMMA resist using e-beam lithography and developed in methyl-isobutyl-ketone: isopropyl alcohol (MIBK : IPA = 1 : 1) solution for 60 s. After transferring the nanochannels into the Cr layer using chlorine plasma etching (BMP Plasma Technology GmbH, O_2 : Cl_2 = 1 : 5), PMMA was removed by 10 min sonication in acetone followed by DI water cleaning and N_2 drying. The obtained nanochannels were further etched into the glass wafer by a SiO_2 etching process using RIE to get $70\text{-}200 \text{ nm}$ deep nanochannels (Oxford 100, Ar = 38 sccm, CHF_4 = 12 sccm, 100 W).

For the patterning of nanopockets inside the nanochannels, first, the Cr layer was removed by 10 min immersion in Cr etcher followed by rinsing with DI water and N_2 drying, and subsequently a new 15-nm-thick Cr layer was evaporated on the wafer. To pattern $100\text{-}500 \text{ nm}$ wide cylindrical pockets inside the nanochannels, PMMA was spin-coated on the wafer and exposed using e-beam lithography and then developed in MIBK : IPA (1 : 3) for 60 s. The

resultant nanopockets-pattern was transferred into the Cr hard mask using chlorine plasma etching, and afterward PMMA resist was removed by sonication in acetone. Using RIE these nanostructures were etched into the nanochannels, where the pocket-height was half of the nanochannel-height. The obtained nanopockets serve as the sites of local potential minima inside the nanochannels to confine the nanoparticles.

For further development of the device, the patterned wafer was coated with protection resist S1813 (3000 rpm, 500 rpm/s, 40 s, 90 s at 115 °C), and diced into 15×15 mm² sized devices, where every device had two microchannels, several nanochannels connecting the microchannels, and the embedded pockets in the nanofluidic channels. Diced chips were used to drill holes (1 mm-diamond drilling bits, Eternal Tools) at the starting and ending points of the microchannels to use these locations as inlet and outlet points. Drilled chips were further sonicated in acetone for 15 min to remove the protection resist and immersed in a piranha solution at 90 °C for 10 min followed by DI water rinsing. Afterward, the Cr layer was removed in Cr etcher solution (12 min), and the wafer was cleaned with DI water and dried under a N₂ gas stream.

To prepare GIE-trapping fluidic chambers, the chips were cleaned in a freshly prepared piranha solution for 20 min followed by DI water cleaning and then activated using ammonium hydroxide solution (28-30%) at ~40 °C for 40 min. Immediately after activation, the chips were aligned against similarly activated coverslip glasses of 150 μm thickness (Borosilicate glass, Plan Optik) and pressed overnight at a pressure of 390 kN/m². To bind the coverslip glass with the patterned chip covalently, the covered chips were placed into a thermal annealing furnace (Process Products Corporation) and heated up to 630 °C for thermal binding. For further details on the thermal binding process and used temperature profile, see reference^{113,193}. Four 1 ml needles were attached to the inlets and outlets of the patterned chip after shortening the hub opening to reduce the dead volume of the needles. For the present experiments, the microchannels of the GIE-trapping devices were connected to two tubings (PTFE tubing, Adtech) that are linked to buffer solution filled syringes.

3.2.2 Functionalization of GIE-trapping devices

GIE-trapping devices can be used for the trapping of negatively charged nanoparticles without additional surface modification. However, for the trapping of positively charged particles, the devices require an additional surface functionalization to obtain a positively charged surface. Several polyelectrolytes have been used to modify the surface charge of glass/silicon/PDMS substrates^{194,195}. Among these polyelectrolytes, poly-(ethyleneimine) (PEI) has been successfully used as a precursor layer to obtain a positively charged layer on silicon and PDMS substrates, which is further used to coat with the layers of other polyelectrolytes.¹⁹⁵ Thus, the surface functionalization was performed using branched poly(ethyleneimine) (PEI, M_w ~ 750,000, 50% (w/v) in H₂O, Sigma Aldrich). A solution of PEI in DI water was prepared with a final concentration of 20 mg/ml, which was then flushed through the nanochannels via microchannels, as shown in Figure 3.3. Capillary forces inside the nanostructures permit the solution to flow inside the nanochannels and nanopockets-¹⁹⁴ The GIE-trapping devices were

incubated with the solution for 3 h and then flushed with DI water overnight. DI water flushing of nanochannels occurs mainly by diffusion.¹⁹⁶ To prepare the device for the experiments, vacuum was applied to both microfluidic channels to remove the DI water. Further, one microfluidic channel was kept on vacuum overnight while leaving the second channel connected to a N₂ gas stream to remove the remaining water in the micro- and nanochannels.

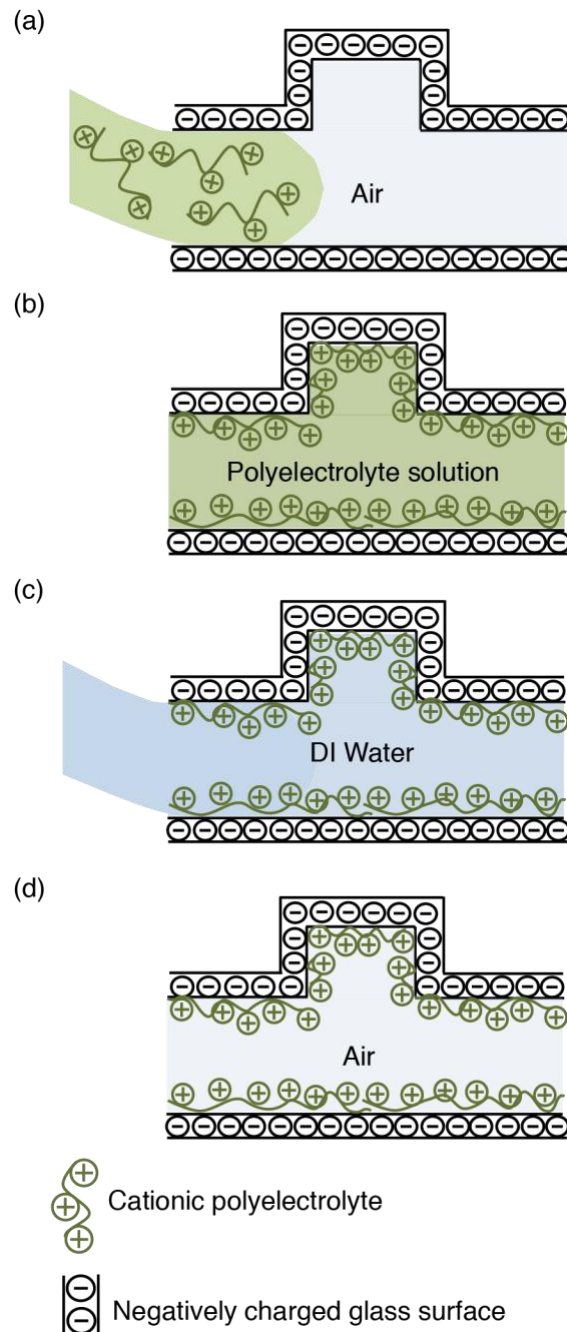


Figure 3.3 Schematics of the steps performed to functionalize the GIE-trapping device for positive particle trapping: (a) Introduction of polyelectrolyte solution in GIE-trapping device. (b) Adsorption of polyelectrolyte on the device walls. (c) Rinsing the nanochannels with DI water. (d) Drying of nanochannels using vacuum and N₂ gas flow.

3.2.3 Sample preparation

GIE-trapping experiments were performed for both negatively (BBI Solutions EM.GC60, size distribution with the coefficient of variation (CV) = 8%) and positively (nanoComposix, NanoXact 0.05 mg/ml, BPEI, CV = 15%) charged Au NPs in non-functionalized and functionalized devices, respectively. To exchange the buffer solution of the nanoparticles, 1 ml of Au NPs solution was centrifuged at 2000 rpm in a tabletop centrifuge for 20 min. The supernatant was removed, and the resultant pellet was resuspended in 1 ml of DI water by pipetting. The solution was further centrifuged (2000 rpm, 20 min), and after discarding the supernatant, the pellet was again dispersed in 1 ml of DI water. To obtain the final sample, the solution was centrifuged, and after disposing of the supernatant, the resultant pellet was suspended in $\sim 20 \mu\text{l}$ DI water to obtain a concentrated solution of Au NPs with about 10^{11} particles/ml. The resulting solution of Au NPs was then used for trapping experiments. During the experiments, the samples were always prepared fresh, i.e., ~ 1 h before each experiment to avoid the aggregation of nanoparticles.

3.2.4 Experimental setup

To map the motion of confined nanoparticles with high spatiotemporal resolution, the experiments were performed on an inverted optical microscope (DMI 5000 M, Leica), which is connected to a home-built iSCAT system consisting of a 300 mW, 532 nm emission wavelength solid-state laser (MGL-III-532, CNILaser), two-axis deflection mirrors running at 1kHz frequency (GVS002, Thorlabs Inc.), and a CMOS camera (MV-D1024-160-CL-12, Photon Focus)¹¹³. Imaging was carried out using a $100\times$ 1.3 NA (oil) objective lens in combination with a $1.5\times$ tube lens (Leica). To control the image acquisition and deflection of mirrors, both mirrors and camera were synchronized by a four-channel AO-LabView controller (cDAQ-9171/NI 9269, LabView) and operated using a custom-built LabView-platform. Images were collected at 1 ms and 10 ms exposure time with an acquisition rate of 111 Hz and 90 Hz, respectively. The laser beam used for imaging has a half-power-beam-width of $4.3 \mu\text{m}$. Thus, in the case of 1 ms exposure time, the laser was scanned only once on the focal plane for the detection of a nanoparticle inside a nanopocket. Further analysis of particle tracking and stiffness calculations was performed in Matlab.

3.3 Results and discussion

3.3.1 Trapping negatively charged particles

In the absence of a functionalized inner surface, glass-based GIE-trapping devices can solely be employed for the trapping of negatively charged particles. For device characterization, experiments were performed using negatively charged Au NPs with a diameter of 60 nm. During the experiment, DI water ($18 \text{ M}\Omega/\text{cm}^{-1}$) was used as the buffer solution and was constantly flowed through the microfluidic channels. In Figure 3.4(a) an iSCAT image of several individually trapped particles in an array of nanopockets ($D = 250 \text{ nm}$, $H_{\text{trap}} = 75 \text{ nm}$,

$H_{\text{channel}} = 150 \text{ nm}$) is shown. Some of the pockets still remain empty (marked by blue circles) depending on the initial concentration of the particles used during the experiments. Due to constructive interference of light reflected by the substrate and scattered by the inner surface of the pocket, empty pockets appear as low-intensity bright spots.

For stiffness measurements, single particles were recorded at a 1 ms exposure time and an acquisition rate of 111 Hz (Figure 3.4 (a) magnified image). Each collected image was fitted to a Gaussian profile to obtain the center of the particle as a means to monitor its trajectory. An exemplary lateral displacement plot of a recorded particle is shown in Figure 3.4(b). The lateral motion plots were used for the

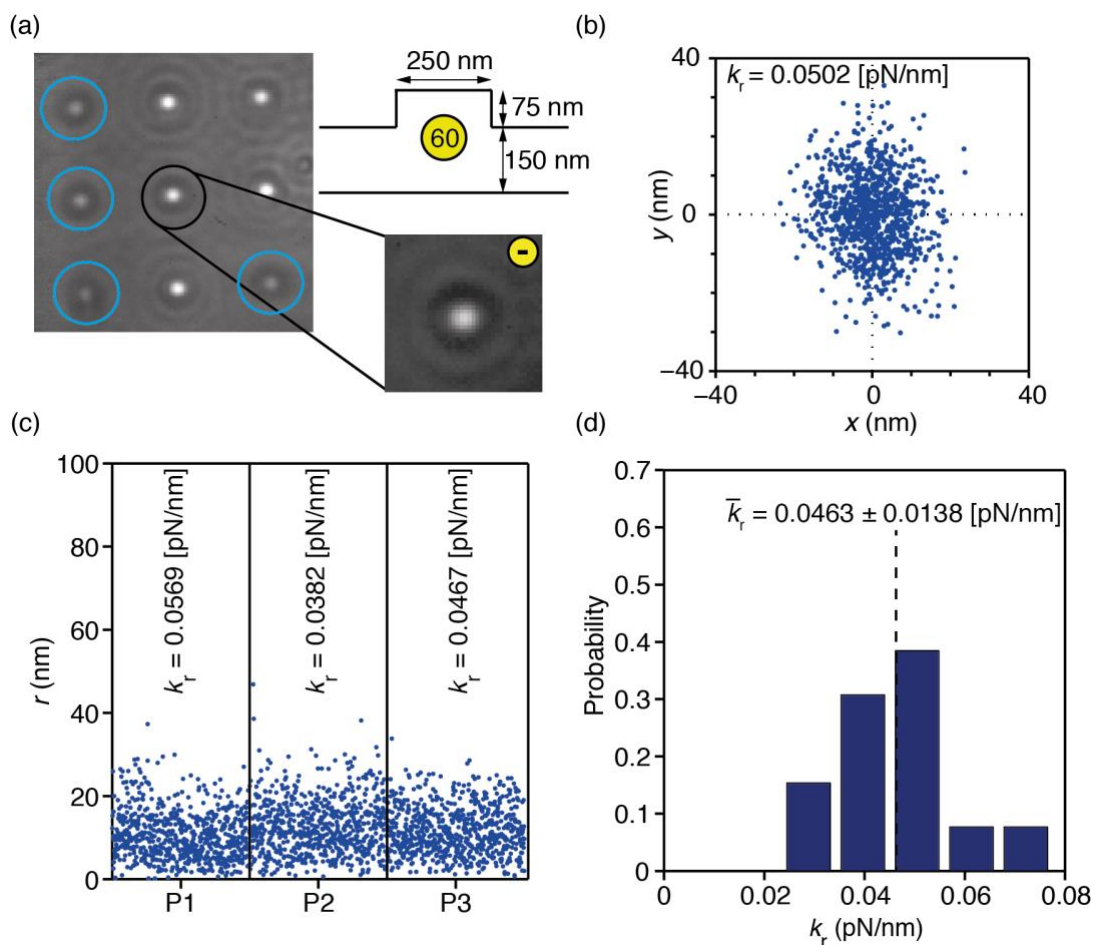


Figure 3.4 Negative particle trapping in GIE-trapping glass-based device: (a) Trapping of 60 nm negatively charged single gold nanoparticles in 250 nm wide and 75 nm high pockets inside 150 nm high nanochannels. Nanopockets with trapped single particle are visible by a bright spot in the middle of the nanopocket whereas empty pockets are visible by very low intensity (shown in blue circle). The inset has shown the zoomed in trapped single particle in the nanopocket. (b) Lateral movement of the trapped particle inside the nanopocket is shown by scattering plot. Corresponding stiffness constant (k_r) of the particle is 0.0502 pN/nm. (c) Lateral displacement of several trapped particles is analyzed to characterize the trapping efficiency of the device. (d) Resultant values for stiffness constant and their probability in the observed particles, where average stiffness values is $0.0463 \pm 0.0138 \text{ pN/nm}$.

calculation of mean square displacement (MSD), $\langle [\Delta r(\Delta t)]^2 \rangle$, where $r = \sqrt{x^2 + y^2}$, as a function of time interval Δt . For a confined particle, the MSD value reaches a plateau for time intervals that are much longer than the relaxation time of the particle in the potential well¹²⁷. The value of MSD at the plateau, $\langle [\Delta r]_p^2 \rangle$, is directly correlated to the radial stiffness constant (k_r) for the particle inside the electrostatic potential trap by $\langle [\Delta r]_p^2 \rangle = 4k_B T / k_r$ ^{110,197,198}, where k_B is the Boltzmann constant, and T the room temperature. Thus, the spread of the scatter plot of a trapped particle directly correlates to the stiffness constant value. Due to the symmetry of cylindrical nanopockets, a symmetric scattering plot was obtained during GIE trapping of a particle inside the electrostatic potential well. Figure 3.4(c) illustrates the radial fluctuations of a few single particles (P1-P3) trapped inside the 250 nm pockets. The maximum radial displacement observed in the GIE trapping of negatively charged particles varies from ~ 30 nm for strongly trapped particle to ~ 50 nm for a relatively weakly trapped particle. Associated trapping stiffness ranges from 0.023 pN/nm to 0.077 pN/nm with average stiffness constant $\bar{k}_r = 0.0463 \pm 0.0138$ pN/nm, as shown in Figure 3.4(d). The spread in the values of stiffness constant and their probability is illustrated in Figure 3.4(d). The difference between the particle-potential energy inside the trap and the midplane of the nanochannel, away from the pocket, must be higher than the thermal energy of the particle for successful trapping. Hence, the selected dimensions of the nanopockets and the nanochannels fulfill this requirement in the used nanofluidic devices. However, the observed variations in the stiffness constant of trapped Au NPs might arise from the fluctuations in the particle diameter or net particle charge inside the solution.

3.3.2 Trapping positively charged particles

A glass-based GIE-trapping device was functionalized with PEI solution (Section 3.2.2) for the trapping of positively charged 60 nm Au NPs. After functionalization, the inner surface of the GIE-trapping device attains a net positive surface charge density. In Figure 3.5(a), the trapping of a positively charged Au NP inside a nanopocket ($D = 250$ nm, $H_{\text{trap}} = 75$ nm) is shown. The nanopockets were embedded in a nanochannel with a height of $H_{\text{channel}} = 150$ nm. The scatter plot obtained from a trapped charged single nanoparticle, as shown in Figure 3.5(b), demonstrates the lateral deviation of a positively charged particle from the center of the pocket, which directly refers to the strength of the electrostatic potential in the pocket. The radial motions of sample particles in the vicinity of the pocket center are shown in Figure 3.5(c), which demonstrate successful trapping of positively charged particles inside an electrostatic potential well. Here, the radial stiffness ranged from 0.0083 pN/nm to 0.0379 pN/nm in pockets of similar dimensions as for negatively charged particles. In comparison to the mean trapping stiffness (0.0463 ± 0.0138 pN/nm) observed for negatively charged particles in a non-functionalized GIE-trapping device, positive particles show comparable stiffness values (0.0266 ± 0.0160 pN/nm), as shown in Figure 3.5(d). Average radial stiffness values for positive particles was slightly lower than for negative particles, which might be because of differences in surface charge density of negatively and positively charged particles and differences in surface charge density of the functionalized (20-25 microequivalents per gram)¹⁹⁹ and non-functionalized glass surface ($\sim 10^{17}$ e/m²)¹¹⁵.

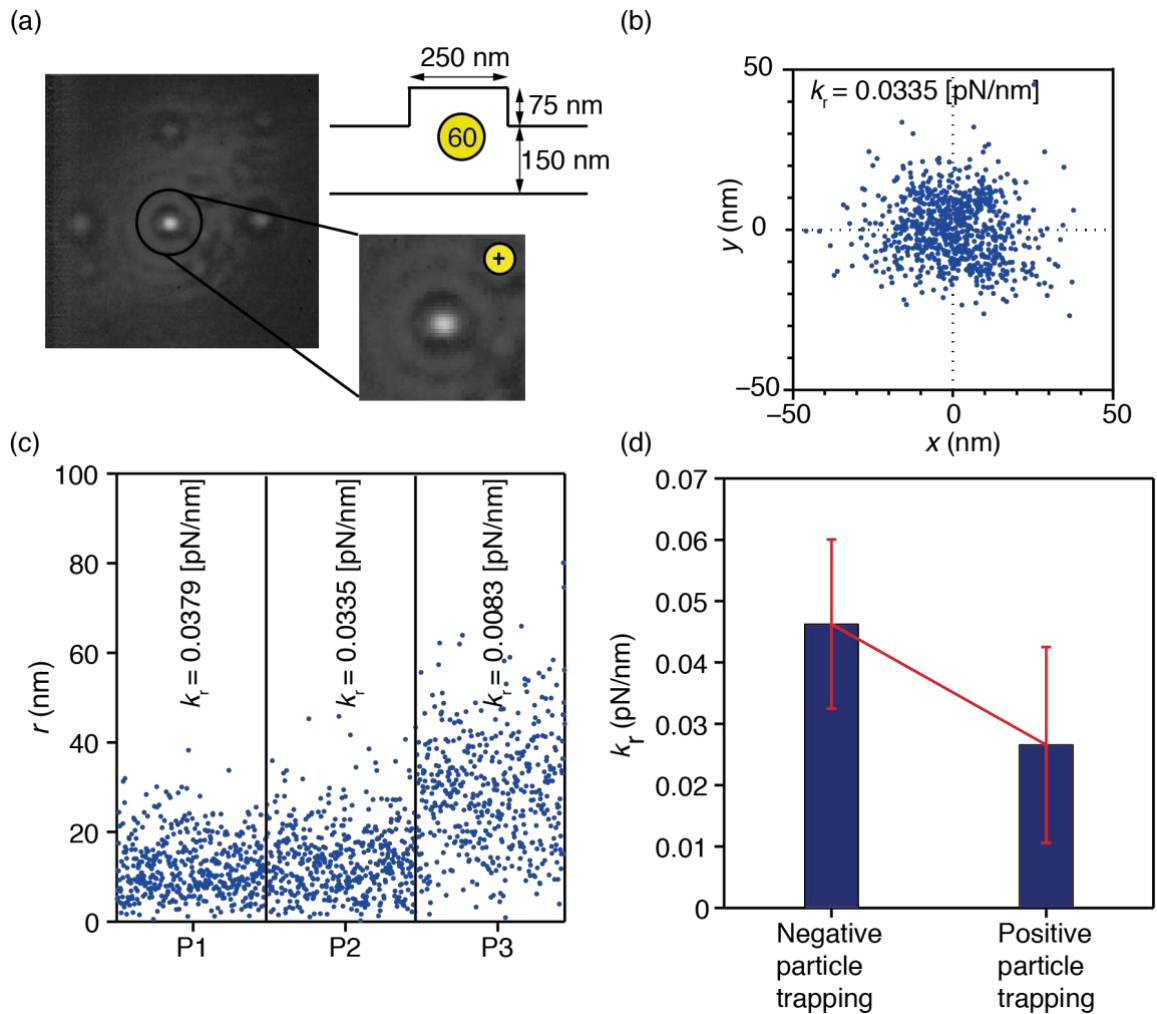


Figure 3.5 Positive particle trapping in modified GIE-trapping device: (a) Trapping of single 60 nm positively charged gold nanoparticle in a functionalized GIE-trapping device. The inset shows the trapped particle inside a 250 nm diameter and 75 nm high pocket embedded in a 150 nm high nanochannel. (b) Scattering plot of a trapped particle in x - and y -direction with stiffness constant (k_r) 0.0335 [pN/nm]. (c) Exemplary particles to show the variation in the GIE-trapping of positive particles. (d) A comparison of the average stiffness constant obtained in negatively and positively charged particle trapping in non-functionalized and functionalized devices, respectively.

Apart from contact-free confinement of single positive Au NPs, we also observed some particles that did not attend the center position of the pocket and stayed around the outer ring of the pocket, as shown in the lateral displacement plot in Figure 3.6. The confinement of the particle away from the center position demonstrates that it is not a conventional GIE trapping where a particle stays inside the potential well. The non-symmetric confinement might arise due to an inhomogeneous functionalized pocket surface and thus attractive forces from the negatively charged SiO₂ surface or due to the interaction of protruded polymer chains with the particle in the presence of rough functionalized surfaces.

Overall, our results show that trapping of single positively charged Au NPs was obtained after functionalizing the inner surface of the device by a cationic polyelectrolyte. To further realize

optimal surface charge densities and surface roughness for the functionalized glass surfaces, optimum polyelectrolyte solution concentrations and incubation times need to be achieved. Additionally, multilayer functionalization with three polyelectrolytes (positive-negative-positive) could improve the homogeneity of the surface charge distribution as well as increase the trapping strength for positively charged Au NPs.¹⁹⁴

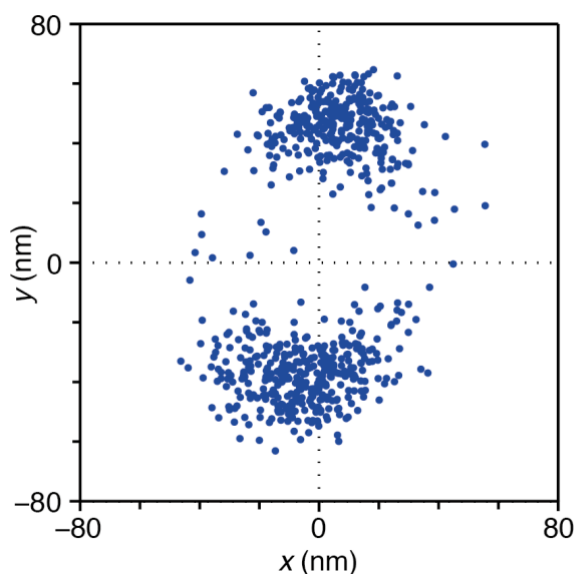


Figure 3.6 Scattering plot of a 60 nm diameter particle to show the lateral deviation inside a 200 nm diameter pocket. It shows the motion of the particle away from the center and along the boundary of the pocket.

3.4 Conclusions

In this work, we presented the fabrication of glass-based GIE-trapping fluidic devices. The GIE-trapping devices are employed to demonstrate the successful trapping of negatively charged Au NPs with 60 nm diameter. To broaden the applications of GIE-trapping devices, we introduced a polyelectrolyte-based functionalization of the nanostructures in the fluidic device, which enabled the successful GIE trapping of single positively charged Au NPs with 60 nm diameter. However, in comparison to negatively charged particle trapping in non-coated glass-based nanofluidic devices, the functionalized devices require further characterization and optimization to achieve stronger and more homogenous trapping inside the nanochannels. The feasibility of trapping both negatively and positively charged particle in GIE-trapping fluidic devices expands the applicability of the device to positively charged nano-objects, such as metallic nanoparticles, polymer beads, biomolecules, viruses and proteins.

Acknowledgments

This work is funded by the Swiss Nanoscience Institute, Basel, Switzerland (SNI PhD Graduate School) under the project P1310. We would like to thank Konrad Vogelsang, Stefan Stutz and the technical staff of the Laboratory for Micro- and Nanotechnology, PSI Villigen, Switzerland, for their technical support. We are also thankful to Dr. Celestino Padeste, Dr. Vitaliy Guzenko and Dario Marty for providing working space for chemistry work, guidance in the e-beam patterning, and help in the cleanroom steps.

Chapter 4. Surface-Modified Elastomeric Nanofluidic Devices for Single Nanoparticle Trapping

Deepika Sharma^{1,2,3†}, Roderick Y.H. Lim^{1,2}, Thomas Pfohl^{1,4†}, Yasin Ekinci^{1,3†}

¹ Swiss Nanoscience Institute, Basel 4056, Switzerland

² Biozentrum, University of Basel, 4056, Basel, Switzerland

³ Laboratory for Micro and Nanotechnology, Paul Scherrer Institut, 5232, Villigen, Switzerland

⁴ Institute of Physics, University of Freiburg, 79104, Freiburg, Germany

† Authors to whom correspondence should be addressed.

ABSTRACT

Our work focuses on the development of simpler and effective production of nanofluidic devices for high-throughput charged single nanoparticle trapping in an aqueous environment. Single nanoparticle confinement using electrostatic trapping has been an effective approach to study the fundamental properties of charged molecules under a controlled aqueous environment. Conventionally, geometry-induced electrostatic trapping devices are fabricated using SiO_x-based substrates and comprise nanochannels embedded with nanoindentations such as nanopockets, nanoslits, and nanogrids. These geometry-induced electrostatic trapping devices can only trap negatively charged particles, and therefore, to trap positively charged particles, modification of the device surface is required. However, the surface modification process of a nanofluidic device is cumbersome and time-consuming. Therefore, here, we present a novel approach for the development of surface-modified geometry-induced electrostatic trapping devices that reduces the surface modification time from nearly 5 days to just a few hours. We utilized polydimethylsiloxane for the development of a surface-modified geometry-induced electrostatic trapping device. To demonstrate the device efficiency and success of the surface modification procedure, a comparison study between a PDMS-based GIE-trapping device and the surface-modified polydimethylsiloxane-based device was performed. The device surface was modified with two layers of polyelectrolytes (1: poly(ethyleneimine) and 2: poly(styrenesulfonate)), which led to an overall negatively charged surface. Our experiments revealed the presence of a homogeneous surface charge density inside the fluidic devices and equivalent trapping strengths for the surface-modified and native polydimethylsiloxane-based geometry-induced electrostatic trapping devices. This work paves the way towards broader use of geometry-induced electrostatic trapping devices in the fields of biosensing, disease diagnosis, molecular analysis, fluid quality control, and pathogen detection.

KEYWORDS: functionalized devices, geometry-induced electrostatic trapping, nanofluidics, soft lithography, polyelectrolytes

4.1 Introduction

High-throughput contact-free trapping of individual nano-objects aqueous media has immense importance for dynamic, chemical, physical, and biological studies. Over the past decades, several techniques for single-particle studies have been introduced, allowing either active or passive confinement of single objects. Contact-free confinement of an object enables its trapping in an aqueous solution without its physical contact with adjacent surfaces of the device and thereby allows a better way of studying and understanding the dynamics of particles and their physical and chemical properties. Thus, it provides a robust means for investigating molecular activities, diagnostic efficiency, and material characteristics.

Conventional active particle confinement methods, such as optical tweezers^{120,176,185}, magnetic tweezers²⁰⁰⁻²⁰², and dielectrophoretic trapping^{203,204}, provide direct control of the trapping strength and manipulation of the particle position. However, the particle trapping strength in the aforementioned methods is dependent on various properties of the particle, such as the refractive index, permeability, and permittivity with respect to its surroundings, and is also proportional to the particle volume and field gradients. Thus, as the particle size decreases to the nanoscale, exceedingly large applied fields are required to confine it. Furthermore, the freedom of manipulating trap locations in active methods requires a complex setup and an external field source. Recently, some other active trapping methods were introduced to achieve particle confinement under ambient conditions for extended periods, such as anti-Brownian electrokinetic (ABEL) trapping²⁰⁵⁻²⁰⁷. To avoid system complexity and the presence of external field gradients, passive trapping methods such as hydrodynamic trapping, convex lens-induced confinement (CLIC)²⁰⁸⁻²¹⁰, and geometry-induced electrostatic (GIE) trapping¹¹² were introduced, which allow single particle confinement in an integrated micro/nanofluidic device based on the device geometry and the device surface and particle interactions.

Among various methods, GIE trapping has shown the potential to be a robust method for stable high-throughput contact-free confinement of nanoparticles down to 1 nm in diameter in an aqueous solution without the requirement of any external field.^{112,211-213} GIE-trapping inside a nanofluidic device is achieved using the electrostatic interactions between charged device surfaces and like-charged nano-objects. Due to the repulsive forces between the like-charged device surface and the charged particle, a nanoparticle levitates inside the fluidic device at specifically tailored nanoscopic locations.⁸⁵ Tailoring the topography of one surface of a fluidic device with nanoindentations generates nanoscopic electrostatic potential traps between the two surfaces and allows nanoparticle trapping inside the nanoindentations.^{85,112} For radial-symmetric electrostatic potential traps inside a fluidic device, one device surface is patterned with nanochannels embedded with cylindrical nanopockets, which leads to the formation of potential wells inside the nanopockets.⁸⁵

Conventionally, GIE-trapping devices are fabricated using glass or silicon substrates, which acquire a negative surface charge density in an aqueous environment ($\text{pH} > 2.4$) due to self-deprotonation of silanol (Si-OH) groups at the surface.^{118,119,214} Since the GIE-trapping devices

can confine only like-charged nano-objects in a contact-free manner, SiO_x-based GIE-trapping devices can only be used for negatively charged nanoparticles. To utilize these devices for positively charged nano-objects and broaden the scope of GIE trapping, the device surface has to be modified to acquire a net positive surface charge density. We have previously reported positive single nanoparticle trapping in a surface-modified glass-based GIE-trapping device, where a conventional glass-based integrated nanofluidic device was functionalized using polyelectrolyte solution.⁸⁵ However, the surface modification of a glass-based nanofluidic devices is a cumbersome and time consuming, since the introduction and exchange of solutions rely on capillary action and diffusion of liquid molecules, respectively. Here, we report on overcoming this issue using polydimethylsiloxane (PDMS)-based integrated nanofluidic devices that allow faster multilayer functionalization and alteration of the surface electrostatic charge. Soft-elastomeric GIE-trapping devices reduce both the fabrication time and functionalization time from nearly 5 days to just a few hours, leading to a nearly one order of magnitude change in time. Surface modification of PDMS-based devices can be performed in minutes, opening up a new possibility of selective functionalization of device surfaces for charge-selective and area-specific trapping of charged nanoparticles. It can also be used to separate positively and negatively charged nanoparticles before trapping, which can work as a particle separation machine. Furthermore, PDMS-based devices enable tunable trapping and release of nanoparticles during experiments owing to the low elastic modulus of PDMS.^{125,215,216} This allows the study of multiple batches of particles with the same GIE-trapping device, giving more statistical information during a single experiment. Other chemical and physical properties of PDMS, such as the biocompatibility, gas permeability, and optical transparency, further enable these devices to be used in drug discovery, biosensing, and disease diagnosis.

In this report, we present fabrication and multilayer surface functionalization procedures for PDMS-based GIE-trapping devices and their usage in the single particle trapping for negatively charged nanoparticles. A comparison of experimental and numerically calculated particle trapping results is presented along with the impact of the size of the nanopocket in single nanoparticle GIE trapping. The novelty of this work lies in the following areas:

1. Functionalization of PDMS-based nanofluidic devices to alter the surface charge density of the device surface.
2. Simplification of the functionalized GIE-trapping devices for high-throughput particle trapping.
3. Improvement of the production of functionalized GIE-trapping devices for positively charged particle trapping.
4. Opening up of the selective surface functionalization prospects of a nanofluidic device for GIE trapping of both positively and negatively charged particles.

4.2 Materials and Methods

4.2.1 Device Patterning and Replica Molding

The devices reported here are PDMS-based GIE-trapping devices that were manufactured using replica molding^{48,217,218}. For PDMS replica molding, a glass-based master was patterned using a combination of optical lithography, electron beam (e-beam) lithography, reactive ion etching (RIE), buffered oxide etching (BOE), and wet etching, as illustrated in Figure 4.1. The detailed fabrication process for the patterned glass surface was described in our previous work⁸⁵. The patterned glass master had dimensions of $15 \times 15 \text{ mm}^2$ and contained two $200 \mu\text{m}$ wide and $11 \mu\text{m}$ deep buffer supply channels with in/out ports at both ends. Both supply channels were connected by multiple 1 mm long nanochannels embedded with cylindrical nanopockets, as shown in Figure 4.2. The nanochannels were approximately 160 nm deep and $30 \mu\text{m}$ wide with embedded nanopockets of diameters of 200 nm and 500 nm and a pocket-depth of 100 nm .

The patterned glass master was used for replica molding of a negative polymer master, as demonstrated in Figure 4.1. Before using the glass master for replica molding of a negative master, gas phase silane deposition was performed on the glass master in a vacuum chamber using a mixture of 1:1 trichloro(1H,1H,2H,2H-perfluorooctyl)silane and (tridecafluoro-1,1,2,2-tetrahydrooctyl)dimethylchlorosilane. Silanization reduces the surface energy of the glass master, which allows easy removal of the glass master and negative polymer master after replica molding. For negative replica molding of the glass master, a $20 \times 20 \text{ mm}^2$ cover glass ($700 \mu\text{m}$ thick BOROFLUAT[®]33 glass, SCHOTT Advanced Optics) was cleaned by sonication in acetone and isopropyl alcohol (IPA) for 10 min each, dried under a N_2 stream, and oxygen plasma cleaned for 2 min (power = 150 W, pressure = 150 mTorr, O_2 flow = 20 sccm, Oxford Instruments - Plasmalab80Plus). After cleaning, the cover glass was spin-coated with OrmoPrime08 (45 s, 4000 rpm (rotation per minute), 3000 rpm/s, Micro resist technology GmbH) and baked for 5 min at $180 \text{ }^\circ\text{C}$.

To obtain a negative polymer master, a UV-curable resin, OrmoComp[®] (Micro resist technology GmbH), was drop-cast on the glass master, and immediately after that, an OrmoPrime08-coated cover glass was gently placed on the top of the drop; the drop was left to spread and fill inside the patterned micro- and nanostructures of the glass master. Once OrmoComp[®] filled the inside of the patterned structures, the assembly was placed in a UV chamber (ELC-500, light exposure system, Electro Life Corporation) for UV exposure (30 mW/cm^2 for $\sim 10 \text{ min}$). After UV curing, the glass master was removed gently, leaving cured resist stuck to the primer-coated cover glass. The negative OrmoComp[®] master was further silanized using the same procedure as for the glass master and further used for PDMS replica molding.

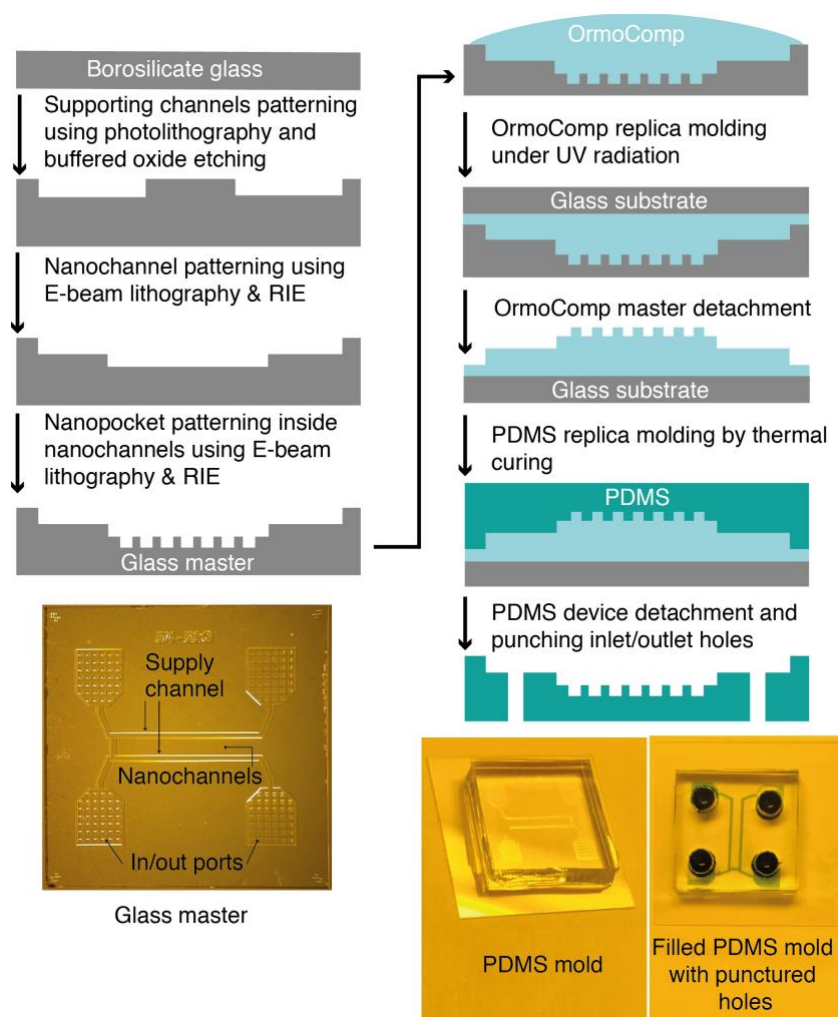


Figure 4.1 Schematics of the glass-master fabrication process in the left column and PDMS replica molding from the glass master using UV-curable resist OrmoComp[®] in the right column. Supply channels and in/out ports for the glass master are indicated with arrows. To inject a particle solution into the supply channels and nanochannels, 3 mm wide holes are punched at the location of supply ports.

To mold nanostructures of the master into PDMS, a high elastic modulus ($\sim 4\text{-}10$ MPa) polymer is typically required⁴⁸; thus, a 5 : 1 mass ratio mixture of the base polymer (SYLGARD[®] 184, silicon elastomer base, Dow Corning) and curing agent (SYLGARD[®] 184, silicon elastomer curing agent, Dow Corning) was prepared to achieve an elastic modulus of ~ 3.6 MPa for cross-linked PDMS^{215,219}, degassed and poured on the OrmoComp[®] master. PDMS was further cured at 150 °C for 2 h in a digital oven (Salvis Lab) in a uniform and controlled thermal environment. After curing the PDMS mold, the oven was switched off, and samples were allowed to cool down first inside the oven for 40 min and later outside the oven at room temperature. After cooling, PDMS molds were gently separated from the OrmoComp[®] master. Inlet/outlet holes (3 mm in diameter) were punched in the PDMS mold, as shown in Figure 4.1.

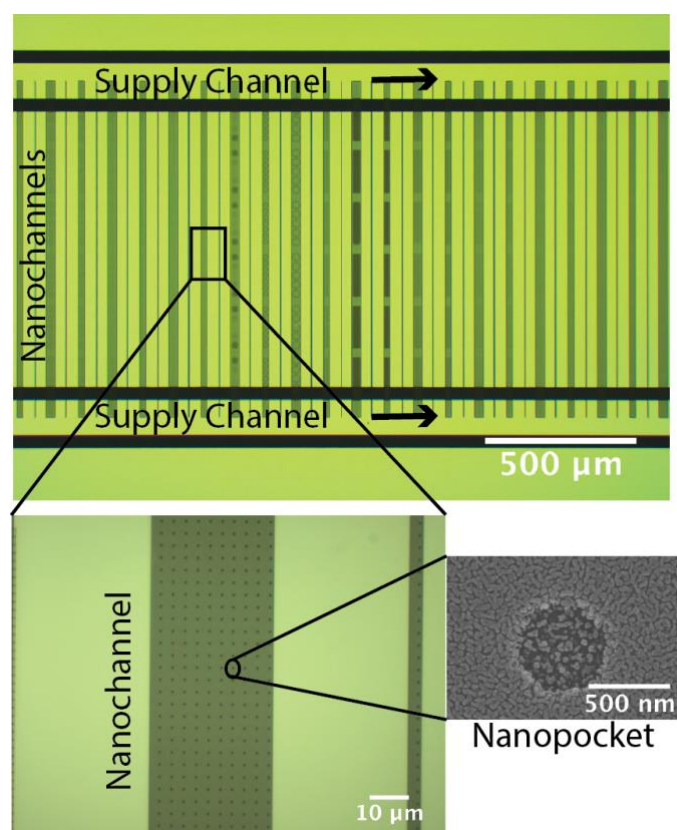


Figure 4.2 Patterned glass substrate with supply channels connected to multiple nanochannels embedded with nanoindentations of different geometries along with circular nanopockets with diameters of 200 nm and 500 nm.

4.2.2 Particle Sample Preparation

Experiments for single particle electrostatic trapping were conducted using negatively charged gold nanoparticles (Au NPs) with a diameter of 80 nm (BBI Solutions, EM.GC80). The purchased gold nanoparticles had intrinsic $-\text{COOH}$ functional groups present on the particle surface. These $-\text{COOH}$ groups are exposed to the environment and dissociate into H^+ and $-\text{COO}^-$ in the aqueous solution, providing a net negative surface charge density to the nanoparticle.

Sample solutions for experiments were prepared using 1 ml of negatively charged 80 nm Au NP solution in a 1.5 ml Eppendorf tube (RNase-free Microfuge tubes, Thermo Fisher Scientific). Nanoparticles were washed by exchanging particle buffer solution with DI water in the following steps: (i) centrifuge the solution at a 2000 relative centrifugal force (rcf) for 20 mins; (ii) discard the supernatant, and resuspend the pellet in 1 ml of DI water; and (iii) repeat the previous cleaning steps (i – ii) two times, and in the last step, resuspend the pellet in 50 μl of DI water instead of 1 ml. The prepared solution had a $\sim 0.02 - 0.05$ mM salt concentration remaining from the particle buffer solution and $\sim 10^{12}$ particles/ml.

4.2.3 Non-functionalized PDMS Device

The PDMS-based GIE-trapping device was made of an assembly of a patterned PDMS mold and two cover glasses (ROTH KARLSRUHE, 200 Deckgläser, 20 × 20 mm, #1), as shown in Figure 4.3. Prior to device assembly and functionalization, cover glasses were cleaned by sonication in acetone (15 min), IPA (15 min), and DI water (15 min) sequentially. Immediately after this step, the cover glasses were immersed for 20 min in a freshly prepared piranha solution, which was a mixture of 2 : 1 sulfuric acid (H₂SO₄) and 30% hydrogen peroxide (H₂O₂), then the cover glasses were thoroughly washed under DI water jet, and later dried under nitrogen (N₂) gas stream.

In the case of native (nonfunctionalized) PDMS devices, both the PDMS mold and the cleaned cover glasses were air-plasma activated (~ 42 s, 80% power - full power 100 W, 1.0 mbar, Diener electronic, Femto). Within 2 min, nanochannels of the patterned PDMS mold were filled with 0.25 µl of particle solution and placed on a cover glass, keeping the patterned side down. To achieve strong covalent PDMS-glass binding, the PDMS mold was pressed gently. Immediately after that, all inlet/outlets were filled with the buffer solution to avoid drying of the nanochannels. After inlet/outlet filling, the other cleaned air-plasma activated cover glass was placed on top of the PDMS mold to avoid evaporation of solution from inlet/outlet ports, as shown in Figure 4.3. The obtained device with filled particle solution was directly used for the experiment ~ 45 min after preparation to allow the solution to reach an equilibrium state.

4.2.4 Functionalized PDMS Device

A PDMS mold acquires a negative surface charge density in the presence of an aqueous solution due to the self-dissociation of terminal silanol groups^{115,117}. The acquired negative surface charge density permits contact-free electrostatic trapping only for negatively charged nano-objects. To use the same device for positive-particle confinement, the net surface electric charge needs to be changed to positive by surface functionalization⁸⁵. For a homogeneous surface charge density, multilayers of alternating cationic and anionic polyelectrolytes can be used for surface functionalization¹⁹⁴. To compare the GIE-trapping efficiency of the functionalized device with that of the original device, we performed surface functionalization to change the surface charge first from negative to positive and then from positive to negative. Thus, we used two layers of polyelectrolytes, poly(ethyleneimine) (PEI) and poly(styrenesulfonate) (PSS), to attain a homogeneous and long-lasting negative surface charge density inside the PDMS GIE-trapping device, as shown in Figure 4.3. The combination of PEI, a weak positive polyelectrolyte, and PSS, a strong negative polyelectrolyte, has been proven to form a stable polyelectrolyte bilayer with a self-healing property²²⁰.

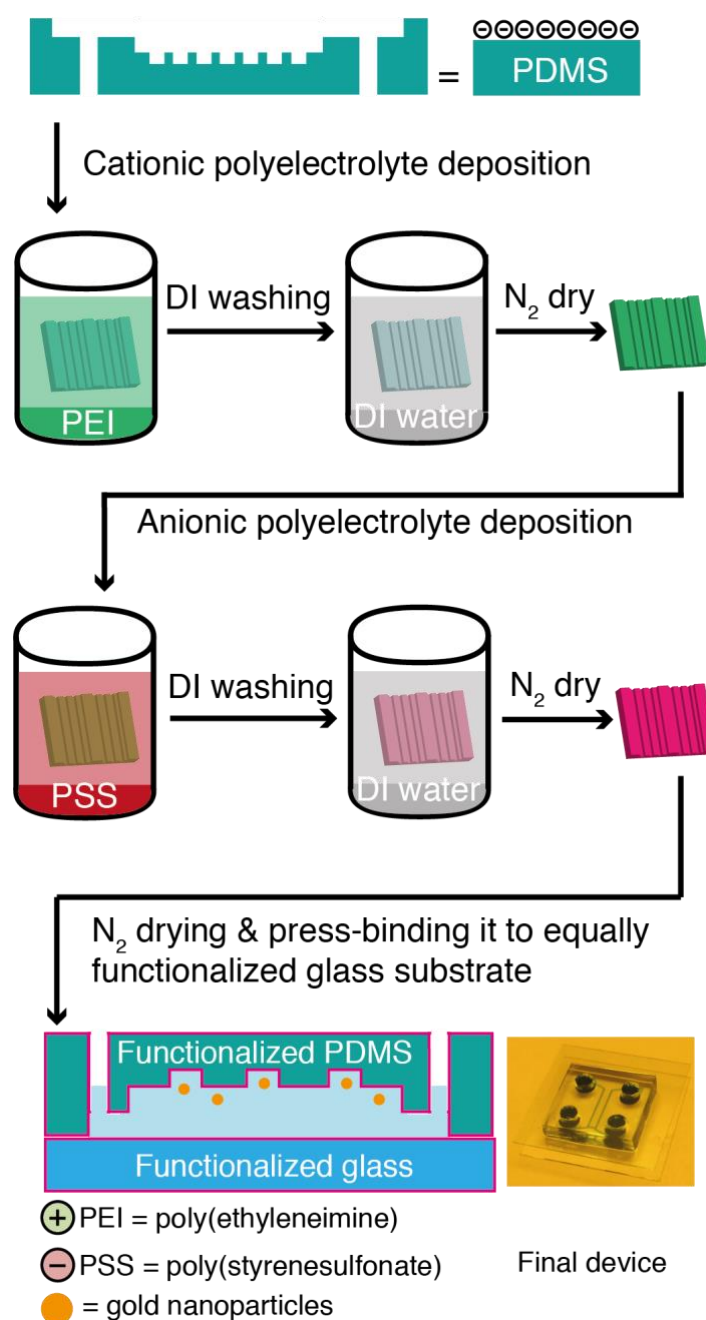


Figure 4.3 Schematics of the surface functionalization process for the polydimethylsiloxane-based nanofluidic device using cationic and anionic polyelectrolytes.

To achieve uniform surface functionalization and homogeneous surface charge density inside the PDMS-based GIE-trapping device, one PDMS mold and two cover glasses were identically functionalized prior to the device assembly. Since both PDMS and glass attain negative surface charge densities in an aqueous environment, the first layer of polyelectrolyte used was a cationic layer. To assist polycation adsorption on PDMS and the glass surface, both the PDMS mold and cover glasses were air plasma activated (42 s, 80% power, 1.0 mbar). Immediately after that, the PDMS mold and glasses were immersed in a 4 mg/ml solution of

a cationic polyelectrolyte for 9 min. For the cationic polyelectrolyte, branched poly(ethyleneimine) (PEI, 50% w/v in H₂O, Fluka Analytical, Sigma-Aldrich) solution was used due to its high cationic charge density. The branched PEI polymer consists of primary, secondary, and tertiary amine groups. In general, every third group in PEI is an amine with a high affinity towards protonation^{199,221}. After 9 min of incubation in PEI solution, both the PDMS mold and the cover glasses were washed thoroughly with Milli-Q water and dried under a N₂ stream. Adsorption of PEI polyelectrolyte on the PDMS and the glass surfaces was verified through particle trapping experiments using positively charged nanoparticles. Immediately after drying, both the PDMS mold and the cover glasses were immersed in a 4 mg/ml anionic polyelectrolyte solution of poly(sodium 4-styrenesulfonate) (PSS, 30% w/v in H₂O, M_w ~ 70000 Da, Sigma-Aldrich) for 9 min. After polyanion adsorption, both the PDMS mold and the cover glasses were washed thoroughly with Milli-Q water and N₂ dried. Immediately after drying, nanochannels on the functionalized PDMS mold were filled with nanoparticle solution, and the filled PDMS mold was placed on a functionalized glass and pressed gently to achieve PDMS mold and glass binding. To avoid drying of nanochannels, all inlets and outlets were filled with buffer solution, and the other identically functionalized cover glass was placed on top of the PDMS mold to obtain the final device for the experiment, as shown in Figure 4.3. Here, we used deionized (DI) water (18 MΩ/cm⁻¹) in place of buffer solution for particle trapping experiments.

In the functionalization procedure, cleaning after polyelectrolyte adsorption played a crucial role in the multilayer functionalization of PDMS and glass surfaces. Thus, thorough washing was required to wash away nonadsorbed polyelectrolytes and for proper physisorption of the consecutive polyelectrolyte layer. Using the adsorption of polycations and polyanions alternatively, one can achieve multiple layers of polyelectrolytes¹⁹⁴.

4.2.5 Particle Detection and Tracking

Trapped nanoparticles inside a GIE-trapping nanofluidic device were imaged using a home-built interferometric scattering (iSCAT) microscope^{113,123,124}. The detection relies on the interference of the light scattered from the trapped nano-object and light reflected from the interface of the buffer solution and the substrate. The iSCAT setup was used for particle detection and particle motion recording as described in previous works^{85,113,211}. The images were recorded with an exposure time of 1 ms and an acquisition rate of 111 Hz using a 300 mW, 532 nm laser-pumped solid-state laser (MGL-III-532, CNILaser). Recorded images were used to determine the particle center and its displacement in each frame through Gaussian fitting of the particle intensity profile^{111,113}. The obtained two-dimensional x and y coordinates for the particle center were further used to calculate the radial mean square displacement (MSD_r) of the trapped nano-object inside a nanopocket and eventually obtain the stiffness constants¹¹¹, as shown in Figure 4.4. $MSD_r, \langle [\Delta r(\Delta t)^2] \rangle$, where $r = \sqrt{x^2 + y^2}$, was calculated as a function of lag time Δt . The MSD_r value reaches a plateau at large lag times for a trapped particle due to its restricted motion inside a nanopocket. The MSD_r value at the plateau, $[MSD_r]_{plateau} = \langle [\Delta r]_p^2 \rangle$, is directly related to the radial stiffness constant (k_r) of

the electrostatic potential trap inside the nanopockets by $[MSD_r]_{plateau} = 4k_B T/k_r$, where k_B is the Boltzmann constant and T is the absolute room temperature.¹¹⁰

To better understand the electrostatic potential trap, the mean residence time of the trapped particle inside the trap (Kramers time = $\bar{\tau}_k$) and potential depth (Q) of the trap are also required in addition to the stiffness constant. The Kramers time and potential depth of the trap are related as $\bar{\tau}_k \cong \tau_R e^{Q/k_B T}$, where τ_R is the relaxation time in the potential well, which is equivalent to the time an untrapped particle takes to freely diffuse through a distance corresponding to the width of potential well.¹²⁵ Relaxation time values can be calculated using $\tau_R = k_B T/Dk_r$, where the diffusion constant for a particle with diameter d is $D = k_B T/3\pi\eta d$, and η is the dynamic viscosity of the solution.^{110,125,128} When particle trapping measurements are performed under equilibrium conditions with exposure times larger than τ_R , the MSD is a flat plateau with the $MSD_r(\Delta t)$ value reaching $[MSD_r]_{plateau}$, as presented in Figure 4.4. However, for exposure times shorter than τ_R , the $MSD_r(\Delta t)$ value monotonically increases and reaches a plateau.

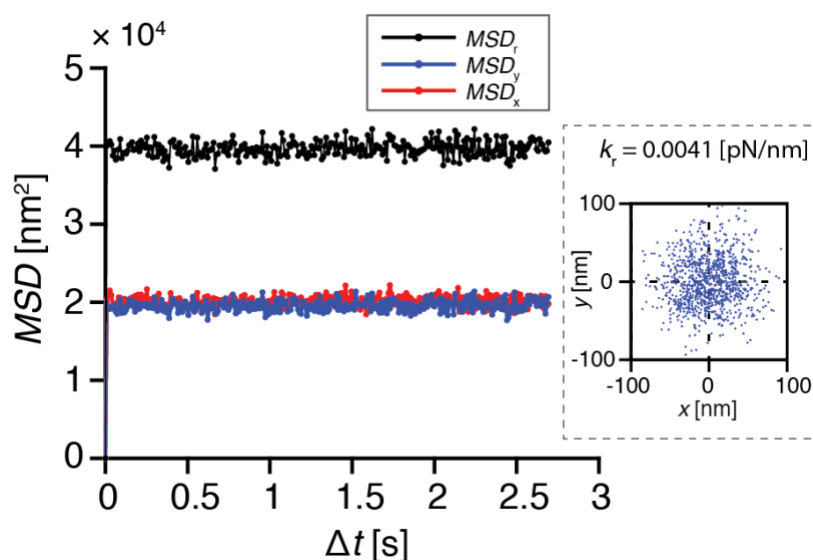


Figure 4.4. Mean square displacement plot as a function of lag time (Δt) of a negatively charged 80 nm diameter particle trapped inside a 500 nm wide nanopocket in a functionalized PDMS device. The x and y coordinates of the particle center inside the potential trap (inset) are used to calculate the MSD_x (red), MSD_y (blue) and MSD_r values. The MSD_r value at the plateau is then used to calculate the stiffness constant of the trapped particle.

4.3 Results

4.3.1 Electrostatic Single Particle Trapping

Single particle confinement experiments were conducted using PDMS-based GIE-trapping nanofluidic devices with and without surface functionalization to analyze the effect of surface modification on the contact-free confinement of a single nano-object. Surface functionalization was carried out using the polyelectrolytes PEI (poly(ethyleneimine))²²²⁻²²⁶ and

PSS (poly-(sodium 4-styrenesulfonate)), as presented in Section 4.2.4. For experiments, a particle sample solution was prepared as described in Section 4.2.2 using negatively charged 80 nm diameter gold nanoparticles in DI water in place of buffer solution. The obtained salt concentration of the final particle solutions was in the range of $\sim 0.02 - 0.05$ mM. Particle samples were always prepared freshly on the day of the experiment to avoid particle agglomeration.

PDMS fluidic devices with and without surface functionalization were obtained using a PDMS mold and cover glass, as described in Sections 4.2.4 and 4.2.3, respectively. For functionalization, two layers – the first a cationic layer (PEI) and second anionic polyelectrolyte layer (PSS) - were adsorbed on the PDMS mold and the cover glass surface. The two-layer (PEI and PSS) functionalization of the PDMS and glass surface resulted in a net negative surface charge density of the substrates.

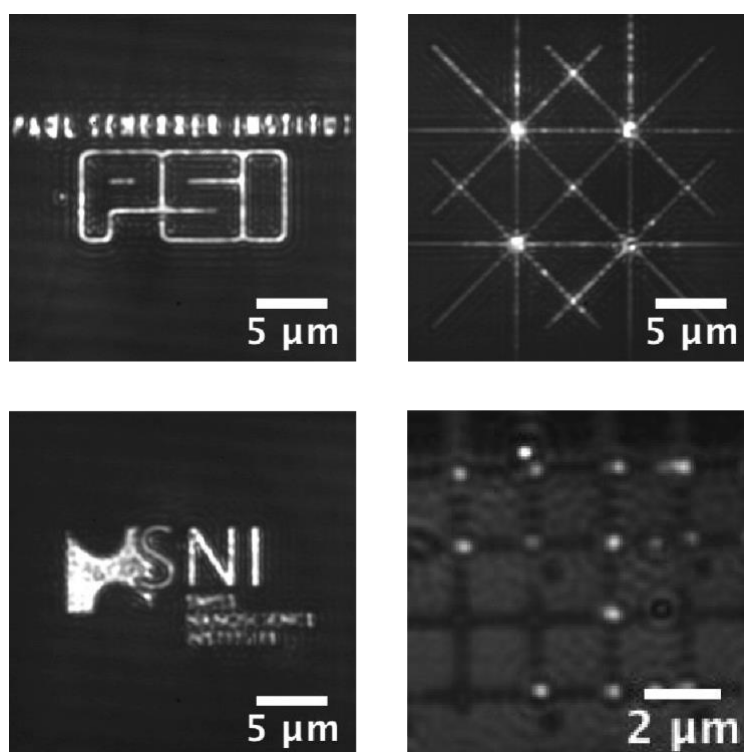


Figure 4.5 Nanoparticle trapping in various nano- and microstructures embedded in nanochannels. The depths of nano/microindentations are 80 nm in the case of the Unibasel, PSI and SNI logos and 100 nm in the case of the grid; the channel height is 160 nm.

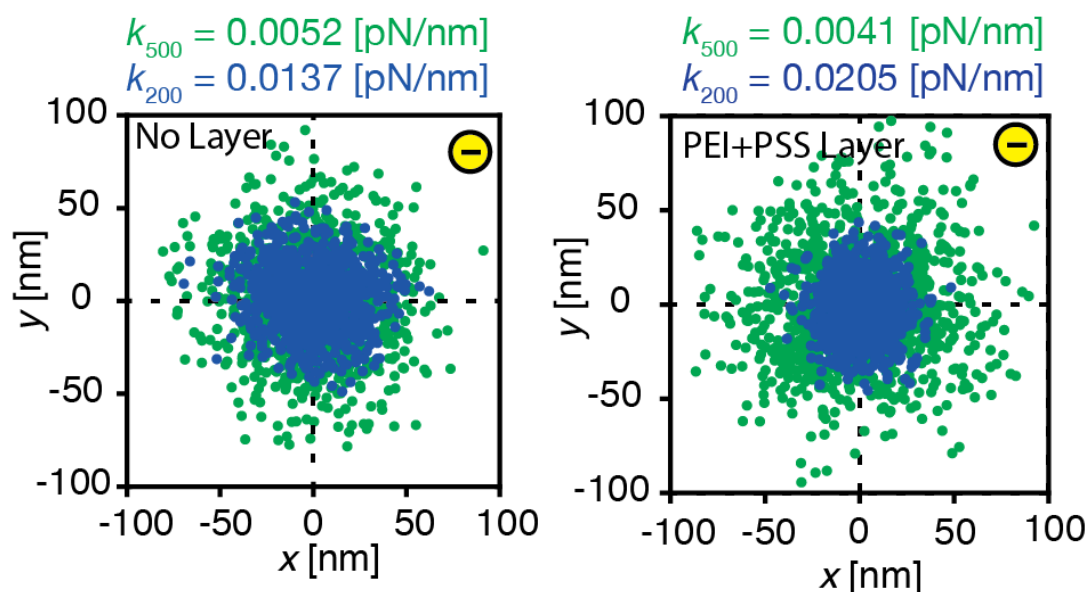


Figure 4.6 Scatter plots of negatively charged single 80 nm gold nanoparticles confined in a contact-free manner in 200 nm (blue) and 500 nm (green) diameter pockets inside a native device (left) and the polyethyleneimine and poly(sodium 4-styrenesulfonate)-functionalized (right) PDMS device. The spread of the scatter plots of the trapped particles in the 500 nm and 200 nm pockets shows lower trapping strength of the potential trap for 500 nm nanopockets than for 200 nm pockets. The calculated stiffness constants (k) for the functionalized and native device were comparable for both the 200 nm and 500 nm nanopockets, denoting the homogeneous surface functionalization of the device.

For particle confinement, various geometries of nanostructures can be used, as shown in Figure 4.5, enabling single particle to multiparticle trapping depending on the size and geometry of the nanoindentations. These nanoindentations can be modified according to the requirements of the experiments and the types of objects that need to be trapped. In our quantitative study, experimental trapping data were collected for circular nanoindentations with diameters of (i) 200 nm and (ii) 500 nm and a depth of 100 nm, as shown in Figure 4.2. To collect particle dynamics information for the trapped particles, images of the trapped nano-objects were collected using the interferometric scattering (iSCAT) detection method. Collected images were further processed to calculate the trapping stiffness of the potential trap as described in Section 4.2.5. Scatter plots of the trapped single nanoparticles were obtained using the x and y coordinates of the center of the confined particle, as shown in Figure 4.6. Using the particle trajectory inside the potential trap, the radial mean square displacement (MSD_r) of the particle was calculated, which reaches a plateau for a confined particle¹²⁷. As mentioned in Section 4.2.5, the MSD_r value at the plateau is related to the radial trapping stiffness constant as $[MSD_r]_{plateau} = 4k_B T/k_r$ ^{110,125}, thus giving quantitative information about the strength of the potential trap.

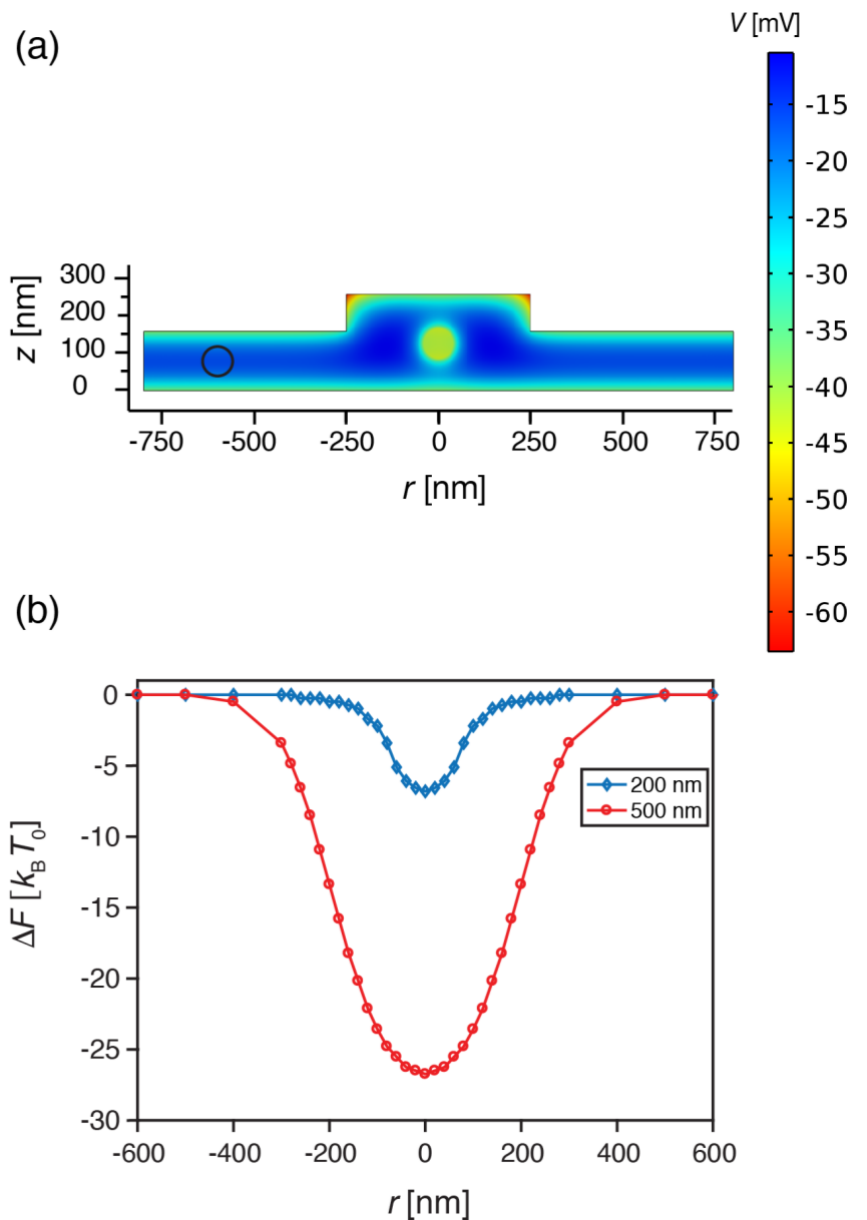


Figure 4.7 (a) 2D electrostatic potential distribution along the yz -plane at $x = 0$ for channel height = 160 nm, pocket depth = 100 nm, pocket diameter = 500 nm, salt concentration = 0.03 mM, and particle diameter = 80 nm. 3D COMSOL simulations were performed for different particle locations inside and outside of the pocket ranging from $r = 0$ nm (bright circle) to $r = 600$ nm (black circle). A potential distribution was used for the calculation of the system free energy as a function of the particle position relative to the center of the nanotrap (i.e., $r = 0$). (b) Helmholtz free energy distribution with respect to the radial position (r) of the trapped nanoparticles inside nanopockets with 200 nm (blue curve) and 500 nm (red curve) diameters. The difference in the free energy of the system was calculated with respect to the Helmholtz energy of the system with the particle at $r = 600$ nm.

In experiments, the measured radial stiffness constants of trapped nanoparticles were comparable for native and surface-modified fluidic device, denoting a homogeneous surface

charge density of the functionalized device surface, which was equivalent to the surface charge density of the native device. Furthermore, we observed that nanoparticles had stronger trapping in 200 nm circular pockets than in 500 nm pockets, as shown in Figure 4.6, where the radial stiffness constant of negatively charged 80 nm diameter particles was higher for a 200 nm pocket than for a 500 nm pocket. This is due to the broadening of the potential well in the case of the 500 nm pocket¹⁰⁹. To further explain the impact of the pocket diameter, we conducted COMSOL simulations for a GIE trap with a negatively charged 80 nm diameter particle at different radial locations inside the trap and nanochannel, as shown in Figure 4.7. In the simulations, the Helmholtz free energy (F) of the entire system^{109,227,228} was calculated for different radial locations of the nanoparticle using the self-energy of the system including the particle (U) and the entropy of the system (ΔS): $F = U - T\Delta S$, where T is the system temperature in Kelvin.

The self-energy of the system was calculated using the electrostatic potential (ψ) inside the GIE trap:

$$U = \frac{1}{2} \varepsilon_r \varepsilon_0 \int_V (\nabla\psi)^2 dV = \frac{1}{2} \int_A \sigma\psi_0 dA + \frac{1}{2} \int_V \rho\psi dV$$

and ΔS was calculated for monovalent-containing binary solutions such as NaCl using:

$$\Delta S = k_B \int_V \left\{ c_\infty \left[\left(1 + \frac{e\psi}{k_B T} \right) e^{-\frac{e\psi}{k_B T}} + \left(1 - \frac{e\psi}{k_B T} \right) e^{\frac{e\psi}{k_B T}} - 2 \right] \right\} dV$$

The potential distribution inside the GIE trap was calculated using the Poisson Boltzmann (PB) equation:

$$\nabla \cdot (\varepsilon E) = \rho_v$$

where $E = -\nabla\psi$ and ε is the permittivity of the solution at zero frequency. The total free charge density is $(\rho_v) = -2c^\infty e \sinh\left(\frac{e\psi}{k_B T}\right)$, where k_B is the Boltzmann constant. These simulations were solved using the electrostatics model in COMSOL, which was validated against previously published work^{109,212}.

To compare the simulations with real experiments, simulations were performed with the nanoparticle situated at the location of minimum potential energy along the z -direction at different radial positions. The location of minimum potential energy along the z -axis for different radial locations was calculated prior to charged-particle-inclusive simulations by using COMSOL simulations performed with a point charge approximation of the charged particle²²⁸. For COMSOL simulations (COMSOL Multiphysics package 4.2), the Poisson-Boltzmann equation was solved in 3D space using the surface charge density of PDMS and glass $-3 \times 10^{-3} e/nm^2$, in agreement with the literature^{115,125}, and the ionic strength of monovalent salt solution, 0.03 mM based on zeta potential measurements. The particle surface charge used in the simulations for the 80 nm diameter nanoparticle was $-132 e$ based on the zeta potential measurement.

The device geometry used for simulations was similar to that of the real device with a 160 nm channel height, a 100 nm pocket depth, and pocket diameters of 200 nm and 500 nm, as shown in Figure 4.7. The nanopockets were kept cylindrical with rotational symmetry along the $r = 0$ axis. 3D COMSOL simulations were performed for different particle locations inside and outside of the pocket ranging from $r = 0$ nm to $r = 600$ nm. In the lateral direction, the particle was located at the position of minimum potential energy at a fixed radial position. The z -locations for the minimum potential energy were calculated using 4×4 nm² averaging of the potential distribution obtained from the point charge approximation COMSOL simulations. The simulated potential distribution for each particle location was further used to calculate the Helmholtz free energy (F) of the system under individual particle configurations by calculating the self-energy of the system and entropy of the system^{109,212}. Employing the Helmholtz energy difference as a function of r , the trapping stiffness constant was calculated by $\Delta F = 1/2 k_r r^2$ (ref. ²¹²). The stiffness constants obtained using simulated results were 0.0043 [pN/nm] for 200 nm diameter pockets and 0.0027 [pN/nm] for 500 nm pockets, which match the stiffness constants measured during experiments for stable particle trapping.

As shown in Figure 4.7, broadening of the pocket diameter from 200 nm to 500 nm makes the potential trap wider and deeper. A deeper potential well allows higher residence times for trapped particles, but contrary to this, broadening of the potential well reduces the stiffness constant of the trap. A broad potential well provides the trapped particle with more room for diffusion and thus results in a lower stiffness constant. However, when comparing increments in pocket diameter from 0 to 500 nm, the stiffness constant for an 80 nm particle initially increases until ≈ 250 nm and then decreases²²⁸.

4.3.2 Single to multiparticle trapping

We conducted experiments for contact-free trapping of negatively charged 80 nm Au NPs using PDMS-based GIE-trapping devices. We observed that particle trapping, including the stiffness constant and residence time, is strongly influenced by the binding of PDMS with the glass surface. In the case of perfect PDMS-glass binding, we observed stable single particle trapping. In electrostatic trapping, the number of particles confined inside a nanopocket depends on the hydrodynamic radius of the particle and the diameter and depth of the nanopocket. For 80 nm diameter nanoparticles, along with single particle trapping, we observed frequent multiparticle trapping for 500 nm pockets and relatively low double or multioccupancy in 200 nm pockets, as shown in Figure 4.8. Single and multiparticle occupancy in the nanopockets can be identified based on the intensity profile of collected images, as demonstrated in Figure 4.8. Since the images were collected using the iSCAT method, larger particles scatter more light and thus appear brighter in the collected image. The scattering intensity is proportional to the size of the particle; thus, a multiparticle assembly gives a higher intensity than a single nanoparticle. To achieve single particle trapping throughout the GIE-trapping PDMS-based device, it is important to optimize the pocket diameter according

to the hydrodynamic radius of the particle of interest inside the buffer solution that will be used for the particle trapping experiment.

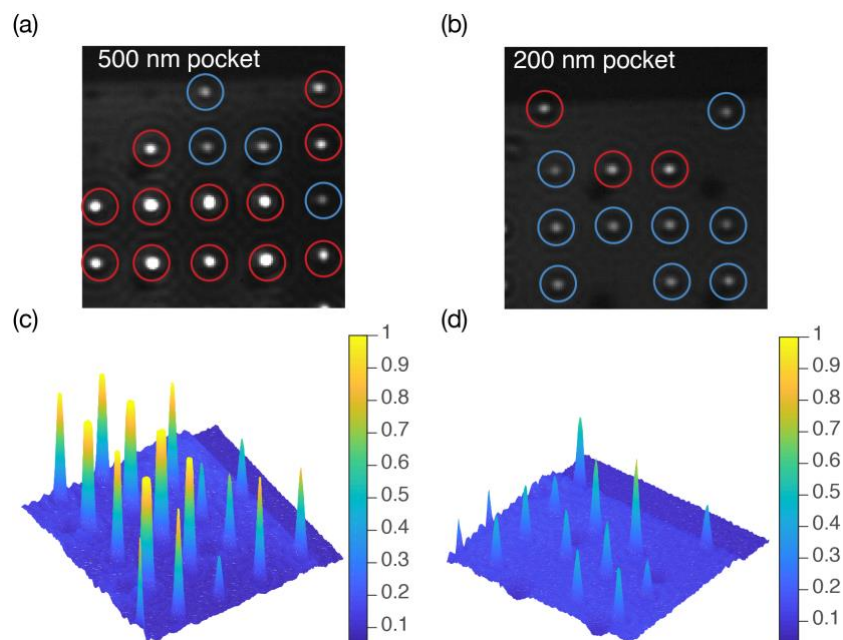


Figure 4.8 Negatively charged single 80 nm diameter gold nanoparticles trapped in multiple (a) 500 nm and (b) 200 nm pockets (blue circle). Double and multioccupancy of nanoparticles was also observed (red circle) more frequently in the case of (a) 500 nm pockets than (b) 200 nm pockets. Multi-occupancy was also detectable from the intensity profile of trapped nano-objects inside the nanopockets of (c) 500 nm and (d) 200 nm diameter, where the intensity was normalized with the maximum RGB value (255).

4.3.3 Experimental comparison for functionalized and nonfunctionalized devices

The final particle trapping depends on the surface charge density of the device surface along with the geometrical parameters of the device; therefore, the trapping stiffness constant for trapped particles in a functionalized PDMS-based device indirectly provides information on how homogeneous and quantitatively similar the surface charge density is for a surface-modified device with respect to the native device. For successful contact-free nanoparticle trapping, the device surface must be homogeneously functionalized. In the presence of an inhomogeneous functionalized surface, charged particles become stuck to the surface and do not show electrostatic trapping.

Experimental data for conventional and two-layer polyelectrolyte (PEI and PSS)-functionalized PDMS devices were compared based on the observed trapping stiffness constants of confined single nanoparticles. The stiffness constant of a trapped object denotes the strength of confinement and the scope to which a particle moves inside the electrostatic trap.

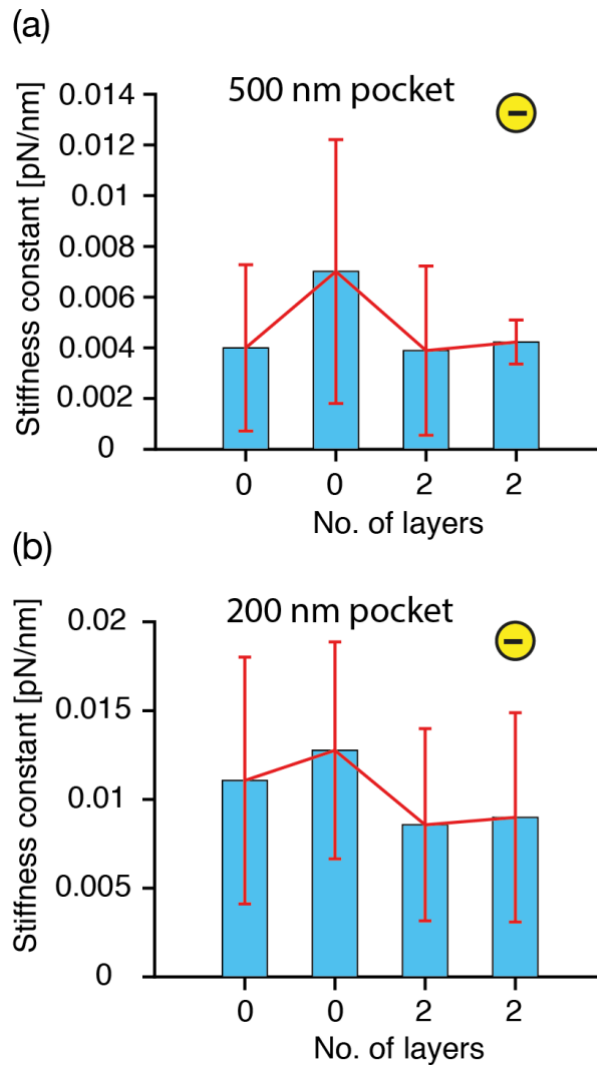


Figure 4.9 Comparison of the trapping stiffness constant obtained for negatively charged single 80 nm gold nanoparticles trapped in (a) 500 nm and (b) 200 nm pockets for both two-layer polyelectrolyte functionalized and nonfunctionalized (0-layer polyelectrolyte) PDMS devices with a 160 nm channel depth and a 100 nm pocket depth. Two datasets were collected from two different experiments to show the distribution variation of the single nanoparticle trapping stiffness constant between different experiments.

We compared experimental data for 500 nm and 200 nm diameter nanopockets. As shown in Figure 4.9, a single trapped particle in 500 nm pockets had a larger spread of the stiffness constant due to higher freedom of movement inside the potential trap, which can be understood from the simulation results shown in Section 4.3.1. Experimentally, we observed that for 500 nm pockets, loosely trapped 80 nm single particles moved within a 200 nm distance from the pocket center and had a stiffness constant in the range of $\sim 0.0004 - 0.0006$ [pN/nm], whereas particles trapped stably inside the pocket diffused in the range of 150 nm, 130 nm, and 100 nm from the center of the pocket and had k_r in the range of $\sim 0.0008 - 0.002$ [pN/nm], $\sim 0.002 - 0.003$ [pN/nm], and $\sim 0.002 -$

0.004 [pN/nm], respectively. For strongly trapped nanoparticles with diffusion in the range of ≤ 75 nm around the pocket center, k_r was $\sim 0.005 - 0.022$ [pN/nm]. Similarly, for 200 nm pockets, 80 nm gold nanoparticles loosely trapped in 200 nm pockets were confined in the range of 100 nm and showed a stiffness constant in the range of $\sim 0.003 - 0.006$ [pN/nm]. For stable trapping, particles diffused over distances of ≤ 70 nm and ≥ 50 nm around the pocket center, with $k_r \sim 0.004 - 0.01$ [pN/nm], and for strong confinement, particle diffusion was in the range of < 70 nm and ≥ 30 nm with $k_r \sim 0.01 - 0.03$ [pN/nm]. This observation was valid for both two-layer functionalized and nonfunctionalized PDMS devices.

During particle trapping, the particle confinement inside the potential well varies depending on the hydrodynamic diameter and net surface charge of the particle²²⁸ along with the slight variations (in the nanometer range) in the geometry of the potential trap, leading to a distribution of the trapping stiffness constant, as shown in Figure 4.9. The nanoparticles used for experiments had a coefficient of variation (CV) for the diameter of nearly 8% and showed a distribution of the net particle surface charge during zeta potential measurements (CV $\sim 11\%$), leading to a distribution of the experimental data.

When geometrical optimization is required to attain stronger particle trapping, it is important to understand the possible causes of the distribution of the stiffness constant, which are mainly related to physical phenomena and experimental conditions. When a particle reaches the inside of a potential trap, it goes through a momentum relaxation process related to its ballistic motion. This momentum relaxation time (τ_p) related to ballistic motion can be in the range of a few picoseconds to a few nanoseconds. In our case, τ_p is ~ 8 ns. The ballistic motion of the charged particle occurs primarily before the particle is trapped inside the potential well. Once the charged particle is trapped, it undergoes an oscillatory motion in the harmonic well of the potential trap, which is mainly governed by diffusion instead of the particle inertia.¹¹¹ The relaxation time (τ_R) of the charged particle inside the potential well is related to the viscous drag from the fluid in the device. In our case, the relaxation time (τ_R) of an 80 nm diameter Au NP inside a 200 nm diameter pocket is ~ 0.15 ms, and inside a 500 nm diameter pocket is ~ 0.25 ms. The sampling rate (~ 9 ms) and integration time (1 ms) of the detection camera in our experiments are much slower than the above two relaxation times. This implies that the experimental measurements are not able to resolve the momentum relaxation dynamics of the particle and that particle motion is captured under equilibrium conditions. Since the exposure time (1 ms) is larger than the momentum relaxation time of the particle inside the potential trap, the spatial averaging of the particle motion over the larger integration time causes a motion blur, leading to a larger measured stiffness constant than the actual stiffness constant of the particle.^{197,229,230} Therefore, the particle trapping looks relatively stiff compared to its true trapping stiffness. The combination of all these factors leads to a distribution of the measured stiffness constant.

The range of obtained stiffness constants for single particle trapping in both 500 nm and 200 nm pockets for functionalized and nonfunctionalized PDMS devices, as shown in Figure 4.9, demonstrates comparable particle trapping inside the PDMS device before and

after functionalization. It was noted that in the case of unsuccessful two-layer functionalization, charged particles became stuck on the glass and PDMS surfaces due to electrostatic attraction forces. Only in the case of obtained homogeneous surface functionalization was the performance of the devices maintained.

4.4 Discussions

The presented experimental and simulation results confirm that geometry-induced electrostatic trapping for nanoparticles depends on the trap dimensions, such as the trap diameter for a constant channel height and a fixed salt concentration of the solution used. It has furthermore been demonstrated that confinement of nano-objects inside nanoindentations can be measured in terms of the radial stiffness constant (k_r), which can be used to identify how strongly a particle is trapped inside the electrostatic potential trap. However, particle trapping can vary based on the size and net surface charge of the particle and the depth and width of the electrostatic trap inside the nanopockets. Therefore, it is important to optimize the device geometry based on the experimental requirements to attain stable high-throughput particle trapping.

In this work, we demonstrated successful electrostatic contact-free trapping for charged single nanoparticles in a multilayer polyelectrolyte-functionalized PDMS-based nanofluidic device. The two-layer functionalized devices demonstrated trapping efficiency comparable to that of the nonfunctionalized device and numerical calculations, indicating that the overall achieved surface charge density is quantitatively similar to that of the native PDMS surface and homogeneous enough to allow contact-free trapping of 80 nm diameter particles. This further demonstrated that the functionalization procedure can be used for single-layer polyelectrolyte functionalization to achieve a positively charged device surface for trapping of positively charged nanoparticles without affecting the device functionality. This broadens the scope of the electrostatic trapping method to positively charged nano-objects using functionalized PDMS-based nanofluidic devices.

The presented surface modification method for PDMS-based nanofluidic devices has not only improved the surface modification process for nanofluidic devices but also reduced the surface functionalization time by nearly 10 times. The use of PDMS-based GIE-trapping nanofluidic devices in combination with the presented surface-modification method has allowed the large-scale production of surface-modified nanofluidic devices. This furthermore has opened up new possibilities to trap both positively and negatively charged particles in the same device at different trapping locations by selectively functionalizing the trapping areas for net positive and negative surface charge density, respectively. This would be of immense use in the fields of medicine, disease diagnosis, biological studies, pathogen detection, and water quality checks.

Acknowledgements

The work was funded by the Swiss Nanoscience Institute, Basel, Switzerland (SNI PhD Graduate School) under the project P1310. We would like to thank Dr. Michael A. Gerspach for fruitful discussions and Konrad Vogelsang for technical support.

Conflict of Interests

The authors declare no conflict of interest.

Contributions

D.S. performed the experiments and simulations, analyzed the data, and wrote the manuscript. Y.E., T.P. and R.Y.H.L. supervised the project.

Chapter 5. Optimization of Nanofluidic Devices for Geometry-Induced Electrostatic Trapping

Deepika Sharma ^{1, 2, *}, Roderick Y. H. Lim ¹, Thomas Pfohl ³, Yasin Ekinci ^{2, *}

¹ Biozentrum, University of Basel, 4056, Basel, Switzerland

² Laboratory for Micro and Nanotechnology, Paul Scherrer Institute, 5232, Villigen, Switzerland

³ Institute of Physics, University of Freiburg, D-79104, Freiburg, Germany

*corresponding authors: deepika.sharma@unibas.ch, yasin.ekinci@psi.ch

ABSTRACT

Nanoparticle trapping in a nanofluidic device utilizing geometry-induced electrostatic (GIE) potential trap is an efficient and robust way to perform nano-object confinement and single particle studies. The GIE trapping is a passive method that solely depends on the device geometry and device-particle surface interaction. Therefore, optimization of a nanofluidic device, based on experimental requirements, helps to achieve stiffer single-particle trapping. The efficiency of a GIE-trapping device is defined in terms of residence time and trapping stiffness of the nanoparticle inside a potential trap. The present study reveals all crucial parameters that affect the device efficiency, particle trapping stiffness, and particle residence time. Furthermore, the trends of particle trapping stiffness are presented as a function of crucial parameters and demonstrate two variants of simulations to estimate the particle trapping efficiency: (a) using a charged particle and (b) using point charge approximation. Simulations with charged particle give more realistic values related to particle trapping whereas simulations with point charge approximation is a faster approach which gives approximate values and a guideline for more rigorous simulations. The results demonstrate a good agreement with experimental observations and hold the key for future developments in this field, wherein a device geometry can be very precisely optimized.

KEYWORDS: Finite element analysis, electrostatic trapping, simulations, nanofluidics, thermodynamics

5.1 Introduction

The geometry-induced electrostatic (GIE) trapping method is a robust passive way to confine nanoparticles in a contact-free manner inside nanofluidic devices. There have been extensive studies on electrostatic trapping of various nanoparticles such as gold nanoparticles^{85,113,211}, lipid vesicles, DNA, and nanorods^{94,112}. Recently published work denotes the development in nanofluidic GIE-trapping devices and in the scope of applications of the method.^{94,188,212} For GIE trapping, nanofluidic devices are fabricated consisting of nanochannels that are embedded with nanometric indentations, also called nanopockets, to confine nano-objects inside these nanoindentations. A charged nano-object gets confined in a potential well formed at the location of the nanopocket due to electrostatic repulsive forces from the substrate walls of the nano-pocket and nanochannel.⁸⁵ Conventionally, silicon, glass, and PDMS substrates are used for electrostatic particle confinement, since all these substrates acquire net negative surface charge densities in contact with an aqueous solution (pH > 2) due to self-deprotonation of terminal silanol groups.^{85,112,118,119} Negative surface charge density of the substrate results in the redistribution of ions inside the buffer solution, which leads to the formation of an electric double layer (EDL)^{114,231}.

As per the Stern representation of EDL, electrostatic potential decays linearly in the Stern layer near the substrate surface, and exponentially in the diffuse layer beyond the Stern layer, as shown in Figure 5.1(a). The potential at the interface of the Stern layer and the diffuse layer is known as the zeta potential (ζ) which can be measured using electrophoresis for particulates.^{232,233} To simplify the electrostatic potential distribution away from the charged surface, the diffuse layer is considered to be in direct contact with the charged surface, which is also known as the Gouy-Chapman (GC) representation of EDL, as shown in Figure 5.1(b). The electrostatic potential distribution in the diffuse layer, normal to the charged surface in an aqueous solution, can be expressed by the Poisson-Boltzmann (PB) equation, where the buffer solution is considered to be diluted so that ions do not interact with each other, charges in the solution are supposed to be point-like, and the dielectric coefficient of the buffer solution is considered uniform in the EDL¹⁸⁹:

$$\nabla \cdot (-\varepsilon \nabla \psi) = -\varepsilon \nabla^2 \psi = \sum_i z_i e c_i^\infty e^{-\frac{z_i e \psi}{k_B T}} \quad (5.1)$$

here z_i (sign included) and $c_i^\infty = n_i c^\infty$ are the charge number and bulk concentration of i^{th} ion, respectively, n_i is the number of i^{th} ion in the formula of buffer solution, c^∞ is the bulk concentration (ion/m³) of the buffer solution, ψ is the position dependent electrostatic potential, k_B is the Boltzmann constant, T is temperature in Kelvin, and ε is the permittivity of the solution at zero frequency. In the case of water $\varepsilon_r = 80 \varepsilon_0$, where ε_0 is the permittivity of free space.¹⁸⁹

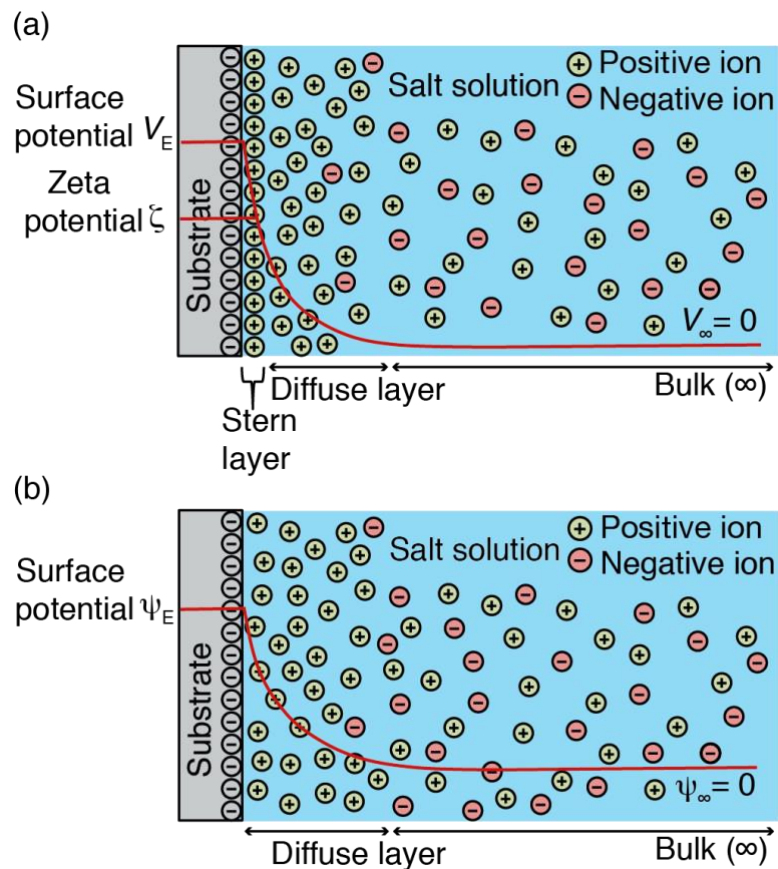


Figure 5.1. (a) The Stern and (b) GC representation of electric double layer. In the Stern representation, the EDL is composed of the Stern layer and the diffuse layer, whereas in the GC representation, the diffuse layer is in direct contact with the charged surface.

It has been previously shown that electrostatic trapping in GIE-trapping devices depends on several geometrical parameters that directly influence the trapping stiffness and residence time of the confined particle.^{84,85,109,110,125} Thus, it is important to acquire prior knowledge of how different geometrical parameters affect the trapping stiffness and residence time of a trapped nanoparticle. To get a complete overview of the trapping strength dependency on geometrical parameters of a nanofluidic device, we have studied all crucial parameters such as nanopocket diameter and its height, nanochannel height, and salt concentration of the buffer solution considering surface charge densities of the trapped particle and nanochannel walls remain constant during the experiment.

To perform parametric studies, we simulated a GIE-trapping device geometry comprising of one nanochannel and one nanopocket, where the electrostatic potential distribution of the system was numerically calculated inside and outside of the nanopockets by solving the nonlinear PB equation (Electrostatic module in COMSOL Multiphysics 4.2). The analysis will help to understand the impact of different parameters on the final single particle trapping,

and also to identify the parametric values for the optimization of a GIE-trapping device as per the requirements of an experiment.

5.2 Theory

In the case of a binary symmetric electrolyte ($z_+ = |z_-| = z$ and $c_+^\infty = c_-^\infty = c^\infty$), Equation 5.1 can be written in the form of the GC equation:

$$\nabla \cdot (-\varepsilon \nabla \psi) = -z e c^\infty \left(e^{\frac{ze\psi}{k_B T}} - e^{-\frac{ze\psi}{k_B T}} \right) \quad (5.2)$$

$$\nabla \cdot (-\varepsilon \nabla \psi) = -2z e c^\infty \sinh \left(\frac{ze\psi}{k_B T} \right) \quad (5.3)$$

In the case of a low electrolyte energy system where the electrostatic energy of ions is smaller than the thermal energy, that is, ($|\psi| \ll |\psi_T| = \frac{k_B T}{ze}$), the GC equation can be linearized to:

$$\nabla \cdot (-\varepsilon \nabla \psi) = -2z e c^\infty \left(\frac{ze\psi}{k_B T} \right) \quad (5.4)$$

For a planar geometry, an infinitely extended planar surface, potential $\psi(x, y, z)$ is independent of two axes parameters parallel to the plane and depends only on the axis parameter perpendicular to the plane. Thus, GC equation is modified to:

$$\frac{d^2 \psi}{dz^2} = -\frac{2z^2 e^2 c^\infty \psi}{\varepsilon k_B T} \quad (5.5)$$

Analytical solution to the equation is:

$$\psi(z) = \psi_0 e^{-\frac{z}{k^{-1}}} \quad (5.6)$$

The electrostatic potential decays exponentially from the surface perpendicular to the surface. The characteristic length k^{-1} of the decay is known as the Debye length.

$$k^{-1} = \sqrt{\frac{\varepsilon k_B T}{2z^2 e^2 c^\infty}} \quad (5.7)$$

The Debye length for a monovalent electrolyte solution in water at room temperature is:

$$k^{-1} = \frac{3.06 \text{ \AA}}{\sqrt{c_0 \left(\frac{\text{mol}}{\text{L}}\right)}} \quad (5.8)$$

Equations 5.6 and 5.8 are helpful to roughly estimate particle stiffness constants, particle residence times, and Debye length for a GIE-trapping device. However, for precise nanoparticle trapping calculations where all device geometries are in the range of the Debye length, numerical simulations are required and Equation 5.3 needs to be solved without the assumption of $(|\psi| \ll |\psi_T| = \frac{k_B T}{ze})$.

5.3 Parametric study of GIE trapping

For a detailed study of the impact of different geometric parameters of the GIE-trapping device on a particle trapping and its residence time, we have first simulated a simplified system with a particle replaced by a point charge with an equivalent net charge. The residence time of a trapped particle is defined as the average time a particle stays inside a GIE potential trap before escaping. The point charge approximation allows for a faster analysis of the trapping stiffness profile with respect to several parameters such as pocket height (H_P), pocket diameter (D_P), channel height (H_C), and salt concentration (C_0) of the buffer solution. Simulations with point charges help to quickly attain approximate values of particle trapping and a guideline for more rigorous simulations. The simplified studies using the point charge approximation is then followed by the more realistic simulations that take into account the particle size and the particle surface charge.

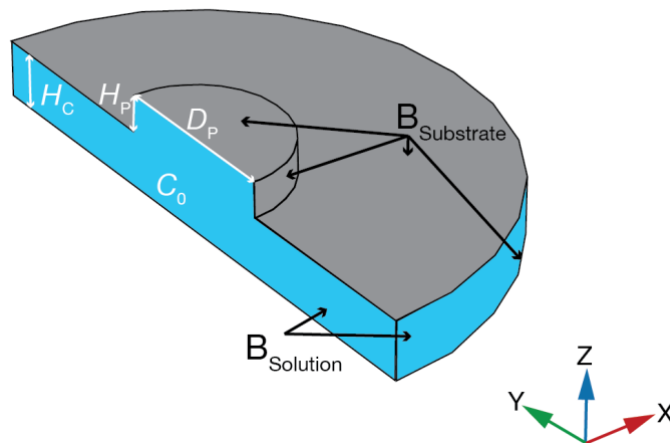


Figure 5.2. Geometrical model of the simulation domain in a GIE-trapping region, used for electrostatic simulations. The model comprises of one nanochannel with height H_C filled with salt solution of concentration C_0 , and one cylindrical nanopocket of height H_P and diameter D_P . Buffer solution (blue) is between substrate boundaries denoted by $B_{\text{Substrate}}$, and solution boundaries denoted by B_{Solution} .

A 3D geometry of a nanopocket embedded in a nanochannel was simulated using an electrostatic module in COMSOL Multiphysics 4.2 for electrostatic potential distribution

inside the GIE-trapping region, as shown in Figure 5.2 and Figure 5.3. In our case, the buffer solution was a monovalent low concentration salt solution, thus the linearized GC equation can be used to solve the PB equation inside the nanochannel and nanopocket region.

$$\nabla \cdot (\varepsilon E) = \rho_v \quad (5.9)$$

$$E = -\nabla\psi; D = \varepsilon E \quad (5.10)$$

Here total free charge density:

$$\rho_v = -2c^\infty e \sinh\left(\frac{e\psi}{k_B T}\right)$$

To denote the continuity of the field inside the trapping region at the solution boundaries (B_{Solution}), continuity boundary condition $\hat{n} \cdot D = 0$ was applied. The initial value of potential was considered to be zero in the entire region. To define the discontinuity of the field at the glass surface boundary, $\hat{n} \cdot (D_1 - D_2) = \rho_s$ boundary conditions were applied at the geometry walls ($B_{\text{Substrate}}$). The surface charge density at the glass surface of $\rho_s = -3 \times 10^{-3} \text{ e/nm}^2$ was taken from literature¹¹⁵.

According to the second law of thermodynamics, an isolated macroscopic system in equilibrium attains minimum free energy, that is, Helmholtz energy (F) for an incompressible system as in the case of GIE trapping. The Helmholtz free energy of the whole system is the sum of self-energy of the system (U), that is, electrostatic potential energy of charges in the solution and the particle, and the negative of entropy of the system (S), that is, entropy of mixing of the dilute solution, times the system temperature (T)^{109,234} : $F = U - TS$. To accommodate this equation for our electrostatic trap, S was replaced by ΔS , where ΔS is the entropy difference between the ion distribution in the electrostatic double layer and the same in the solution at $\psi = 0$, at the approximation of dilute electrolyte solution.

Self-energy of the system is thus given by:

$$U = \frac{1}{2} \varepsilon_r \varepsilon_0 \int_V (\nabla\psi)^2 dV = \frac{1}{2} \int_A \sigma\psi_0 dA + \frac{1}{2} \int_V \rho\psi dV \quad (5.11)$$

where σ is the surface charge density at the boundaries of the integral domains and ρ is the volume net charge density in the solution.

ΔS for monovalent containing binary symmetric solution (like NaCl) is ^{234,235}:

$$\Delta S = k_B \int_V \left\{ c^\infty \left[\left(1 + \frac{e\psi}{k_B T}\right) e^{-\frac{e\psi}{k_B T}} + \left(1 - \frac{e\psi}{k_B T}\right) e^{\frac{e\psi}{k_B T}} - 2 \right] \right\} dV \quad (5.12)$$

For constant system temperature, change in Helmholtz free energy of the system is:

$$\Delta F = \Delta U - T\Delta S \quad (5.13)$$

In case of the point charge approximation, contributions of a point charge to both self-energy and entropy of the system are negligible. Thus, the change in the entropy of the system ΔS between the particle location inside and outside a nano-trap is zero. This leads to the equation:

$$\Delta F = \Delta U \quad (5.14)$$

For a harmonic potential trap, trap characteristics can be quantified using the system's Helmholtz free energy²¹²:

$$\Delta F = \frac{1}{2}k_r r^2 \quad (5.15)$$

where k_r is the radial trap stiffness for a harmonic potential trap, and r is the distance from the center of the potential trap.

According to the equipartition theorem, the average energy of a particle at thermal equilibrium is $k_B T/2$ per degree of freedom. Similarly, the probability energy distribution of a particle in a system at thermal equilibrium can be predicted by the Maxwell-Boltzmann distribution, where the instantaneous energy of the particle can be considerably higher than the average energy of the particle. To trap a particle stably at a specific location during these exceedingly high energy states and corresponding velocities, a potential energy trap of nearly $10k_B T$ depth is required.^{120,121,125} The potential depth (Q) of the electrostatic trap also signifies the mean residence time (Kramers time, $\bar{\tau}_k$) of the particle inside the trap, which is related by $\bar{\tau}_k \cong \tau_R e^{Q/k_B T}$, here τ_R is the relaxation time of the particle inside the potential well.^{110,125}

5.3.1 Point-Charge Approximation Simulation Results

Simulations were performed using a reference GIE-trapping geometry with $H_C = 160$ nm, $H_P = 100$ nm, $D_P = 200$ nm, and $C_0 = 0.03$ mM. For the point charge approximation, simulations were performed without a nanoparticle inside the nanochannel, as shown in Figure 5.3. For parametric studies, one parameter was changed while keeping the remaining parameters fixed. Using the potential well profile in the form of the system free energy for the simulated geometry, the stiffness constant for the trapping of a point charge with equivalent net charge as that of a negatively charged 80 nm diameter negatively charged particle, that is, $q = -132e$, ($e = 1.60 \times 10^{-19}$ C) was calculated. Due to the point charge approximation, changes in electrostatic free energy of the system are equivalent to $\Delta U = q\Delta\psi$, as described in Section 5.2. Therefore, simulated potential distributions were used to calculate the potential well profiles (Figure 5.4). To extract the system free energy profiles for potential traps, free energies were calculated for various particle locations along the radial direction (r) and the corresponding location of minimum potential energy for the particle in z -direction. Obtained

potential distribution profiles were further used to calculate the stiffness constants by $\Delta U = 1/2 k_r r^2$.

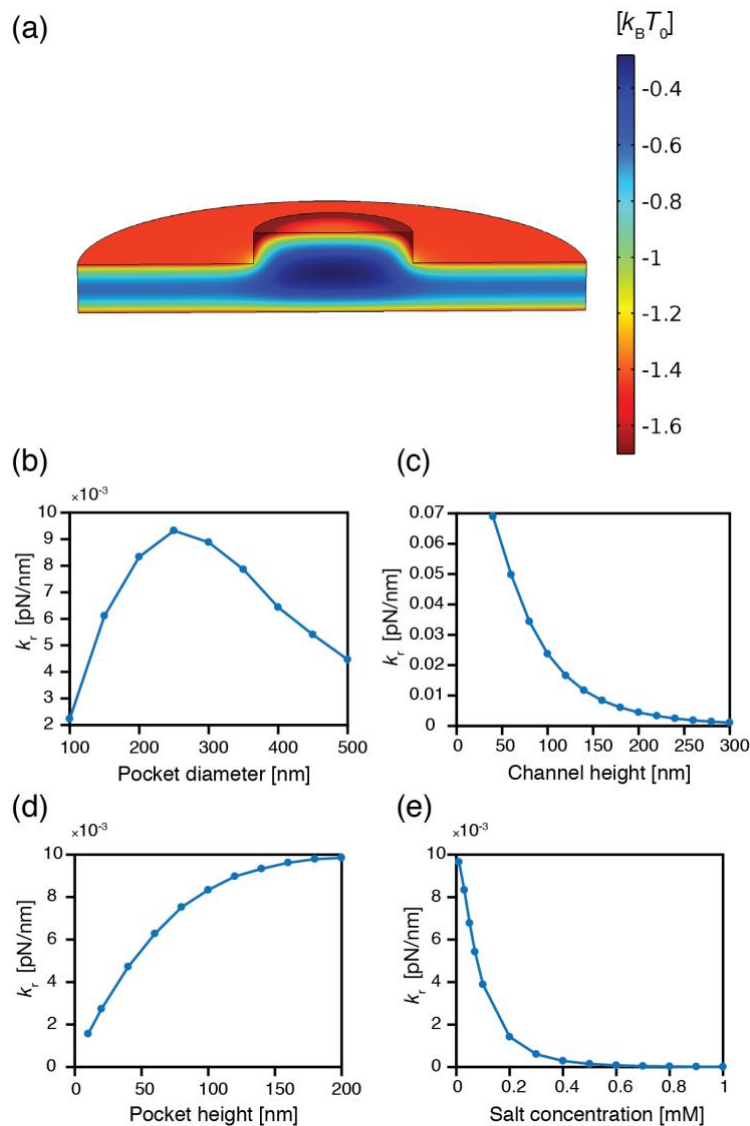


Figure 5.3. (a) Electrostatic energy distribution for a point charge with 1e net charge inside a GIE-trapping geometry. A 3D electrostatic simulation was performed using point charge approximation for a geometry comprising of a 160 nm high nanochannel, a 100 nm high and 500 nm wide nanopocket and the salt concentration being 0.03 mM. The color bar denotes the value of electrostatic energy for a 1e point charge ($U_{el} = e\psi$) in units of $k_B T$. Simulated results of electrostatic potential for point charge approximation were further used to calculate the stiffness constants (k_r) of a point charge with net charge equivalent to the net charge of an 80 nm diameter particle as a function of different geometrical parameters. (b) Stiffness constants for point charge approximation of 80 nm diameter particle with net surface charge (-132e) as a function of nanopocket diameter when all other parameters were kept constant ($H_c = 160$ nm, $H_p = 100$ nm, $C_0 = 0.03$ mM). (c) Stiffness constants for 80 nm charged nanoparticle ($q_{net} = -132e$) as a function of channel height when $D_p = 200$ nm, $H_p = 100$ nm, and $C_0 = 0.03$ mM were kept constant. (d) Stiffness constants as a function of nanopocket height with $D_p = 200$ nm, $H_c = 160$ nm, and $C_0 = 0.03$ mM, and (e) stiffness constants as a function of salt concentration while $D_p = 200$ nm, $H_c = 160$ nm, and $H_p = 100$ nm were constant.

In this study, we have performed simulations to understand the impact of pocket diameter by varying D_p from 100 nm to 500 nm. Similarly, the impact of variations in channel height, pocket height, and salt concentration was studied by varying $H_c = 40$ nm to 300 nm, $H_p = 10$ nm to 200 nm, and $C_0 = 0.01$ mM to 1 mM, respectively.

Stiffness constant profiles extracted using the point-charge approximation as a function of the pocket diameter (Figure 5.3) shows an increment in the stiffness (k_r) of the particle trapping until 250 nm diameter and reduction for larger trap diameters. This behavior of the particle confinement can be understood from the potential well profile shown in Figure 5.4. Broadening of the pocket diameter leads to an increment of the potential depth as well as a broadening of the potential well around the trap center. An increased depth of a potential trap increases the residence time of the particle inside the trap, and a broad tip of the potential curve around the center location of the potential trap increases the scope of particle diffusion inside the potential trap resulting in a lesser stiff confinement of the particle.

Observed variation of the stiffness constant as a function of pocket diameter is also consistent with the experimental results, as shown in Figure 5.5 and Table 1, where experiments were conducted for negatively charged 80 nm diameter particle trapping using PDMS based GIE-trapping devices with the geometrical parameters similar to the simulated geometry $H_c = 160$ nm, $H_p = 100$ nm, $C_0 = 0.03$ mM²³⁶. As shown in Table 1, the increment in stiffness constant values for 200 nm pocket diameter from 500 nm is evident, indicating the behavior observed using point charge approximation simulations (Figure 5.3b).

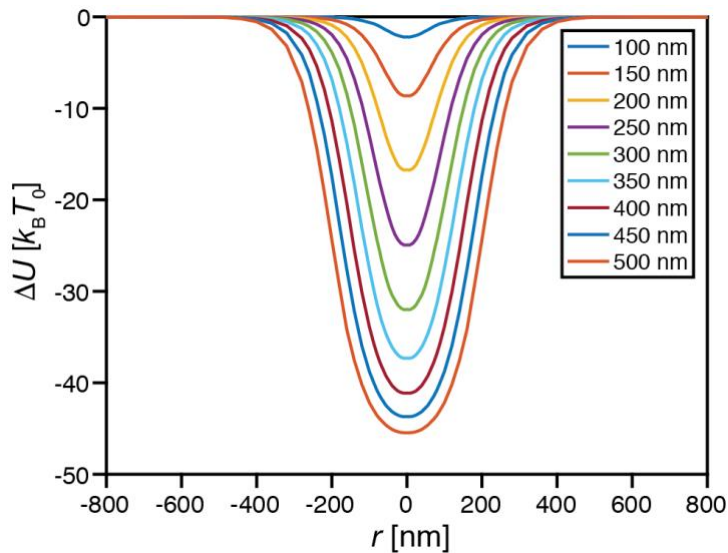


Figure 5.4. Free energy distribution profiles of a point charge ($q = -132e$) as a function of radial locations (r) from the center of the trap ($r = 0$ nm) for different pocket diameters (100 nm to 500 nm), while the channel height = 160 nm, pocket height = 100 nm, and salt concentration = 0.03 mM were constant. The difference of the free energy was calculated w.r.t the particle (point charge in this case) location outside the nanopocket region. The depth of the curve denoted the change in the particle energy when the particle is trapped inside the nanopocket.

	Stiffness constant for 500 nm pocket (pN/nm)	Stiffness constant for 200 nm pocket (pN/nm)
Experiment	0.0040 ± 0.0033	0.0111 ± 0.0070
Simulation - point charge	0.0045	0.0083
Simulation - particle	0.0027	0.0043

Table 1. Experimental data comparison with the simulated results obtained using point charge approximation, and charged nanoparticle, for pocket diameters of 500 and 200 nm.

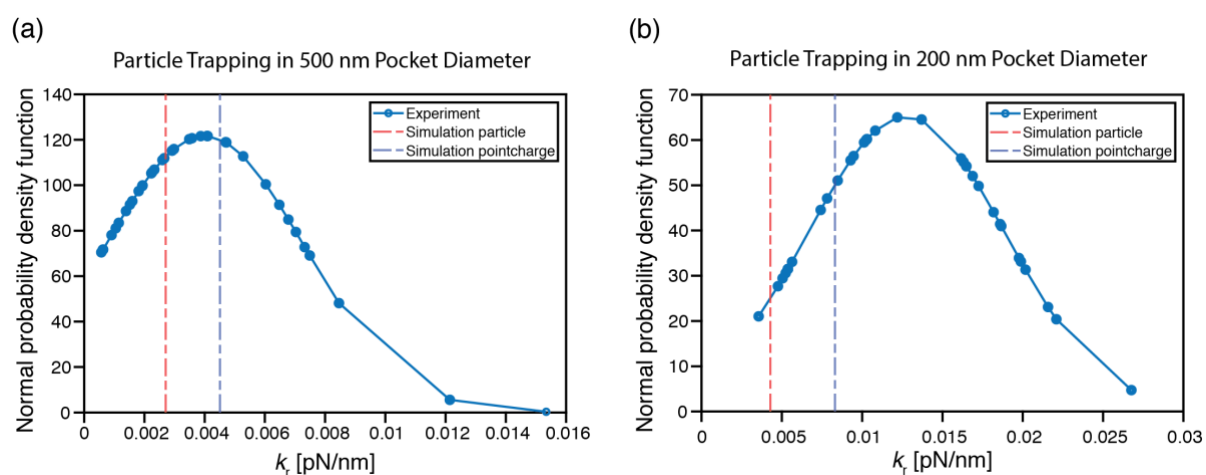


Figure 5.5. The normal probability density function for experimental observation as a function of trapping stiffness constant for a) 500 nm pocket diameter and b) 200 nm pocket diameter. Experiments were performed for negatively charged 80 nm diameter particles using PDMS-based GIE-trapping device with geometrical parameters $H_c = 160$ nm, $H_p = 100$ nm, $C_0 = 0.03$ mM. Simulations for the same device geometry and same charged nanoparticle were used to calculate stiffness constant, presented as dashed lines. Stiffness constant value obtained using charged nanoparticle (red) lies at the lower end of the experimentally observed stiffness constant values, whereas the result from point charge approximation (violet) is shifted towards the increased stiffness constant.

Unlike the trend of particle trapping due to pocket diameter, an increment in the channel height reduces the stiffness of particle trapping resulting in reduced stiffness constant, as shown in Figure 5.3(c). This suggests loose particle trapping in a higher channel compared to much stiffer trapping of the particle in a shorter channel. This effect can be explained further based on the profiles of electrostatic potential trap presented in Figure 5.6(a). Free energy curves in Figure 5.6(a) show the reduction of the potential depth as well as the steepness of the electrostatic trap with the increment in the channel height, which causes the reduction of both the residence time and the stiffness constant (Figure 5.3(c)). This enables the possibility of tuning the particle trapping by changing the channel height. Our experimental data published in previous work also validate this behavior for a tunable GIE-trapping device

where the strength of particle trapping was modified by tuning the channel height.^{84,125} Tunability of particle trapping by changing the channel height gives the flexibility to perform particle dynamic studies for various trapping strengths using a single device. Additionally, the impact of channel height on stiffness constant for different particle diameters is further presented in Section 5.6.1, Supporting Information.

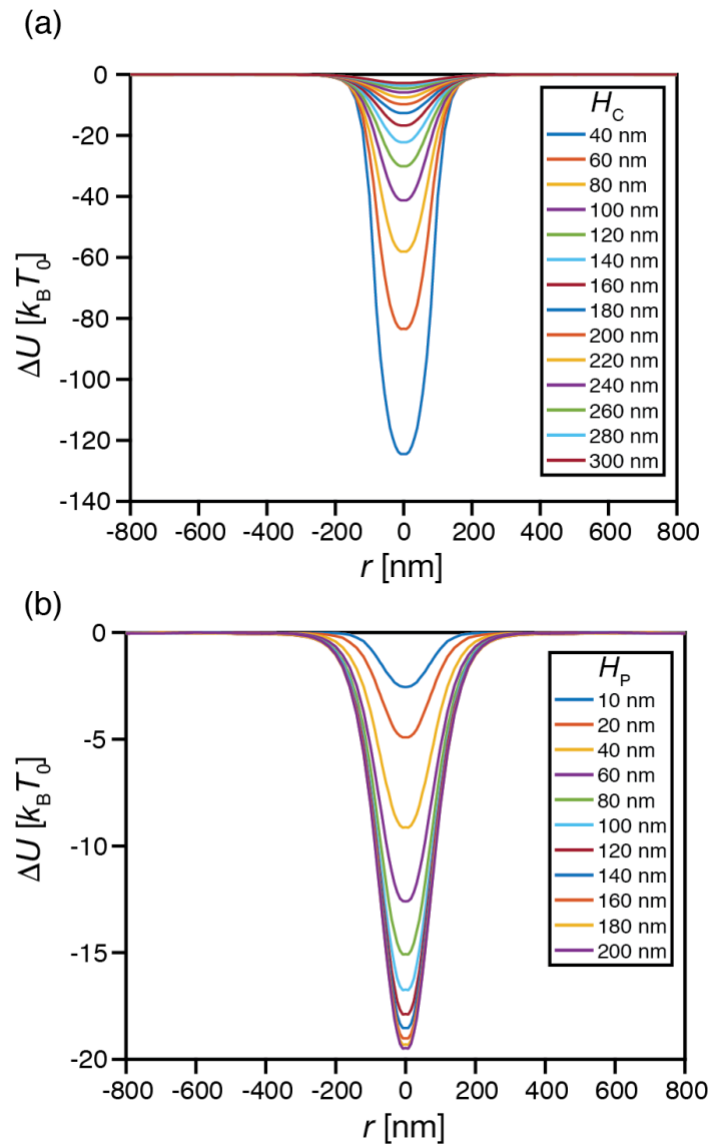


Figure 5.6. Profiles of the free energy distribution for electrostatic traps within the point charge approximation as a function of particle radial locations (r) with respect to the center of the trap ($r = 0$ nm) for different a) channel heights, and b) pocket heights respectively. Pocket diameter of the electrostatic trap and salt concentration used were 200 nm and 0.03 mM, respectively. While varying channel heights, the pocket height was kept constant at 100 nm, similarly when pocket heights were varied the channel height was kept constant at 160 nm. The free energy was calculated for a point charge with a charge equivalent to the net charge of a negatively charged 80 nm diameter particle ($q = -132e$).

While increments in channel height reduce the stiffness of the particle trapping, increased pocket heights improve the stiffness constant for the electrostatic trapping (Figure 5.3(d)). In case of the pocket height, both potential depth and trap steepness increase with the increment in the trap height (Figure 5.6(b)). Thus, making the particle trapping stronger and resulting in an increased stiffness constant (Figure 5.3(d)). However, the successive increment of the potential depth and trap steepness becomes infinitesimal for pocket heights greater than 180 nm as the stiffness constant value reaches a plateau around 180 nm pocket height.

In the case of the salt concentration (Figure 5.3(e)), higher salt concentrations of the buffer solution develop strong electrostatic screening of the electric field from the charged substrate and particle surface, leading to negligible stiffness constants for $C_0 > 1$ mM. The stiffness constant at $C_0 = 1$ mM reaches 1.05×10^{-5} pN/nm. Thus, the most effective electrostatic trapping of charged particles using this method is feasible for buffer solutions at low salt concentration.

Parametric studies for GIE-trapping devices make the device optimization process much faster for applying specific electrostatic trapping of nanoparticles of interest. However, while estimating the final device design, particle size and hydrodynamic radius must be taken into consideration for appropriate channel heights and pocket sizes. Therefore, simulations with a particle, considering its shape as well, inside the GIE-trapping region are required to understand the difference between point-charge approximation-based results and the real case scenario.

5.3.2 Particle Inclusive Simulation Results

GIE trapping of a particle depends on the geometrical parameters of the fluidic device as well as the particle-device electrostatic interactions. Thus, for realistic estimations and final optimization of the device, it is important to perform electrostatic simulations by incorporating a charged particle, considering its physical shape as well, in the simulations. For this study, we added an 80 nm diameter negatively charged particle with a total surface charge (q) of $-132e$ inside the nanochannel. To calculate the self-energy of the entire system including the particle as a function of particle location, simulations were performed for different radial locations of the particle inside the nanochannel and nanopocket, as shown in Figure 5.6. For every radial location of the particle, a location of minimum potential energy of the particle along z-axis ($z_{min} | r$) was extracted using the point-charge approximation simulations described in Section 5.3.1. Thus, for particle inclusive simulations, the particle was located at $(r, z_{min} | r)$, which is the position where a spherical particle receives minimum repulsion from the device surfaces and thus the system attains minimum self-energy for that specific radial location. To perform simulations including the particle, one additional boundary condition was applied at the boundary of the particle for the field discontinuity as $\hat{n} \cdot (D_1 - D_2) = \rho_p$, where ρ_p is surface charge density of the particle. To solve the Poisson equation inside the particle, $\nabla \cdot D = 0$ was defined for the particle region since the volume charge inside the particle was zero.

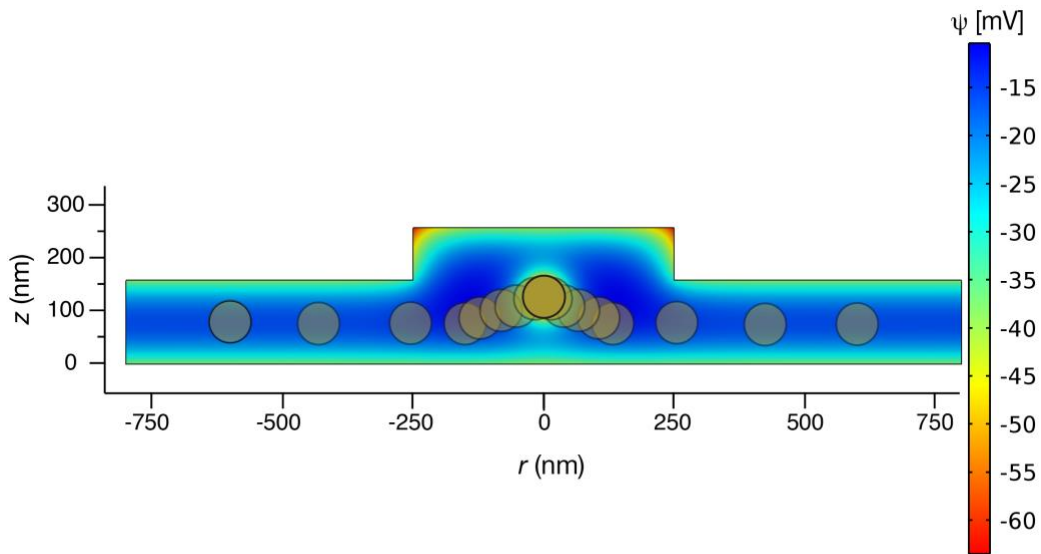


Figure 5.7. Electrostatic potential distribution inside a nanochannel ($H_c = 160$ nm, $C_0 = 0.03$ mM) embedded with a nanopocket ($H_p = 100$ nm, $D_p = 500$ nm), when a negatively charged 80 nm diameter particle ($q = -132e$) is trapped at the location of minimum potential self-energy at the center of the trap. Trajectory of the particle from the nanochannel to the location of the confinement is demonstrated both in radial and axial directions using circles. The color bar shows the potential values in mV.

Based on particle inclusive electrostatic simulations, free energy of the system was calculated using the self-energy and entropy of the system as a function of particle position. In the potential trap, the particle moves both in axial and lateral directions, as shown in Figure 5.7, however, the dependency of the Helmholtz free energy on the axial displacement of the particle is nearly linear. The effect of radial location of the particle on the system free energy is shown in Figure 5.8, which shows a bell curve. Approximating the free energy curve in the range of pocket ($r = -100$ to 100 nm) gives a harmonic curve approximation of the potential trap. Using the harmonic potential well approximation, the stiffness constant of the trap can be calculated using $\Delta F = 1/2 k_r r^2$, where k_r denotes the radial stiffness constant of the potential trap. Figure 5.8 shows the stiffness constant calculated for 80 nm diameter charged particle for 200 nm and 500 nm diameter pocket while channel height, pocket height, and salt concentration were kept constant. The stiffness constant values obtained using particle incorporated simulations was ≈ 0.5 times for 500 nm diameter pocket and ≈ 0.6 times for 200 nm diameter pocket of the values obtained using point-charge approximation, which is due to the broadening of the free energy curve, as shown in Figure 5.8.

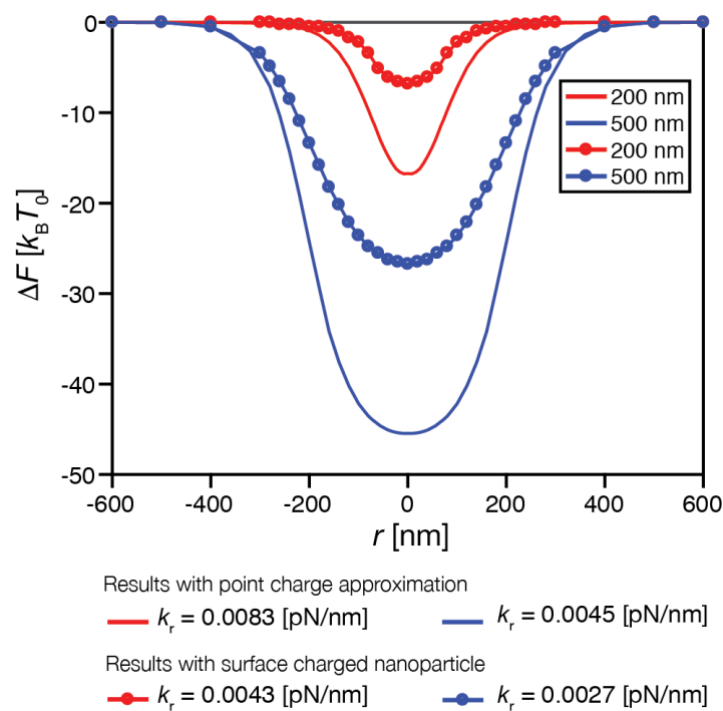


Figure 5.8. Free energy distributions for a fluidic system with a nanochannel ($H_c = 160$ nm) with an embedded nanopocket ($H_p = 160$ nm) of diameter 200 nm (red) and 500 nm (blue) and salt concentration 0.03 mM. Plots with circles denote the free energy difference as a function of particle location from the center of the trap ($r = 0$ nm), where simulations were performed with an 80 nm diameter particle located at different radial locations at the position of minimum potential energy along the z -axis. Each data point represents a separate simulation. Straight line plots denote the free energy distribution as a function of the radial position of a point charge with $q = -132e$. Stiffness constant (k_r) values for respective plots were calculated using harmonic potential approximation beneath the nanopocket region.

In comparison to the experimental data, as shown in Figure 5.5, the simulation result for charged particle lies at the lower end of the experimentally observed stiffness constant. While simulated result gives expected stiffness constant values for the charged nanoparticle in the simulated device geometry, it leaves out some other factors that can influence the particle trapping such as particle diameter and surface charge density variation (see Sections 5.6.2 and 5.6.3, Supporting Information), initial velocity of the particle before coming into the potential trap, etc. However, the advantage of simulated results is that the probability of a particle getting trapped with stiffness constant is equal to or higher than the simulated result is higher for the optimized GIE-Trapping device, as shown in Figure 5.5.

In comparison to the charged particle simulation result, point charge approximation simulation result overestimates the stiffness value of a stably trapped nanoparticle and thus misses out a part of experimentally observed stiffness constant values that would be associated with a stable electrostatic trapping (Figure 5.5). Therefore, for GIE-trapping device optimization to increase the percentage of stably trapped nanoparticle, preferred simulations are charged particle inclusive simulations. Although, the trend of the free energy profile and

consequently stiffness constant in both cases was the same, proving that point-charge approximation data can be used for a rough estimation of the relative trapping strength and GIE-trapping device optimization.

5.4 Conclusions

Parametric studies of GIE trapping are important for both understanding the properties of trapping devices and the optimization of fluidic devices for improving their trapping efficiency. Since the trapping strength of an electrostatic potential trap depends on the geometry of nanostructures, these simulations play a crucial role to analyze the effect of the geometry on the feasibly achievable confinement of the particle. Using simulations with particles is of great importance to save experimental time so as to fabricate devices with a priori estimated trapping properties. In this study, we have performed both simplified and realistic simulations for electrostatic trapping of an 80 nm diameter particle inside a GIE-trapping fluidic device. The detailed study of the impact of various geometrical parameters and the salt concentration of the buffer solution was conducted using point-charge approximation where the particle was replaced with a point charge, enabling faster simulations and analyses. The point-charge approximation can also be used to verify experimental data as also published in our previous work¹²⁵. For precise information of the device functionality and particle trapping, it is necessary to perform simulations by incorporating the real dimensions of the particle. We believe that the current detailed study of the properties of electrostatic confinement will help to expand the applicability of the method in different domains for particle trapping and molecular dynamic studies.

5.5 Acknowledgments

The research work was performed under the project P1310 funded and supported by the Swiss Nanoscience Institute, Basel, Switzerland.

5.6 Supporting Information

5.6.1 Optimal pocket diameter for stiffer particle trapping

Using an optimal pocket diameter for particle trapping can help confine single nanoparticle strongly in a potential well. The value of pocket diameter with maximum stiffness constant depends on the channel height when the pocket height and salt concentration during experiments are kept constant. For higher channel height, the peak of k_r vs D_p curve becomes flat, as shown in Figure 5.9. While the trend of stiffness constant is similar for the two channel heights (160 nm and 200 nm) used in the simulation, the peak gets a flat shape for 200 nm channel height, indicating the reduced impact of pocket diameter in the range of $D_p \approx 200$ nm to 350 nm.

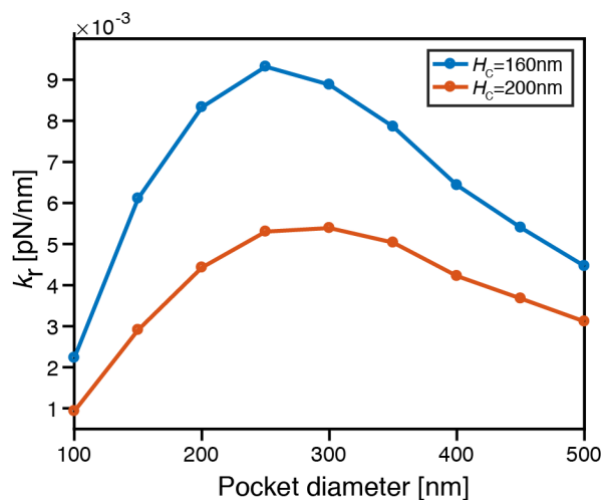


Figure 5.9. Variation of stiffness constant using point charge approximation for a negatively charged 80 nm diameter particle with a net charge of $-132e$ as a function of pocket diameter for a device with $H_c = 160$ nm (blue) and 200 nm (red). Other parameters $H_p = 100$ nm, $C_0 = 0.03$ mM were kept constant.

5.6.2 Impact of particle surface charge on stiffness constant

The net surface charge of a particle affects the stiffness constant of the trapping inside the potential well. A particle with a higher charge would have a higher stiffness constant while keeping the device geometry and salt concentration constant, as shown in Figure 5.10. The impact of particle charge variation is stronger for 200 nm diameter pockets compared to a 500 nm diameter pocket, where all the other geometrical parameters were kept constant.

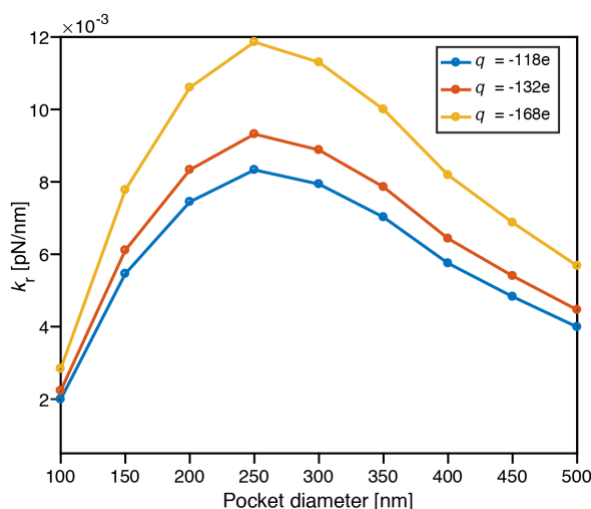


Figure 5.10. Variation of stiffness constant as a function of pocket diameter for different charges of the trapped particle, here $H_C = 160$ nm, $H_P = 100$ nm, $C_0 = 0.03$ mM. The simulation results were obtained for an 80 nm diameter charged nanoparticle with $q = -118e$ (blue), $q = -132e$ (red), and $q = -168e$ (orange), using point charge approximation simulations.

5.6.3 Difference between experimental and numerical results from particle-based simulations

The batch of 80 nm diameter nanoparticles used for the single particle trapping experiments varied in size with a mean diameter = 78.7 nm with the coefficient of variation of nearly 8%. The net charge of the single particles measured using zeta potential measurements also showed a variation of net charge of the particle ranging from $-118e$ to $-168e$, giving a broader range of particle net surface charge in the solution. Therefore, the mean of the trapped particles captured during experiments can vary from the ideal simulation condition. In simulation, mean value ($q = -132e$) of particle net surface charge from zeta measurements was used with particle diameter = 80 nm. However, the final experimental values (Figure 5.5) indicate that the mean value of the net charge of particles captured during experiments is larger than $q = -132e$, especially for 200 nm diameter pocket data. Therefore, the simulated values lie at the lower end of the distribution. As shown in Figure 5.11, increasing the particle charge value would bring the particle-based simulation close to the mean of the experiments.

The point charge approximation does not consider the size of the particle and therefore leads to a deeper and steeper free energy distribution curve (Figure 5.8), leading to higher stiffness constant of the trapped particle. In contrast, the particle-based simulation results take into account the presence of the particle surface and its interaction to device walls, leading to a broader and comparatively shallow free energy distribution curve. Therefore, the stiffness

constant both in experiments and in particle-based simulation is lower than the stiffness constant obtained using point charge approximation.

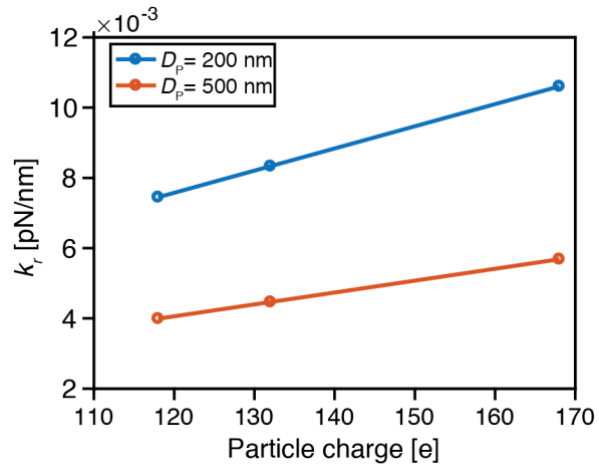


Figure 5.11. Change of stiffness constant of an 80 nm diameter charged nanoparticle with net charge value of $-118e$, $-132e$, and $-168e$. The results were simulated using point charge approximation for pocket diameter = 200 nm (blue), and 500 nm (red). The other device parameters $H_c = 160$ nm, $H_p = 100$ nm, $C_0 = 0.03$ mM were kept constant.

Chapter 6. Nanofluidic Devices for Particle Trapping and Molecular Sensing

6.1 Introduction

In previous chapters, we focused on the development and optimization of high-throughput GIE-trapping devices for electrostatic trapping of charged nanoparticles, which are useful for molecular dynamic and molecule-molecule interaction studies. However, to perform molecular detection at very low concentrations from bodily fluids like blood and urine, we require a new platform that allows for preconcentration of molecules inside the nanofluidic devices for molecular detection through various detection methods such as surface-enhanced Raman spectroscopy (SERS), UV-vis spectroscopy, and fluorescence microscopy.

As described in Chapters 3-5, integrated micro- and nanofluidic devices utilize both surface-specific properties of nanostructures as well as controlled fluid dynamics of microstructures to provide a platform for molecular dynamic²³⁷ and intermolecular interactions studies²³⁸ and molecular sensing²³⁹ for nanoscale molecules at low concentration. Furthermore, micro- and nanofluidic devices can also be used for molecule separation²⁴⁰, sorting²⁴¹, and trapping^{112,242}. Thus, utilizing micro- and nanofluidics combined with bioconjugated nanoparticles to achieve analyte preconcentration inside a lab-on-a-chip platform can provide a robust and universal platform for analyte detection at very low concentrations from a very small volume.

Analyte preconcentration to detect molecules such as proteins, peptides, biomolecules, and metal ions at very low volumes and concentrations is generally achieved using magnetic nanoparticles²⁴³⁻²⁴⁶, nano-capillary channels²⁴⁷, electrophoresis²⁴⁸, gold nanoparticles²⁴⁹, carbon nanotubes²⁵⁰, etc. For final analyte quantity and signal identification, detection methods such as absorption spectroscopy, flow cytometry, fluorescence microscopy, and Fourier-transform infrared spectrometry (FTIR) are used. The main advantage of analyte preconcentration is that it can be used in any solution irrespective of the salt concentration of the solution, making it effective for bodily fluid and salt-water-based detection.

To achieve preconcentration of biomolecules and other analytes for efficient analyte detection at very low concentrations in both high and low salt concentration solutions, we combined nanoparticle trapping and manipulation methods into a nanofluidic device. To achieve nanoparticle trapping, we exploited integrated micro- and nanofluidics for hydrodynamic trapping of bioconjugated nanoparticles that can adsorb analytes from the solution. Hydrodynamic trapping^{181,251-255} has been used extensively for single cell trapping and analysis in microfluidic devices; however, incorporating it in nanofluidic devices for nanoparticle trapping has been a major challenge. In hydrodynamic trapping, hydrodynamic forces and fluid flow are utilized to immobilize and manipulate particles either for contact-based²⁵⁴⁻²⁵⁶ or contact-free confinement of particles.²⁵⁷ Physical hydrodynamic trapping

based on microfabricated obstacles or channel walls is helpful in achieving high-throughput trapping of a large number of particles.^{257,258}

To expand the scope of the device in the direction of multi-molecular sensing using different sizes of nanoparticles, we combined hydrodynamic trapping with deterministic lateral displacement (DLD) arrays that can be used to manipulate nanoparticles' motion to trap in different locations. DLD arrays have been in use to achieve directional motion of particles for size-based particle separation or trapping.^{134,136,140,259} For DLD of particles based on their size, an array of posts of different shapes, such as circular, rectangular, and triangular, can be used with a fixed or varying lateral shift across the fluidic channel, as discussed in Chapter 2. The DLD arrays create a specific streamline pattern based on the periodicity of the arrays and help the particles that are smaller than the critical diameter to travel in the direction of laminar streamline through the pillar array and particles that are larger than the critical diameter to flow in a zigzag pattern.²⁶⁰ This leads to the separation of particles based on their size.

Trapped nanoparticles with adsorbed analytes can be detected using different detection methods such as SERS, Fluorescence microscopy, FTIR, and UV-vis spectroscopy. Among various detection methods, SERS can detect analytes with a sensitivity of a few pg/ml. SERS measurements using gold²⁶¹ and silver nanoparticle²⁶²⁻²⁶⁴, nanorods²⁶⁵, nano-patterned surface²⁶⁶, etc., have been extensively in use for bio- and molecular sensing^{150,173}. SERS-enhanced surface enhances the Raman signal of the analytes adsorbed on the surface and provides a means of performing multi-analyte detection with high precision.^{261,265}

Combining hydrodynamic trapping and DLD arrays for nanoparticle trapping and analyte detection, we developed a lab-on-a-chip platform by integrating micro- and nanofluidics. The device was specifically designed to use functionalized nanoparticles for early disease diagnosis, where nanoparticles can be functionalized with disease-specific or analyte-specific antibodies. Antibody functionalized nanoparticles can be purchased directly or prepared in the laboratory using surface chemistry. To perform experiments for disease-specific biomarker detection, one needs to mix the nanoparticles with body fluids and inject them through the inlet area into the LoC platform. The device uses different chambers to sieve out unwanted biomolecules from analyte-adsorbed nanoparticles, provide directional motion of nanoparticles for size-selective nanoparticle trapping in the detection area, and trap nanoparticles at different locations in the detection area based on their diameter for analyte detection. Trapped nanoparticles inside the detection area can be used as SERS probes to enhance the Raman spectra of the molecules attached to these nanoparticles, providing both qualitative and quantitative information on the attached analyte or disease-specific biomarker. In combination with optical detection using SERS and localized surface plasmon resonance (LSPR), a highly sensitive (~10 pg/ml) molecular detection can be achieved.^{267,268} To demonstrate the manufacturability and performance capability of the proposed lab-on-a-chip platform for molecular detection, we have performed preliminary experiments using gold nanoparticles.

6.2 Materials and Methods

6.2.1 Device Design

The device has one inlet and one outlet location, as shown in Figure 6.1. Both inlet and outlet locations were patterned with circular pillars to support microstructures and avoid pattern collapsing after transferring the device pattern to elastic materials such as polydimethylsiloxane (PDMS). The outlet area was patterned with 3 μm and 15 μm diameter circular pillars with 7 μm and 15 μm inter-pillar spacing, respectively, as shown in Figure 6.1. The inlet area was patterned with the 15 μm diameter pillars with a 15 μm inter-pillar spacing. For micro and macro-particle separation from the sample solutions, 3- μm -wide pillars are patterned with a 2 μm inter-pillar spacing and connected with an area patterned with $5 \times 3 \mu\text{m}^2$ rectangular pillars rotated at an angle of 48.37° with 6 μm and 6.6 μm inter-pillar spacing in axial and lateral directions of the flow, respectively. The micro and macro particle separation area was directly connected with nanochannels embedded with DLD arrays. DLD arrays were achieved using 2 μm diameter pillars with 1 μm and 500 nm inter-pillar spacing. DLD arrays were achieved for periods $N = 1, 2, 3, 10, 20$ with 1 μm inter-pillar spacing and for $N = 1, 10, 12, 18, 25$ with 500 nm inter-pillar spacing. Patterned DLD arrays allow for nanoparticle separation and promote directional motion of nanoparticles, helping them to be trapped in a specific direction. In the particle detection area, steps were patterned with different heights to trap different particles at different step locations based on the particle size, as shown in Figure 6.1 and Figure 6.2. Steps were supported by pillars to avoid pattern collapsing, as shown in Figure 6.2.

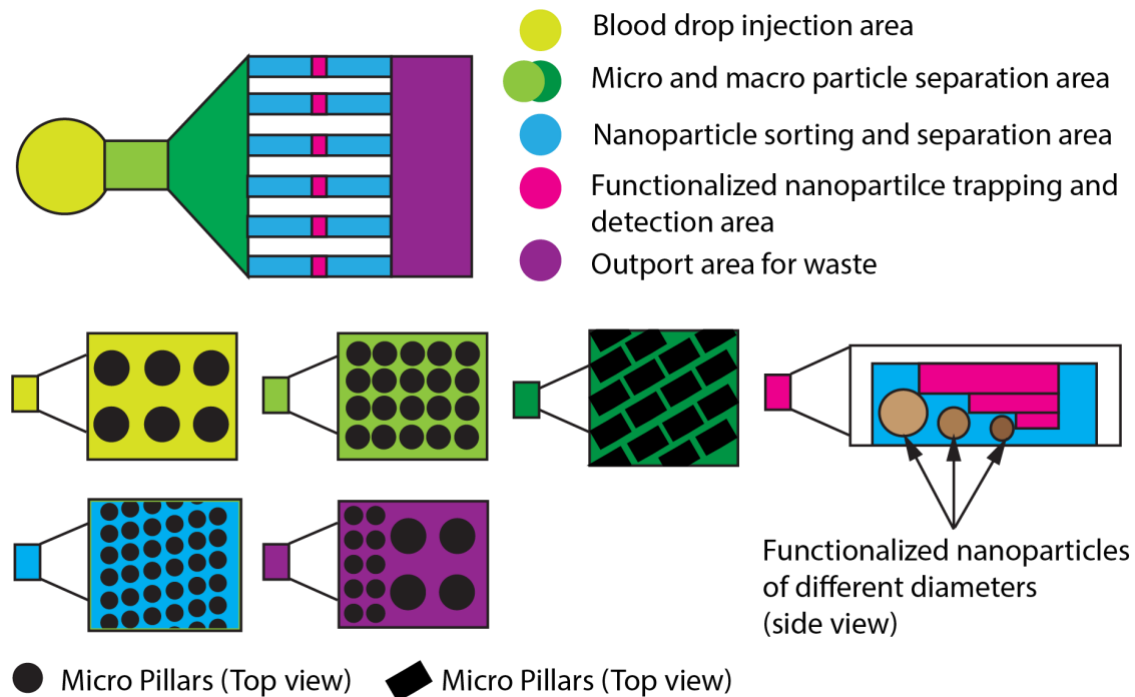


Figure 6.1. Schematics of a lab-on-a-chip platform (top view) for early disease detection using antibody-functionalized nanoparticles. The blood sample is injected at the inlet area in combination with functionalized nanoparticles allowing antibody-antigen binding on the nanoparticle surface, and detection of bound antibodies at the detection area. Injection area, micro and macro particle separation area, nanoparticle and separation area, all contain microarray pillars with different inter-pillar spacings, pillar periods, and orientations. The detection area consists of three different steps to allow for the size-based trapping of three different sized nanoparticles at different locations.

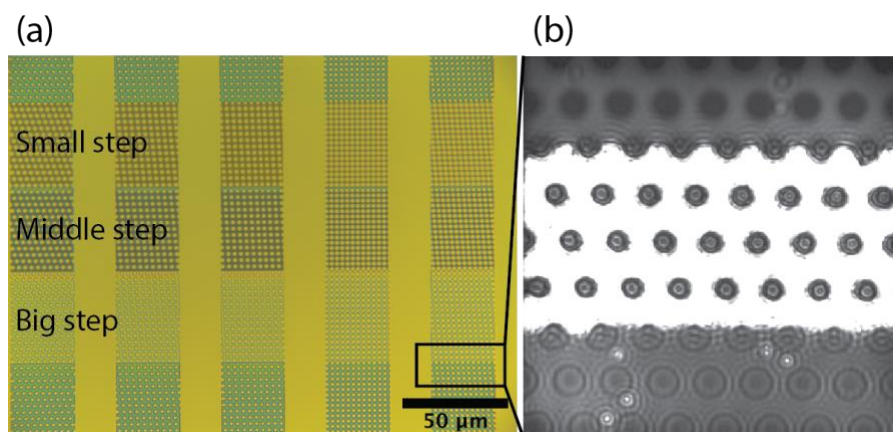


Figure 6.2. Nanochannels embedded with deterministic lateral displacement arrays and three steps for passive size-based trapping of three different nanoparticles (a). Trapping of 150 nm diameter gold nanoparticles at the location of Big step inside the nanochannel (b). Nanochannels are embedded with 2 μm diameter DLD pillars which also serve as supporting pillars for the nanosteps and nanochannels.

6.2.2 Device Development

The lab-on-a-chip (LoC) platform for biosensing applications was developed using state-of-the-art lithography processes and replica molding. A negative master was developed on a Si wafer using electron-beam lithography (Vistec EBP 5000 Plus). As shown in Figure 6.3, a silicon wafer was first sonicated under acetone and isopropyl alcohol (IPA) for 10 min in each solvent and then dried under nitrogen (N_2) gas stream. The cleaned wafer was further processed for 1 min in buffered hydrofluoric acid (BOE 7:1, $HF:NH_4F = 12.5:87.5\%$, General Chemical) and later washed thoroughly with deionized (DI) water and dried with N_2 . To proceed with the alignment marker patterning, the wafer was spin-coated (1000 rpm, 300 rpm/s, 60 s) with poly-(methylmethacrylate) (PMMA, 950K, 4% ethylacetate, Allresist) and pre-baked at 175 °C for 4 min. After the e-beam exposure of alignment markers, PMMA was developed under methyl-isobutyl-ketone (MIBK):IPA (1:1) for 60 s. A 60-nm-thick gold (Au) layer was thermally deposited (Univex, 1 Å/s) on the patterned wafer after the deposition of a 5 nm thin adhesion layer of chromium, transferring the patterns on the wafer. PMMA resist was removed from the wafer through acetone, IPA, and DI sonication (10 min each), and the cleaned wafer was processed with O_2 plasma for 2 min (power = 150 W, pressure = 150 mTorr, O_2 flow = 20 sccm, Oxford Instruments – Plasmalab80Plus).

Immediately after plasma cleaning, HSQ Fox16 (1:4) negative e-beam resist was spin-coated on the wafer (3000 rpm, 500 rpm/s, 60 s). E-beam exposure for small steps was done, and after the exposure, the resist was developed in AZ351:H₂O = 1:3 for 3 min. The wafer was further cleaned using O₂ plasma for 2 min, and HSQ Fox16 (1:3) resist was spin-coated (4000 rpm, 500 rpm/s, 60 s). The pattern for the middle step was exposed using the e-beam, and the resist was developed in AZ351:H₂O = 1:3 solution for 3 min. For the big step patterning, the wafer was O₂ plasma cleaned for 2 min and spin-coated with HSQ Fox16 (1:2) (1500 rpm, 500 rpm/s, 60 s) before e-beam exposure. The exposed resist was developed for 3 min, and the wafer was O₂ plasma cleaned for 2 min. The cleaned wafer was spin-coated with HSQ Fox (1:1) resist (1000 rpm, 500 rpm/s, 60 s) and then exposed with the pattern for nanochannels. After the development of the exposed resist for 3 min, the wafer was again cleaned with O₂ plasma and spin-coated with HSQ Fox (undiluted) resist (1000 rpm/s, 300 rpm, 60 s). The wafer was exposed with inlet and outlet areas and developed in the developer solution for 7 min and later sonicated in the developer solution for 6 min. The final thickness of small, middle, and big steps are approximately 78 nm, 100 nm, and 170 nm, respectively. The thicknesses of the nanochannels and the inlet/outlet areas are ~330 nm and ~885 nm, respectively.

The device pattern was transferred to a PDMS mold using replica molding, as shown in Figure 6.3, after performing gas phase silanization of the patterned silicon wafer. Silanization was performed inside a vacuum chamber using a mixture of 1:1 trichloro(1H,1H,2H,@H-perfluorooctyl) silane and (tridecafluoro-1,1,2,2-tetrahydrooctyl)dimethylchlorosilane for 10 min. For replica molding, UV curable PDMS base and curing agent mixture (Shin-Etsu Chemical Co. Ltd.) was used in a 1:1 weight ratio and cured for 4 min under UV exposure at 30mW/cm² and then baked at 50°C in an oven at atmospheric pressure. Patterned PDMS mold was further prepared for final device assembly by punching holes at inlet and outlet locations. Immediately before the final device assembly, a cleaned cover glass and a prepared PDMS mold were processed with air plasma for the activation of glass and PDMS surface for effective covalent binding. Before pressing both surfaces together, nanostructures of patterned PDMS mold were filled with 2.5 µl of DI water through capillary force action. Pre-filling of nanostructures in patterned PDMS surface avoids pattern collapsing during the glass-PDMS surface binding process.

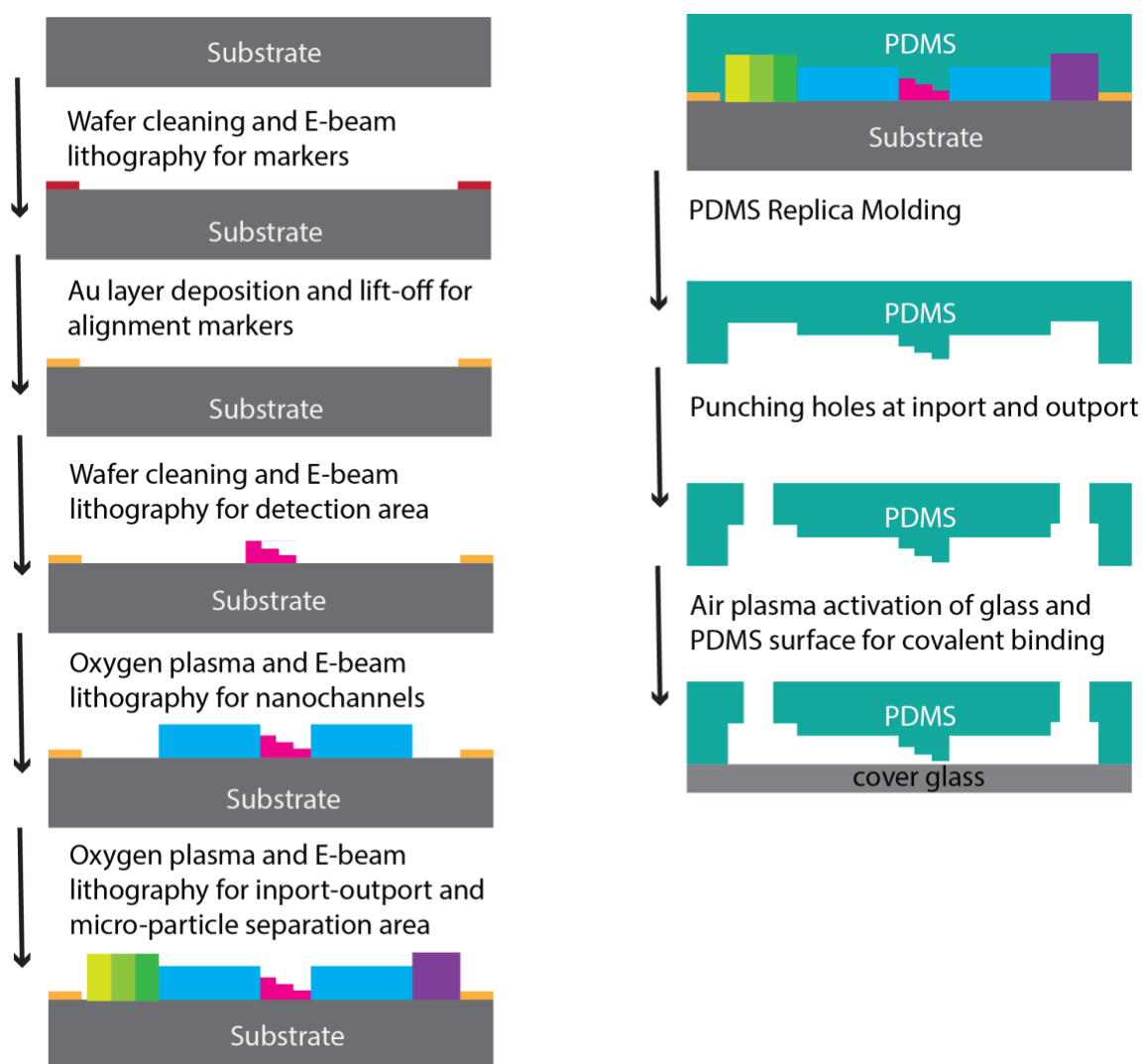


Figure 6.3. Schematics for fabrication and development of a lab-on-a-chip platform using state-of-the-art lithography processes on a silicon wafer and replica molding using polydimethylsiloxane (PDMS). The final integrated micro- and nanofluidic device was developed using air plasma activation of patterned PDMS and a cover glass.

6.2.3 Experiment Preparation

To identify the functioning of the developed device, we performed preliminary experiments using gold nanoparticles (Au NPs). For our preliminary experiments, we focused on 1) identifying if the size-based hydrodynamic trapping of nanoparticles is possible using nanosteps and 2) If DLD arrays can provide directional motion of nanoparticles that can be later used for size-based nanoparticle separation to enable multiplexable detection of multiple analytes, 3) If biomolecules can be separate out in the separation chamber from nanoparticles and can be stopped from reaching to the detection chamber. For 1st and 2nd points, we performed experiments with Au NPs of different diameters ranging from 60 nm to

200 nm (BBI Solutions). These Au NPs have the native —COOH functional group at the surface, which later can be used for nanoparticle surface functionalization. Our primary goal through these experiments was to detect —COOH group using SERS measurement. For 3rd point, a blood sample mixed with Au NPs was used for the experiment.

6.2.4 Optical Detection

For optical imaging of the sample and trapped particles, we used an in-house built interferometric scattering detection (iSCAT)^{85,113} setup. For the Raman spectroscopy measurements, an inverted microscope with an Acton SP2500 monochromator (Princeton Instruments) with 180 BLZ, 600 BLZ, and 1800 BLZ gratings, and a CCD detector (PROEM 1600x200 CCD207-00, Princeton Instruments) was used. A 532 nm laser-pumped solid-state laser was used to excite Au NPs for the SERS spectra of attached molecules.

6.3 Results and Discussions

To check the working efficiency of the developed device, we performed preliminary experiments for molecular detection, size-based nanoparticle sorting and trapping, and micro-particle separation using Au NPs.

6.3.1 Micro-Particle Separation

Microparticle separation experiments were performed using whole blood samples mixed with Au NPs. For detection of disease-specific biomolecule detection, it is important to separate red and white blood cells and platelets, including other micro and macro particles, from Au NPs at the detection area to achieve a high signal-to-noise ratio of SERS signal from the attached molecules on the functionalized nanoparticles. Thus, preliminary experiments were performed to identify the efficiency of the device in separating these particles prior to the nanochannel region in the LoC chip. Based on the performed experiments, we identified that for a mixture of 100 μl of the whole blood sample and 10 μl of (-ve) 80 nm of Au NPs, all macro and micro molecules were sieved out before the nanochannel region.

6.3.2 Nanoparticle Directed Displacement

Passive sorting of nanoparticles was achieved by deterministic lateral displacement (DLD)^{139,260,269} using different micro-structured arrays integrated on the LoC platform, as shown in Figure 6.4. DLD arrays support both size-based particle separation as well as the directional displacement of nanoparticles. In this work, size-based nanoparticle sorting and the directional motion were investigated using DLD arrays with 1 μm diameter pillars with 2 μm and 1 μm inter-pillar spacing in both axial and lateral directions of the flow. DLD arrays were patterned with an array period (N) of 0, 1, 2, 10, 100, 200, 300, and 600. First preliminary experiments were performed using 150 nm and 200 nm Au NPs to examine the efficiency of DLD arrays to allow motion of nanoparticles in the direction of the pillar array. During experiments, we observed that among all DLD arrays, the array with 1 μm inter-pillar spacing

and array period of $N = 10$ promoted directional motion of both 200 nm and 150 nm Au NPs, as shown in Figure 6.4. However, at the aspect ratio of (height : width) 1000 : 330, 1 μm diameter pillars inside the nanochannels collapsed during the experiments due to nanochannel drying. Furthermore, for an array of period $N \geq 100$, the lateral row shift was not sufficient enough to allow for a directed motion of nanoparticles along the array direction. Thus, the next generation of the LoC device design was developed using DLD arrays with a period lesser than 100 and inter-pillar spacing of 1 μm and 500 nm for a 2 μm diameter circular array, as mentioned in Section 6.2.1. The reduced aspect ratio of the pillars inside the nanochannel region provided stability to the pillars. However, the directional motion of nanoparticles for the new set of DLD arrays was not as effective as observed for 1 μm diameter pillars with an inter-pillar spacing of 1 μm . Therefore, further optimization of the DLD array would be required to achieve improved directional motion of nanoparticles for size-based separation of nanoparticles inside the nanochannel before reaching the detection area. This improvement would allow for a multiplexed detection on a single LoC platform.

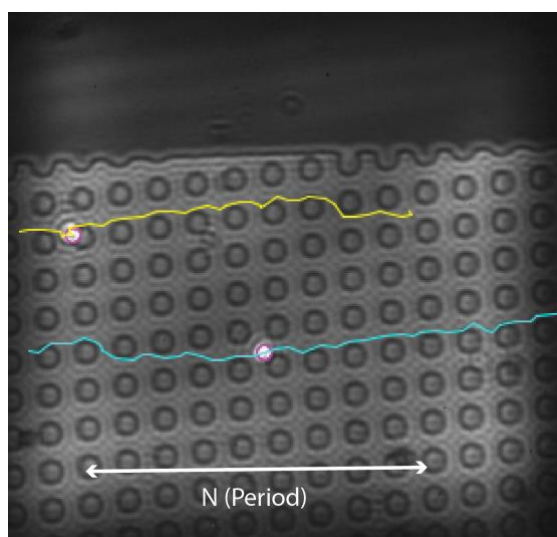


Figure 6.4. The microarray of 1 μm diameter pillars with 1 μm inter-pillar spacing inside the integrated micro- and nanofluidic device for size-based sorting of nanoparticle and directional motion of the particles of interest. The presence of deterministic lateral displacement arrays with a period of $N = 10$ assisted directional motion of nanoparticles with a diameter of 200 nm.

6.3.3 Nanoparticle Size-based Trapping

The detection area in the LoC platform was patterned with nanometric steps, as shown in Figure 6.1. The step structures allowed for passive size-based trapping of nanoparticles, leading to the possibility of multi-diametric particle detection at the detection area. In the current work, we performed experiments with two and three steps for 2 and 3 different diametric particles trapping at the detection region. We successfully achieved the trapping of nanoparticles (200 nm to 100 nm) at the first step, as shown in Figure 6.2, and the removal of (~ 60 nm) smaller particles through the opening. For the separation of 200 nm and 100 nm nanoparticles at the detection location, further optimization of step heights is required.

6.3.4 Molecular Sensing

Before performing preliminary experiments, we performed Raman measurements on various solvents for which Raman spectra are well known, as shown in Figure 6.5. Later molecular sensing experiments were performed in different buffer solutions using 80 nm diameter Au NPs, which consist of -COOH group on the particle surface. The presence of Au NPs in close vicinity in the detection area enhanced the electric field coupled with the particles leading to nanoparticle agglomeration and melting due to plasmonic heating^{270,271}. The agglomeration of Au NPs due to plasmonic heating led to a dramatic reduction in the field enhancement, which reduced the strength of Raman peaks, as shown in Figure 6.6. Moderate peaks related to -COO group are expected around $\sim 1315 - 1435 \text{ cm}^{-1}$ and $\sim 1610 - 1740 \text{ cm}^{-1}$ in the SERS spectra of Au NPs.²⁷²⁻²⁷⁴ Both peaks are visible in the collected SERS spectra, as shown in Figure 6.6. To take molecular sensing studies further, we would require to perform similar experiments with antibody-functionalized nanoparticles and analyte solution.

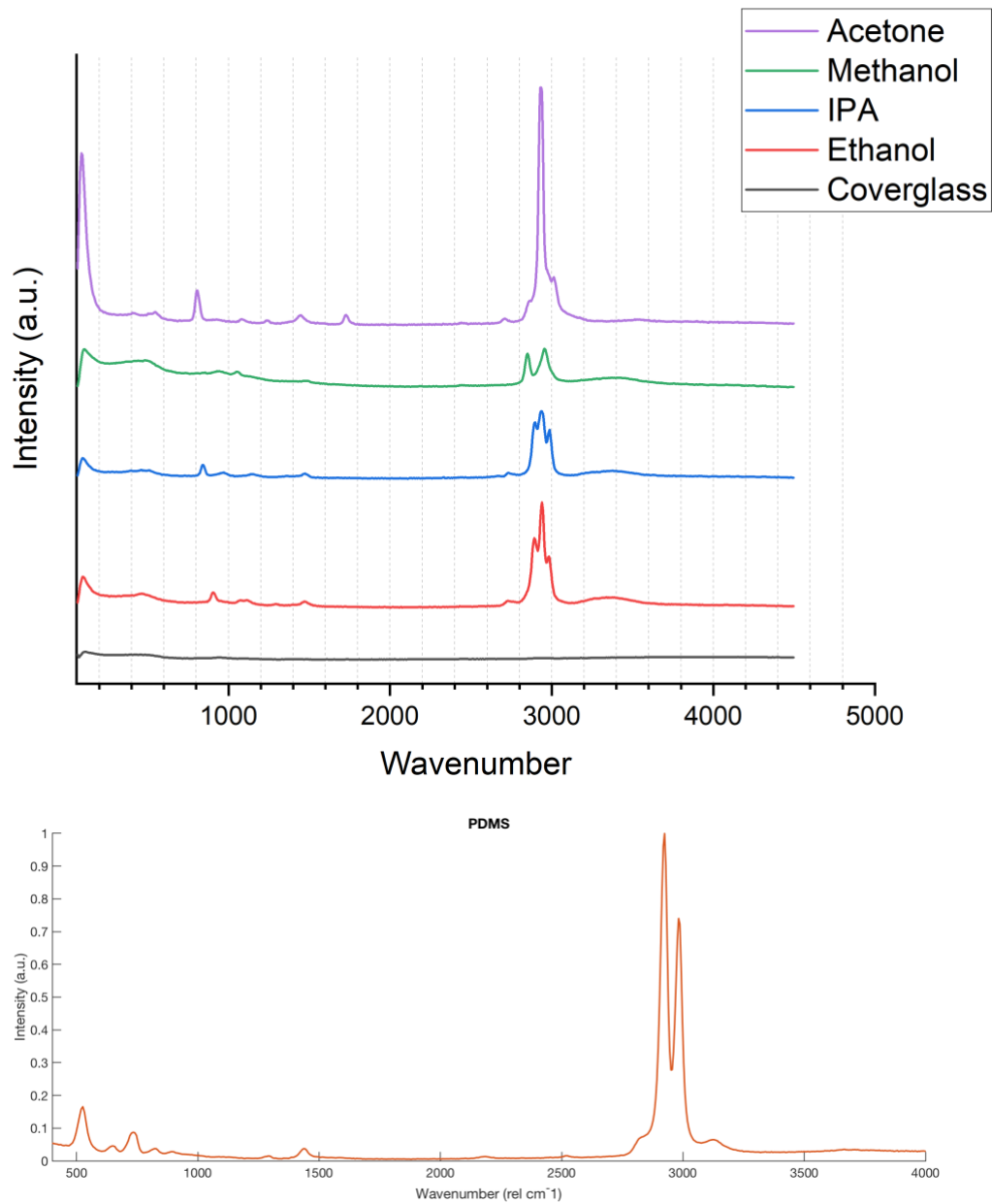


Figure 6.5. (Top) Raman Spectra of various solvent solutions and cover glass that is used in the lab-on-a-chip device fabrication. (Bottom) Raman spectra of PDMS device used for experiments.

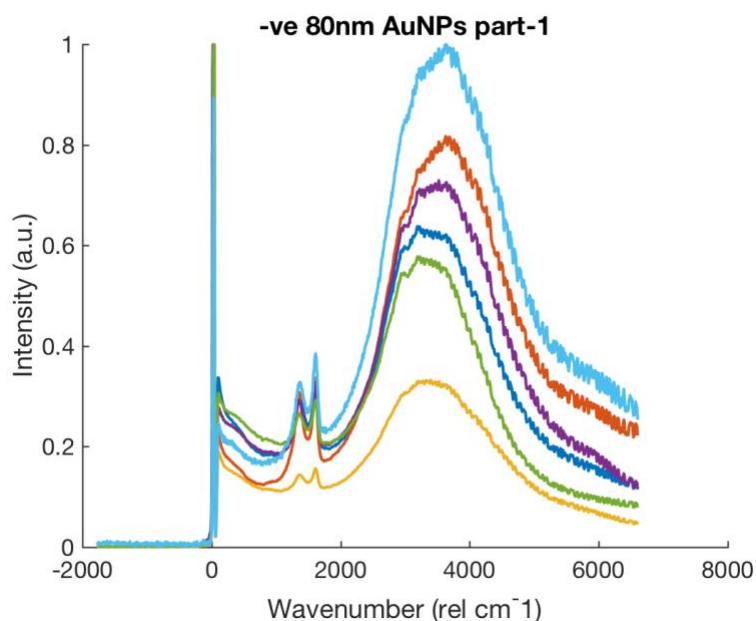


Figure 6.6. Photoluminescence and Raman spectra from trapped 80 nm diameter gold nanoparticles in the detection area. The agglomeration of nanoparticles causes the reduction of field enhancement factor and therefore overall reduction of the spectra intensity (blue to yellow spectra).

6.4 Conclusions

In our preliminary experiments, we successfully demonstrated that using DLD arrays, we could achieve directional motion of nanoparticles, and using hydrodynamic trapping through channel steps, we could achieve size-based particle trapping in the detection regions. In addition, we also demonstrated that by using gold nanoparticles, the SERS signal of molecules adsorbed on nanoparticles can be measured and used for molecular detection. Since in this work, we performed only preliminary studies to understand the feasibility, manufacturability, and functionality of the device; further optimization is required to make it a robust platform for size-based particle separation and multi-analyte detection in the same device.

We anticipate that with further optimization of device design and after detailed SERS measurement using functionalized nanoparticles and analyte solution, the proposed device and method would be useful for a multiplexable LoC platform that would allow multi-biomarker detection on a single chip possible.

Chapter 7. Conclusions and Outlook

Molecular studies in an aqueous environment have been crucial for both scientific and commercial purposes in performing molecular interaction studies, early disease detection, diagnosis, molecular sensing, and molecular analysis. Among various methods to perform these studies, passive molecular trapping has emerged as an important method of handling nanoscale objects in a controlled way in solutions. Among passive methods such as entropic trapping, geometrical trapping, electrostatic trapping, and hydrodynamic trapping, the electrostatic trapping method provides an effective platform for high-throughput nanoparticle screening and molecular dynamics and interaction studies. In contrast, the geometrical trapping method provides tools to conduct efficient molecular screening and sensing. While electrostatic trapping is most useful for charged nano-objects in an aqueous solution of low ionic concentration, geometrical trapping can be used for both charged and uncharged particles in diverse aqueous environments. This thesis has explored the development, optimization, and usage of electrostatic and geometrical trapping methods using integrated micro- and nanofluidic devices. The highlight of the conducted studies is presented in this chapter along with the perspectives of potential scientific studies and commercial applications and studies.

7.1 Conclusions and Prospective Applications of Electrostatic Trapping

The electrostatic trapping was achieved by optimizing the geometry of the nanofluidic device so that the electrostatic potential due to charged surface of the device overlaps to form an electrostatic potential well that can be used to trap a charged particle in a contact-free manner due to the electrostatic interactions leading to repulsive forces between the charged surfaces and the like-charged particle. Therefore, electrostatic trapping is also known as geometry-induced electrostatic (GIE) trapping. GIE-Trapping device performance can be tuned for the desired confinement strength for nanoparticles of interest for the trapping by optimizing the device geometry and surface charge density of the device surface. Conventional GIE-trapping devices that are produced using silicon, glass, or PDMS substrates can trap only negatively charged particles since SiO_x based surfaces attain net negative surface charge in an aqueous environment with $\text{pH} > 2$. Therefore, to trap positively charged particles in an electrostatic trap, the device surface was modified such that the device surface attained a net positive charge density. In this thesis, we have presented the procedure of surface modification of glass-based and PDMS-based GIE-trapping devices, which was exploited successfully to achieve both positively and negatively charged particle trapping in the GIE-trapping devices.

Along with the conventional GIE-trapping devices, tunable PDMS-based GIE-trapping devices were developed using PDMS-based GIE-trapping devices^{125,216}, where charged particles can be trapped and released by tuning the channel height of the nanofluidic device. Similarly, a GIE-trapping device can be developed to trap particles based on the size and net surface charge of the particle by optimizing the device design accordingly, as shown in Figure 7.1.

Size-based trapping can be used in different environments for scientific and biological studies, such as the activity analysis of pathogens, organisms, viruses, and ultramicrobacteria²⁷⁵, also known as nanobacteria, in different environments. Ultramicrobacteria is omnipresent and abundantly dominant in groundwater, ocean, lakes, and other aquatic ecosystems. Therefore, in-depth knowledge about their characteristics can help to improve their removal from drinking water in water treatment plants²⁷⁶. Similarly, various viruses and bacteria, such as mycoplasma^{277,278}, parvovirus²⁷⁹, and pandoravirus^{280,281}, that range in size from 20 nm to 1000 nm, can also be studied for their activity in different environments, which can help to advance the understanding of these organisms. Since GIE trapping is most effective in low or no-salt concentration solution, it can be used to study Halotolerant and non-halophile organisms²⁸², which can thrive in solution with no salt (e.g., NaCl)^{283,284}. Scientific research on halotolerant is relevant in the field of biochemistry, molecular biology, cell biology, physiology, ecology, and genetics and can be applied to areas such as agriculture, aquaculture, and xeriscaping.^{285,286} Additionally, by modifying the surface charge density of a device selectively, the same device can be used for trapping both positively and negatively charged objects in their respective areas, allowing the separation of opposite-charge organisms initially by adsorption and later by trapping of like-charged molecules in the trapping area, as shown in Figure 7.2. The separation and trapping area can be further optimized so that oppositely charged organisms can be completely adsorbed in the separation area.

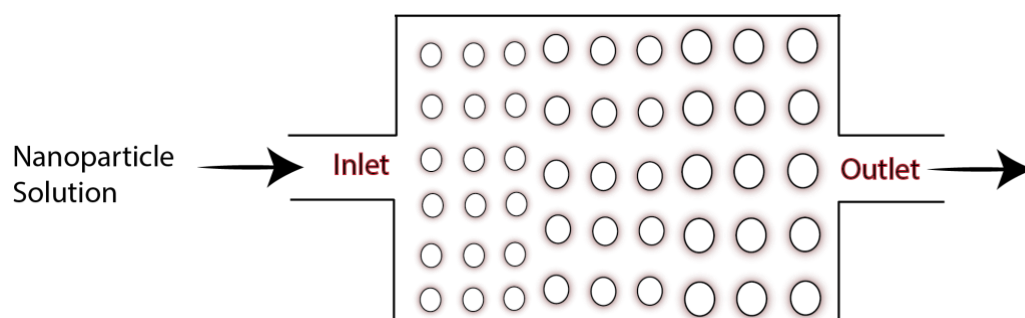


Figure 7.1 Schematic representation of a nanofluidic device for size-based electrostatic trapping of nano-objects. The trapping of nano-objects based on size works as a filter and provides a platform for systematic high-throughput analysis of trapped objects.

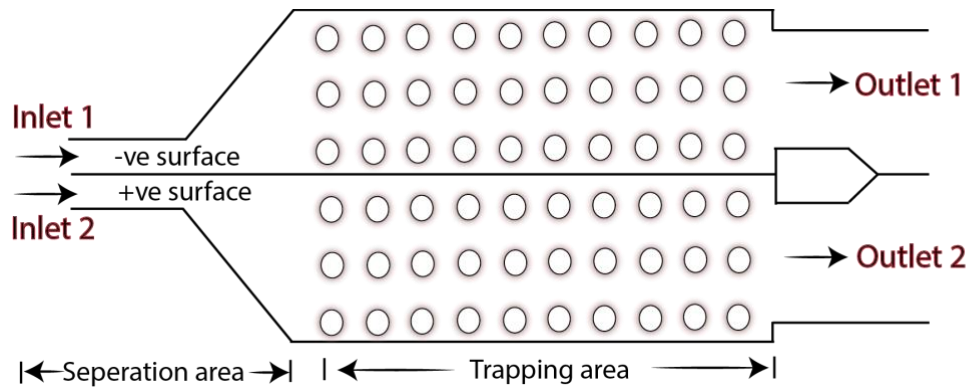


Figure 7.2 Schematic of a nanofluidic device for charge selective electrostatic trapping of nano-objects to trap negatively charged objects in the upper trapping region and positively charged objects in the lower trapping region. The separation area before the trapping area would allow the removal of unlike-charged nano-objects by their adsorption on the device surface in the separation area.

7.2 Conclusions and Prospective Application of Geometrical Trapping

Unlike GIE trapping, geometrical trapping can be used for both charged and uncharged objects in a wide range of aqueous solutions, including body fluids and high salt buffer solutions. Like GIE trapping, geometrical trapping requires an optimized device geometry for effective particle trapping. The geometrical trapping for microscale objects can be obtained using pillars and pockets^{252,287}. However, the same approach cannot be implemented directly for nanofluidic devices to trap nano-objects due to the high surface-to-volume ratio of the device and the nano-objects. The high surface-to-volume ratio of a nanofluidic device leads to increased electrostatic, van der Waals, and capillary forces inside the nanochannel and other nanostructures, resulting in the collapse of nanostructures^{55-57,288,289}. Therefore, this thesis introduces geometrical trapping for nano-objects using nanosteps that allow for size-based nanoparticle trapping at different locations, as shown in Figure 7.3. In order to achieve stable nanostructures and avoid structure collapse, nanopillars were introduced to support the nanosteps and the nanochannel. In the presented device design, micro and nanopillars were combined with nanosteps to achieve effective particle sieving, sorting, and size-based trapping, as shown in Figure 7.4.

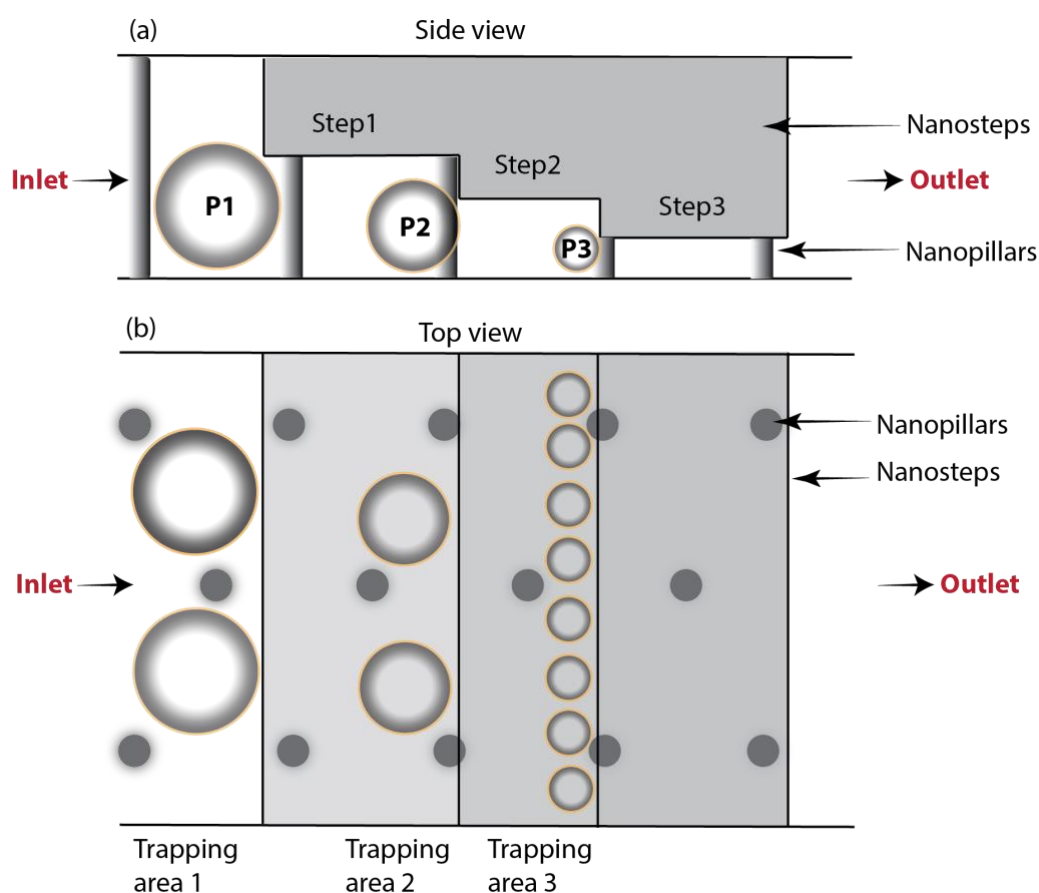


Figure 7.3 Schematic of nanosteps and nanopillars inside a nanochannel in a nanofluidic device for size-selective particle trapping at the location of the nanosteps. Steps 1, 2, and 3 create trapping areas 1, 2, and 3 for trapping particles P1, P2, and P3, respectively. (a) Representation of the side view of the geometrical trapping region inside a nanochannel of a nanofluidic device, and (b) the top view of the nanochannel containing the trapping regions. Nanopillars avoid the collapse of nanochannels and nanosteps and also serve as DLD pillars which can be used as per the requirement of the device for sorting nanoparticles and directing nanoparticles with different diameters in different directions.

The presented device can be used to trap nanoparticles of three different sizes. It can be further optimized based on the particle sizes and the number of different particles needed to be trapped. Since it allows the trapping of same-size particles at the same location, it enhances the detection signal from the particles and, therefore, can be used for the multiplexed detection of molecules adsorbed on the trapped particles at low concentrations (ng/ml to pg/ml) using sensitive detection methods, such as SERS, and LSPR^{267,268}, and fluorescence microscopy^{290,291}.

In order to allow the usage of the fluidic devices for body fluids such as blood, the devices were designed with specifically tailored sections to separate/exclude unwanted macro and micro-sized objects from the main solution before the nano-objects of interest reach the nanochannels. Subsequently, in the nanochannels, nanoparticles are further sorted using DLD pillars to allow particles of different diameters to get trapped at different locations

perpendicular to the flow of the nanochannel (Figure 7.4). This approach can be used for early disease detection and molecular identification by exploiting nanoparticles that could bind the molecules of interest (target) on the particle surface. When a nanoparticle with adsorbed binding molecules is mixed with the main fluid, it allows the binding of the target molecules with the binding molecule on the nanoparticle surface. When multiple of such nanoparticles get trapped at the trapping or detection area, the overall signal from these binding molecule-target molecule complexes gets enhanced. It allows for detecting the target molecules even at a very low concentration. The remaining trapping locations can be used as negative and positive controls by using nanoparticles of different diameters. This device can be further multiplexed for multi-molecule detection.

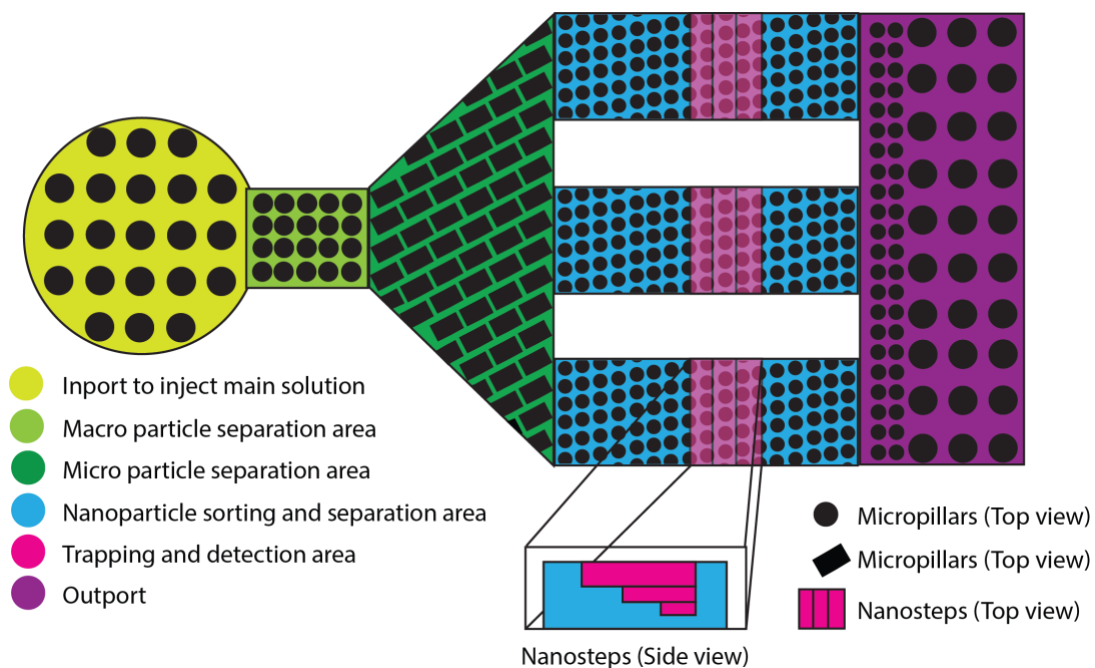


Figure 7.4 Schematic of a nanofluidic device for size-based nanoparticle trapping in addition to the particle separation and sorting from the main solution. The device regions are divided into parts to achieve particle sieving, sorting, and trapping of the target particles in the detection area.

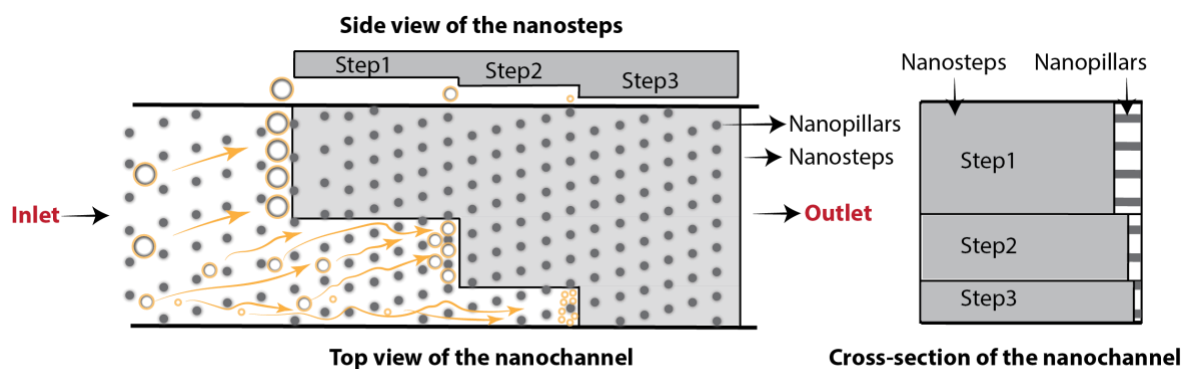


Figure 7.5 Schematic of a nanochannel with the combination of DLD arrays and nanosteps for size-selective nanoparticle sorting and trapping at different locations in the trapping region of the nanochannel.

Furthermore, DLD pillars, combined with nanosteps inside a nanochannel, help trap particles of different sizes at different locations along and perpendicular to the flow of the solution, as shown in Figure 7.5. This combination provides further optimization opportunities to make the detection more effective and location-specific.

Conducted studies in this thesis will help the scientific community to take a step further in the direction of GIE trapping and geometrical trapping and use the presented results for further development and optimization of integrated micro/nanofluidic devices for biological & molecular studies, early disease diagnosis, in-depth study of particle dynamics in the nanoscale and many more.

Bibliography

- 1 Gale, B. *et al.* A Review of Current Methods in Microfluidic Device Fabrication and Future Commercialization Prospects. *Inventions* **3**, doi:10.3390/inventions3030060 (2018).
- 2 Convery, N. & Gadegaard, N. 30 years of microfluidics. *Micro and Nano Engineering* **2**, 76-91, doi:10.1016/j.mne.2019.01.003 (2019).
- 3 Nisisako, T. & Torii, T. Microfluidic large-scale integration on a chip for mass production of monodisperse droplets and particles. *Lab on a Chip* **8**, 287-293, doi:10.1039/b713141k (2008).
- 4 Shang, L., Cheng, Y. & Zhao, Y. Emerging Droplet Microfluidics. *Chem Rev* **117**, 7964-8040, doi:10.1021/acs.chemrev.6b00848 (2017).
- 5 Haneveld, J., Tas, N. R., Brunets, N., Jansen, H. V. & Elwenspoek, M. Capillary filling of sub-10nm nanochannels. *J Appl Phys* **104**, 014309, doi:10.1063/1.2952053 (2008).
- 6 Zhmud, B. V., Tiberg, F. & Hallstenson, K. Dynamics of Capillary Rise. *J Colloid Interface Sci* **228**, 263-269, doi:10.1006/jcis.2000.6951 (2000).
- 7 Martinez, A. W., Phillips, S. T., Butte, M. J. & Whitesides, G. M. Patterned paper as a platform for inexpensive, low-volume, portable bioassays. *Angew Chem Int Ed Engl* **46**, 1318-1320, doi:10.1002/anie.200603817 (2007).
- 8 Reynolds, O. XXIS. An experimental investigation of the circumstances which determine whether the motion of water shall be direct or sinuous, and of the law of resistance in parallel channels. *Phil. Trans. R. Soc.* **174**, 935-982 (1883).
- 9 Manz, A. & Becker, H. *Microsystem Technology in Chemistry and Life Sciences*. (Springer, 1998).
- 10 Mashaghi, S., Abbaspourrad, A., Weitz, D. A. & van Oijen, A. M. Droplet microfluidics: A tool for biology, chemistry and nanotechnology. *TrAC Trends in Analytical Chemistry* **82**, 118-125, doi:10.1016/j.trac.2016.05.019 (2016).
- 11 Hansen, C. L., Skordalakes, E., Berger, J. M. & Quake, S. R. A robust and scalable microfluidic metering method that allows protein crystal growth by free interface diffusion. *Proc Natl Acad Sci U S A* **99**, 16531-16536, doi:10.1073/pnas.262485199 (2002).
- 12 Jafek, A. R., Harbertson, S., Brady, H., Samuel, R. & Gale, B. K. Instrumentation for xPCR Incorporating qPCR and HRMA. *Anal Chem* **90**, 7190-7196, doi:10.1021/acs.analchem.7b05176 (2018).
- 13 Son, J., Samuel, R., Gale, B. K., Carrell, D. T. & Hotaling, J. M. Separation of sperm cells from samples containing high concentrations of white blood cells using a spiral channel. *Biomicrofluidics* **11**, 054106, doi:10.1063/1.4994548 (2017).
- 14 Nivedita, N., Ligrani, P. & Papautsky, I. Dean Flow Dynamics in Low-Aspect Ratio Spiral Microchannels. *Sci Rep* **7**, 44072, doi:10.1038/srep44072 (2017).
- 15 Sweet, R. G. High Frequency Recording with Electrostatically Deflected Ink Jets. *The review of scientific instruments* **36**, 131-136, doi:10.1063/1.1719502 (1965).
- 16 Bassous, E., Taub, H. H. & Kuhn, L. Ink jet printing nozzle arrays etched in silicon. *Applied Physics Letters* **31**, 135-137, doi:10.1063/1.89587 (1977).

- 17 Terry, S. C., Jerman, J. H. & Angell, J. B. A gas chromatographic air analyzer fabricated on a silicon wafer. *IEEE Transactions on Electron Devices* **26**, 1880-1886, doi:10.1109/T-ED.1979.19791 (1979).
- 18 Huff, M. A., Mettner, M. S., Lober, T. A. & Schmidt, M. A. in *IEEE 4th Technical Digest on Solid-State Sensor and Actuator Workshop* 123-127 (Hilton Head Island, SC, USA, 1990).
- 19 Jerman, H. in *IEEE 4th Technical Digest on Solid-State Sensor and Actuator Workshop* 65-69 (IEEE, Hilton Head Island, SC, USA, USA, 1990).
- 20 Tirén, J., Tenerz, L. & Hök, B. A batch-fabricated non-reverse valve with cantilever beam manufactured by micromachining of silicon. *Sensors and Actuators* **18**, 389-396, doi:10.1016/0250-6874(89)87044-1 (1988).
- 21 Ohnstein, T., Fukiura, T., Ridley, J. & Bonne, U. in *IEEE Proceedings on Micro Electro Mechanical Systems, An Investigation of Micro Structures, Sensors, Actuators, Machines and Robots*. 95-98 (IEEE).
- 22 Van Lintel, H. T. G., Van De Pol, F. C. M. & Bouwstra, S. A piezoelectric micropump based on micromachining of silicon. *Sensors and Actuators* **15**, 153-167, doi:10.1016/0250-6874(88)87005-7 (1988).
- 23 Smits, J. G. Piezoelectric micropump with three valves working peristaltically. *Sensors and Actuators A: Physical* **21**, 203-206, doi:10.1016/0924-4247(90)85039-7 (1990).
- 24 Au, A. K., Lai, H., Utela, B. R. & Folch, A. Microvalves and Micropumps for BioMEMS. *Micromachines-Basel* **2**, 179-220, doi:10.3390/mi2020179 (2011).
- 25 Whitesides, G. M. The origins and the future of microfluidics. *Nature* **442**, 368-373, doi:10.1038/nature05058 (2006).
- 26 Manz, A., Graber, N. & Widmer, H. M. Miniaturized Total Chemical Analysis Systems: a Novel Concept for Chemical Sensing. *Sensors and Actuators B: Chemical* **1**, 244-248 (1990).
- 27 Collins, F. S., Morgan, M. & Patrinos, A. The Human Genome Project: Lessons from Large-Scale Biology. *Science* **300**, 286-290 (2003).
- 28 Woolley, A. T. & Mathies, R. A. Ultra-high-speed DNA fragment separations using microfabricated capillary array electrophoresis chips. *P Natl Acad Sci USA* **91**, 11348-11352, doi:10.1073/pnas.91.24.11348 (1994).
- 29 Effenhauser, C. S., Paulus, A., Manz, A. & Widmer, H. M. High-Speed Separation of Antisense Oligonucleotides on a Micromachined Capillary Electrophoresis Device. *Analytical Chemistry* **66**, 2949-2953, doi:10.1021/ac00090a024 (1994).
- 30 Woolley, A. T. & Mathies, R. A. Ultra-High-Speed DNA Sequencing Using Capillary Electrophoresis Chips. *Analytical Chemistry* **67**, 3676-3680, doi:10.1021/ac00116a010 (1995).
- 31 Simpson, P. C. *et al.* High-throughput genetic analysis using microfabricated 96-sample capillary array electrophoresis microplates. *P Natl Acad Sci USA* **95**, 2256-2261 (1998).
- 32 McDonald, J. C. *et al.* Fabrication of microfluidic systems in poly(dimethylsiloxane). *Electrophoresis* **21**, 27-40 (2000).
- 33 Whitesides, G. M., Ostuni, E., Takayama, S., Jiang, X. Y. & Ingber, D. E. Soft lithography in biology and biochemistry. *Annual Review of Biomedical Engineering* **3**, 335-373, doi:DOI 10.1146/annurev.bioeng.3.1.335 (2001).

- 34 McDonald, J. C. & Whitesides, G. M. Poly(dimethylsiloxane) as a material for fabricating microfluidic devices. *Accounts of Chemical Research* **35**, 491-499 (2002).
- 35 McDonald, J. C. *et al.* Prototyping of Microfluidic Devices in Poly(dimethylsiloxane) Using Solid-Object Printing. *Analytical Chemistry* **74**, 1537-1545 (2002).
- 36 Lötters, J. C., Olthuis, W., Veltink, P. H. & Bergveld, P. The mechanical properties of the rubber elastic polymer polydimethylsiloxane for sensor applications. *Journal of Micromechanics and Microengineering* **7**, 145-147 (1997).
- 37 Lee, Y. S., Bhattacharjee, N. & Folch, A. 3D-printed Quake-style microvalves and micropumps. *Lab Chip* **18**, 1207-1214, doi:10.1039/C8LC00001H (2018).
- 38 Unger, M. A., Chou, H.-P., Thorsen, T., Scherer, A. & Quake, S. R. Monolithic Microfabricated Valves and Pumps by Multilayer Soft Lithography. *Science* **288**, 113-116 (2000).
- 39 Sia, S. K. & Whitesides, G. M. Microfluidic devices fabricated in poly(dimethylsiloxane) for biological studies. *Electrophoresis* **24**, 3563-3576, doi:10.1002/elps.200305584 (2003).
- 40 Torino, S., Corrado, B., Iodice, M. & Coppola, G. PDMS-Based Microfluidic Devices for Cell Culture. *Inventions* **3**, doi:10.3390/inventions3030065 (2018).
- 41 Xu, L., Lee, H., Jetta, D. & Oh, K. W. Vacuum-driven power-free microfluidics utilizing the gas solubility or permeability of polydimethylsiloxane (PDMS). *Lab Chip* **15**, 3962-3979, doi:10.1039/c5lc00716j (2015).
- 42 Eddings, M. A. & Gale, B. K. A PDMS-based gas permeation pump for on-chip fluid handling in microfluidic devices. *Journal of Micromechanics and Microengineering* **16**, 2396-2402, doi:10.1088/0960-1317/16/11/021 (2006).
- 43 Ramos, B. L., Choquette, S. J. & Fell, N. F. Embossable Grating Couplers for Planar Waveguide Optical Sensors. *Analytical Chemistry* **68**, 1245-1249 (1996).
- 44 Chou, S. Y., Krauss, P. R. & Renstrom, P. J. Imprint of sub-25 nm vias and trenches in polymers. *Applied Physics Letters* **67**, 3114-3116, doi:10.1063/1.114851 (1995).
- 45 Hansen, T. S., Selmeczi, D. & Larsen, N. B. Fast prototyping of injection molded polymer microfluidic chips. *Journal of Micromechanics and Microengineering* **20**, doi:10.1088/0960-1317/20/1/015020 (2010).
- 46 Kim, D. S., Lee, S. H., Ahn, C. H., Lee, J. Y. & Kwon, T. H. Disposable integrated microfluidic biochip for blood typing by plastic microinjection moulding. *Lab Chip* **6**, 794-802, doi:10.1039/b516495h (2006).
- 47 Kim, P. *et al.* Soft Lithography for Microfluidics: a Review. *Biochip J* **2**, 1-11 (2008).
- 48 Christopher Love, J., Wolfe, D. & Whitesides, G. in *Dekker Encyclopedia of Nanoscience and Nanotechnology - Six Volume Set (Print Version)* (CRC Press, 2004).
- 49 Kim, D.-H. *et al.* Guided three-dimensional growth of functional cardiomyocytes on polyethylene glycol nanostructures. *Langmuir* **22**, 5419-5426 (2006).
- 50 Weerakoon-Ratnayake, K. M., O'Neil, C. E., Uba, F. I. & Soper, S. A. Thermoplastic nanofluidic devices for biomedical applications. *Lab on a Chip* **17**, 362-381, doi:10.1039/c6lc01173j (2017).
- 51 Abgrall, P. & Nguyen, N. T. Nanofluidic devices and their applications. *Analytical Chemistry* **80**, 2326-2341, doi:10.1021/ac702296u (2008).

- 52 Eijkel, J. C. T. & Berg, A. v. d. Nanofluidics: what is it and what can we expect from it? *Microfluid Nanofluid* **1**, 249-267, doi:10.1007/s10404-004-0012-9 (2005).
- 53 Sparreboom, W., van den Berg, A. & Eijkel, J. C. Principles and applications of nanofluidic transport. *Nat Nanotechnol* **4**, 713-720, doi:10.1038/nnano.2009.332 (2009).
- 54 Schoch, R. B., Han, J. & Renaud, P. Transport phenomena in nanofluidics. *Reviews of Modern Physics* **80**, 839-883, doi:10.1103/RevModPhys.80.839 (2008).
- 55 Gad-el-Hak, M. The fluid mechanics of microdevices - The Freeman Scholar Lecture. *J Fluid Eng-T Asme* **121**, 5-33, doi:Doi 10.1115/1.2822013 (1999).
- 56 Conlisk, A. T. The Debye-Huckel approximation: Its use in describing electroosmotic flow in micro- and nanochannels. *Electrophoresis* **26**, 1896-1912, doi:10.1002/elps.200410238 (2005).
- 57 Haywood, D. G., Saha-Shah, A., Baker, L. A. & Jacobson, S. C. Fundamental studies of nanofluidics: nanopores, nanochannels, and nanopipets. *Anal Chem* **87**, 172-187, doi:10.1021/ac504180h (2015).
- 58 Kim, S. J., Wang, Y. C., Lee, J. H., Jang, H. & Han, J. Concentration polarization and nonlinear electrokinetic flow near a nanofluidic channel. *Phys Rev Lett* **99**, 044501, doi:10.1103/PhysRevLett.99.044501 (2007).
- 59 Mani, A., Zangle, T. A. & Santiago, J. G. On the Propagation of Concentration Polarization from Microchannel-Nanochannel Interfaces Part I: Analytical Model and Characteristic Analysis. *Langmuir* **25**, 3898-3908, doi:10.1021/1a803317p (2009).
- 60 Zangle, T. A., Mani, A. & Santiago, J. G. On the Propagation of Concentration Polarization from Microchannel-Nanochannel Interfaces Part II: Numerical and Experimental Study. *Langmuir* **25**, 3909-3916, doi:10.1021/la803318e (2009).
- 61 Son, S. Y., Lee, S., Lee, H. & Kim, S. J. Engineered nanofluidic preconcentration devices by ion concentration polarization. *Biochip J* **10**, 251-261, doi:10.1007/s13206-016-0401-7 (2016).
- 62 Kim, S. J., Song, Y. A. & Han, J. Nanofluidic concentration devices for biomolecules utilizing ion concentration polarization: theory, fabrication, and applications. *Chem Soc Rev* **39**, 912-922, doi:10.1039/b822556g (2010).
- 63 van Honschoten, J. W., Brunets, N. & Tas, N. R. Capillarity at the nanoscale. *Chem Soc Rev* **39**, 1096-1114, doi:10.1039/b909101g (2010).
- 64 Tas, N. R., Mela, P., Kramer, T., Berenschot, J. W. & van den Berg, A. Capillarity induced negative pressure of water plugs in nanochannels. *Nano Letters* **3**, 1537-1540, doi:10.1021/nl034676e (2003).
- 65 Piruska, A., Gong, M., Sweedler, J. V. & Bohn, P. W. Nanofluidics in chemical analysis. *Chem Soc Rev* **39**, 1060-1072, doi:10.1039/b900409m (2010).
- 66 Pu, Q. S., Yun, J. S., Temkin, H. & Liu, S. R. Ion-enrichment and ion-depletion effect of nanochannel structures. *Nano Letters* **4**, 1099-1103, doi:10.1021/nl0494811 (2004).
- 67 Oh, J. M., Faez, T., de Beer, S. & Mugele, F. Capillarity-driven dynamics of water-alcohol mixtures in nanofluidic channels. *Microfluid Nanofluid* **9**, 123-129, doi:10.1007/s10404-009-0517-3 (2009).

- 68 Hwang, J. & Daiguji, H. Ion Transport in Sub-10 nm Nanofluidic Channels: Synthesis, Measurement, and Modeling. *Isr J Chem* **54**, 1509-1518, doi:10.1002/ijch.201400088 (2014).
- 69 Zhou, G. Y. *et al.* Bioinspired Micro/Nanofluidic Ion Transport Channels for Organic Cathodes in High-Rate and Ultrastable Lithium/Sodium-Ion Batteries. *Adv Funct Mater* **28**, doi:10.1002/adfm.201804629 (2018).
- 70 Daiguji, H. Ion transport in nanofluidic channels. *Chemical Society Reviews* **39**, 901-911, doi:10.1039/b820556f (2010).
- 71 Persson, F. & Tegenfeldt, J. O. DNA in nanochannels--directly visualizing genomic information. *Chem Soc Rev* **39**, 985-999, doi:10.1039/b912918a (2010).
- 72 Levy, S. L. & Craighead, H. G. DNA manipulation, sorting, and mapping in nanofluidic systems. *Chem Soc Rev* **39**, 1133-1152, doi:10.1039/b820266b (2010).
- 73 Han, J. & Craighead, H. G. Separation of long DNA molecules in a microfabricated entropic trap array. *Science* **288**, 1026-1029, doi:DOI 10.1126/science.288.5468.1026 (2000).
- 74 Zangle, T. A., Mani, A. & Santiago, J. G. Theory and experiments of concentration polarization and ion focusing at microchannel and nanochannel interfaces. *Chem Soc Rev* **39**, 1014-1035, doi:10.1039/b902074h (2010).
- 75 Wu, D. & Steckl, A. J. High speed nanofluidic protein accumulator. *Lab Chip* **9**, 1890-1896, doi:10.1039/b823409d (2009).
- 76 Frykholm, K., Nyberg, L. K. & Westerlund, F. Exploring DNA-protein interactions on the single DNA molecule level using nanofluidic tools. *Integr Biol (Camb)* **9**, 650-661, doi:10.1039/c7ib00085e (2017).
- 77 Oz, R., Kk, S. & Westerlund, F. A nanofluidic device for real-time visualization of DNA-protein interactions on the single DNA molecule level. *Nanoscale* **11**, 2071-2078, doi:10.1039/c8nr09023h (2019).
- 78 Lenshof, A. & Laurell, T. Continuous separation of cells and particles in microfluidic systems. *Chem Soc Rev* **39**, 1203-1217, doi:10.1039/b915999c (2010).
- 79 Sajeesh, P. & Sen, A. K. Particle separation and sorting in microfluidic devices: a review. *Microfluid Nanofluid* **17**, 1-52, doi:10.1007/s10404-013-1291-9 (2014).
- 80 Yanai, T., Ouchi, T., Yamada, M. & Seki, M. Hydrodynamic Microparticle Separation Mechanism Using Three-Dimensional Flow Profiles in Dual-Depth and Asymmetric Lattice-Shaped Microchannel Networks. *Micromachines (Basel)* **10**, doi:10.3390/mi10060425 (2019).
- 81 Tetala, K. K. R. & Vijayalakshmi, M. A. A review on recent developments for biomolecule separation at analytical scale using microfluidic devices. *Anal Chim Acta* **906**, 7-21, doi:10.1016/j.aca.2015.11.037 (2016).
- 82 Fringes, S., Holzner, F. & Knoll, A. W. The nanofluidic confinement apparatus: studying confinement-dependent nanoparticle behavior and diffusion. *Beilstein J Nanotechnol* **9**, 301-310, doi:10.3762/bjnano.9.30 (2018).
- 83 Loucaides, N. G., Ramos, A. & Georgiou, G. E. Trapping and manipulation of nanoparticles by using jointly dielectrophoresis and AC electroosmosis. *Journal of Physics: Conference Series* **100**, 052015, doi:10.1088/1742-6596/100/5/052015 (2008).

- 84 Gerspach, M. A., Mojarad, N., Sharma, D., Ekinci, Y. & Pfohl, T. Pneumatically Controlled Nanofluidic Devices for Contact-Free Trapping and Manipulation of Nanoparticles. *Particle & Particle Systems Characterization* **35**, doi:10.1002/ppsc.201800161 (2018).
- 85 Sharma, D., Gerspach, M. A., Pfohl, T., Lim, R. Y. H. & Ekinci, Y. Single positively charged particle trapping in nanofluidic systems. *Microelectronic Engineering* **175**, 43-49, doi:10.1016/j.mee.2017.01.001 (2017).
- 86 Kang, D.-K., Monsur Ali, M., Zhang, K., Pone, E. J. & Zhao, W. Droplet microfluidics for single-molecule and single-cell analysis in cancer research, diagnosis and therapy. *TrAC Trends in Analytical Chemistry* **58**, 145-153, doi:10.1016/j.trac.2014.03.006 (2014).
- 87 Prickril, B. & Rasooly, A. *Biosensors and Biodetection*. (Humana Press, New York, NY, 2017).
- 88 Rems, L., Kawale, D., Lee, L. J. & Boukany, P. E. Flow of DNA in micro/nanofluidics: From fundamentals to applications. *Biomicrofluidics* **10**, 043403, doi:10.1063/1.4958719 (2016).
- 89 Mikkelsen, M. B., Reisner, W., Flyvbjerg, H. & Kristensen, A. Pressure-driven DNA in nanogroove arrays: complex dynamics leads to length- and topology-dependent separation. *Nano Lett* **11**, 1598-1602, doi:10.1021/nl1044764 (2011).
- 90 Lin, P. K. *et al.* Static conformation and dynamics of single DNA molecules confined in nanoslits. *Phys Rev E Stat Nonlin Soft Matter Phys* **76**, 011806, doi:10.1103/PhysRevE.76.011806 (2007).
- 91 Reisner, W., Pedersen, J. N. & Austin, R. H. DNA confinement in nanochannels: physics and biological applications. *Rep Prog Phys* **75**, 106601, doi:10.1088/0034-4885/75/10/106601 (2012).
- 92 Friedrich, R. *et al.* A nano flow cytometer for single lipid vesicle analysis. *Lab Chip* **17**, 830-841, doi:10.1039/c6lc01302c (2017).
- 93 Vallejo, D., Lee, S.-H. & Lee, A. in *Biosensors and Biodetection Methods in Molecular Biology* (eds B. Prickril & A. Rasooly) 489-510 (Humana Press, New York, NY, 2017).
- 94 Celebrano, M., Rosman, C., Sonnichsen, C. & Krishnan, M. Angular trapping of anisometric nano-objects in a fluid. *Nano Lett* **12**, 5791-5796, doi:10.1021/nl303099c (2012).
- 95 Rodriguez-Ruiz, I., Babenko, V., Martinez-Rodriguez, S. & Gavira, J. A. Protein separation under a microfluidic regime. *Analyst* **143**, 606-619, doi:10.1039/c7an01568b (2018).
- 96 Lee, W. G., Kim, Y. G., Chung, B. G., Demirci, U. & Khademhosseini, A. Nano/Microfluidics for diagnosis of infectious diseases in developing countries. *Adv Drug Deliv Rev* **62**, 449-457, doi:10.1016/j.addr.2009.11.016 (2010).
- 97 Rosen, Y. & Gurman, P. in *Encyclopedia of Nanotechnology* (ed Bharat Bhushan) 1375-1375 (Springer Netherlands, 2012).
- 98 Sanjay, S. T. *et al.* Biomarker detection for disease diagnosis using cost-effective microfluidic platforms. *Analyst* **140**, 7062-7081, doi:10.1039/c5an00780a (2015).
- 99 Wu, J., Dong, M., Rigatto, C., Liu, Y. & Lin, F. Lab-on-chip technology for chronic disease diagnosis. *NPJ Digit Med* **1**, 7, doi:10.1038/s41746-017-0014-0 (2018).

- 100 Thorsen, T., Maerkl, S. J. & Quake, S. R. Microfluidic large-scale integration. *Science* **298**, 580-584, doi:10.1126/science.1076996 (2002).
- 101 Araci, I. E. & Brisk, P. Recent developments in microfluidic large scale integration. *Curr Opin Biotech* **25**, 60-68, doi:10.1016/j.copbio.2013.08.014 (2014).
- 102 Freitas, D. N., Mongersun, A., Chau, H. & Araci, I. E. Tunable soft lithography molds enable rapid-prototyping of multi-height channels for microfluidic large-scale integration. *Journal of Micromechanics and Microengineering* **29**, doi:10.1088/1361-6439/aafd9c (2019).
- 103 Gokce, O., Mercandetti, C. & Delamarche, E. High-Content Optical Codes for Protecting Rapid Diagnostic Tests from Counterfeiting. *Anal Chem* **90**, 7383-7390, doi:10.1021/acs.analchem.8b00826 (2018).
- 104 Jebrail, M. J. *et al.* Digital microfluidics for automated proteomic processing. *J Vis Exp*, doi:10.3791/1603 (2009).
- 105 Freire, S. L. S. Perspectives on digital microfluidics. *Sensors and Actuators A: Physical* **250**, 15-28, doi:10.1016/j.sna.2016.08.007 (2016).
- 106 Pungetmongkol, P. & Yamamoto, T. Single-Molecule Detection of DNA in a Nanochannel by High-Field Strength-Assisted Electrical Impedance Spectroscopy. *Micromachines (Basel)* **10**, doi:10.3390/mi10030189 (2019).
- 107 Cipriany, B. R. *et al.* Single molecule epigenetic analysis in a nanofluidic channel. *Anal Chem* **82**, 2480-2487, doi:10.1021/ac9028642 (2010).
- 108 Li, D. in *Encyclopedia of Microfluidics and Nanofluidics* Ch. Chapter 1091-3, 1-8 (2014).
- 109 Krishnan, M. Electrostatic free energy for a confined nanoscale object in a fluid. *J Chem Phys* **138**, 114906, doi:10.1063/1.4795087 (2013).
- 110 Mojarad, N. & Krishnan, M. Measuring the size and charge of single nanoscale objects in solution using an electrostatic fluidic trap. *Nat Nanotechnol* **7**, 448-452, doi:10.1038/nnano.2012.99 (2012).
- 111 Mojarad, N., Sandoghdar, V. & Krishnan, M. Measuring three-dimensional interaction potentials using optical interference. *Opt Express* **21**, 9377-9389, doi:10.1364/OE.21.009377 (2013).
- 112 Krishnan, M., Mojarad, N., Kukura, P. & Sandoghdar, V. Geometry-induced electrostatic trapping of nanometric objects in a fluid. *Nature* **467**, 692-695, doi:10.1038/nature09404 (2010).
- 113 Gerspach, M. A., Mojarad, N., Pfohl, T. & Ekinici, Y. Glass-based geometry-induced electrostatic trapping devices for improved scattering contrast imaging of nano-objects. *Microelectronic Engineering* **145**, 43-48, doi:10.1016/j.mee.2015.02.035 (2015).
- 114 Kirby, B. J. & Hasselbrink, E. F. Zeta potential of microfluidic substrates: 1. Theory, experimental techniques, and effects on separations. *Electrophoresis* **25**, 187-202, doi:10.1002/elps.200305754 (2004).
- 115 Behrens, S. H. & Grier, D. G. The charge of glass and silica surfaces. *Journal of Chemical Physics* **115**, 6716-6721, doi:Doi 10.1063/1.1404988 (2001).
- 116 Holt, P. F. & King, D. T. The Chemistry of Silica Surfaces. *J Chem Soc*, 773-779, doi:DOI 10.1039/jr9550000773 (1955).

- 117 Iler, R. K. *The Chemistry of Silica*. (John Wiley & Sons, 1979).
- 118 Zhuravlev, L. T. Concentration of Hydroxyl-Groups on the Surface of Amorphous Silicas. *Langmuir* **3**, 316-318, doi:DOI 10.1021/la00075a004 (1987).
- 119 Lowe, B. M., Skylaris, C. K. & Green, N. G. Acid-base dissociation mechanisms and energetics at the silica-water interface: An activationless process. *J Colloid Interface Sci* **451**, 231-244, doi:10.1016/j.jcis.2015.01.094 (2015).
- 120 Ashkin, A., Dziedzic, J. M., Bjorkholm, J. E. & Chu, S. Observation of a Single-Beam Gradient Force Optical Trap for Dielectric Particles. *Optics Letters* **11**, 288-290, doi:Doi 10.1364/Ol.11.000288 (1986).
- 121 Juan, M. L., Righini, M. & Quidant, R. Plasmon nano-optical tweezers. *Nature Photonics* **5**, 349-356, doi:10.1038/nphoton.2011.56 (2011).
- 122 Taylor, R. W. & Sandoghdar, V. Interferometric Scattering Microscopy: Seeing Single Nanoparticles and Molecules via Rayleigh Scattering. *Nano Lett* **19**, 4827-4835, doi:10.1021/acs.nanolett.9b01822 (2019).
- 123 Ortega-Arroyo, J. & Kukura, P. Interferometric scattering microscopy (iSCAT): new frontiers in ultrafast and ultrasensitive optical microscopy. *Phys Chem Chem Phys* **14**, 15625-15636, doi:10.1039/c2cp41013c (2012).
- 124 Andrecka, J. *et al.* in *Methods in Enzymology* (Academic Press, 2016).
- 125 Gerspach, M. A., Mojarad, N., Sharma, D., Pfohl, T. & Ekinici, Y. Soft electrostatic trapping in nanofluidics. *Microsystems & Nanoengineering* **3**, 17051, doi:10.1038/micronano.2017.51 (2017).
- 126 Lindfors, K., Kalkbrenner, T., Stoller, P. & Sandoghdar, V. Detection and spectroscopy of gold nanoparticles using supercontinuum white light confocal microscopy. *Phys Rev Lett* **93**, 037401, doi:10.1103/PhysRevLett.93.037401 (2004).
- 127 Kusumi, A., Sako, Y. & Yamamoto, M. Confined Lateral Diffusion of Membrane-Receptors as Studied by Single-Particle Tracking (Nanovid Microscopy) - Effects of Calcium-Induced Differentiation in Cultured Epithelial-Cells. *Biophysical Journal* **65**, 2021-2040 (1993).
- 128 Islam, M. A. Einstein–Smoluchowski Diffusion Equation: A Discussion. *Physica Scripta* **70**, 6 (2004).
- 129 Kramers, H. A. Brownian motion in a field of force and the diffusion model of chemical reactions. *Physica* **7**, 284-360 (1940).
- 130 Carey, G. F. & Martin, H. C. *Introduction to Finite Element Analysis: Theory and Application*. (1973).
- 131 Hilderbrand, F. B. *Advanced Calculus for Applications*. (1962).
- 132 Fletcher, C. A. J. *The Galerkin Method: An Introduction, Numerical Simulation of Fluid Motion*. (1978).
- 133 Chari, M. V. K. & Salon, S. J. *Numerical Methods in Electromagnetism*. (2000).
- 134 Zeming, K. K., Thakor, N. V., Zhang, Y. & Chen, C. H. Real-time modulated nanoparticle separation with an ultra-large dynamic range. *Lab on a Chip* **16**, 75-85, doi:10.1039/c5lc01051a (2016).
- 135 Huang, L. R., Cox, E. C., Austin, R. H. & Sturm, J. C. Continuous particle separation through deterministic lateral displacement. *Science* **304**, 987-990, doi:DOI 10.1126/science.1094567 (2004).

- 136 Liu, Z. *et al.* Rapid isolation of cancer cells using microfluidic deterministic lateral displacement structure. *Biomicrofluidics* **7**, 11801, doi:10.1063/1.4774308 (2013).
- 137 Wei, J. *et al.* Numerical Study of Pillar Shapes in Deterministic Lateral Displacement Microfluidic Arrays for Spherical Particle Separation. *IEEE Trans Nanobioscience* **14**, 660-667, doi:10.1109/TNB.2015.2431855 (2015).
- 138 Morton, K. J. *et al.* Crossing microfluidic streamlines to lyse, label and wash cells. *Lab Chip* **8**, 1448-1453, doi:10.1039/b805614e (2008).
- 139 Inglis, D. W., Davis, J. A., Austin, R. H. & Sturm, J. C. Critical particle size for fractionation by deterministic lateral displacement. *Lab Chip* **6**, 655-658, doi:10.1039/b515371a (2006).
- 140 Zeming, K. K., Salafi, T., Chen, C. H. & Zhang, Y. Asymmetrical Deterministic Lateral Displacement Gaps for Dual Functions of Enhanced Separation and Throughput of Red Blood Cells. *Sci Rep* **6**, 22934, doi:10.1038/srep22934 (2016).
- 141 Ranjan, S., Zeming, K. K., Jureen, R., Fisher, D. & Zhang, Y. DLD pillar shape design for efficient separation of spherical and non-spherical bioparticles. *Lab Chip* **14**, 4250-4262, doi:10.1039/c4lc00578c (2014).
- 142 Chan, J., Fore, S., Wachsmann-Hogiu, S. & Huser, T. Raman spectroscopy and microscopy of individual cells and cellular components. *Laser & Photonics Review* **2**, 325-349, doi:10.1002/lpor.200810012 (2008).
- 143 Pahlow, S. *et al.* Isolation and identification of bacteria by means of Raman spectroscopy. *Adv Drug Deliv Rev* **89**, 105-120, doi:10.1016/j.addr.2015.04.006 (2015).
- 144 Katz, O., Levitt, M. J., Grinvald, E. & Silberberg, Y. Single-beam coherent Raman spectroscopy and microscopy via spectral notch shaping. *Optics Express* **18**, 22693 - 22701 (2010).
- 145 Hayazawa, N. *et al.* Visualization of localized strain of a crystalline thin layer at the nanoscale by tip-enhanced Raman spectroscopy and microscopy. *Journal of Raman Spectroscopy* **38**, 684-696, doi:10.1002/jrs.1728 (2007).
- 146 Berto, P., Andresen, E. R. & Rigneault, H. Background-free stimulated Raman spectroscopy and microscopy. *Phys Rev Lett* **112**, 053905, doi:10.1103/PhysRevLett.112.053905 (2014).
- 147 Kneipp, J., Kneipp, H. & Kneipp, K. Two-photon vibrational spectroscopy for biosciences based on surface-enhanced hyper-Raman scattering. *Proc Natl Acad Sci U S A* **103**, 17149-17153, doi:10.1073/pnas.0608262103 (2006).
- 148 Spiro, T. G. Resonance Raman Spectroscopy: a New Structure Probe for Biological Chromophores. *Accounts of Chemical Research* **7** (1974).
- 149 Diem, M., Romeo, M., Boydston-White, S., Miljkovic, M. & Matthaus, C. A decade of vibrational micro-spectroscopy of human cells and tissue (1994-2004). *Analyst* **129**, 880-885, doi:10.1039/b408952a (2004).
- 150 Laing, S., Jamieson, L. E., Faulds, K. & Graham, D. Surface-enhanced Raman spectroscopy for in vivo biosensing. *Nature Reviews Chemistry* **1**, doi:10.1038/s41570-017-0060 (2017).

- 151 Shan, B., Pu, Y., Chen, Y., Liao, M. & Li, M. Novel SERS labels: Rational design, functional integration and biomedical applications. *Coordination Chemistry Reviews* **371**, 11-37, doi:10.1016/j.ccr.2018.05.007 (2018).
- 152 Fleischmann, M., Hendra, P. J. & McQuillan, A. J. Raman spectra of pyridine adsorbed at a silver electrode. *Chemical Physics Letters* **26**, 163-166 (1974).
- 153 Jeanmaire, D. L. & Van Duyne, R. P. Surface raman spectroelectrochemistry: Part I. Heterocyclic, aromatic, and aliphatic amines adsorbed on the anodized silver electrode. *Journal of Electroanalytical Chemistry and Interfacial Electrochemistry* **84**, 1-20 (1977).
- 154 Baddour-Hadjean, R. & Pereira-Ramos, J.-P. Raman Microspectrometry Applied to the Study of Electrode Materials for Lithium Batteries. *Chemical Reviews* **110**, 1278-1319 (2010).
- 155 Atkins, P., de Paula, J. & Friedman, R. *Physical Chemistry: Quanta, Matter and Change*. Second edn, (Oxford University Press, 2013).
- 156 Gillibert, R., Huang, J. Q., Zhang, Y., Fu, W. L. & Lamy de la Chapelle, M. Explosive detection by Surface Enhanced Raman Scattering. *TrAC Trends in Analytical Chemistry* **105**, 166-172, doi:10.1016/j.trac.2018.03.018 (2018).
- 157 Guillot, N. & de la Chapelle, M. L. The electromagnetic effect in surface enhanced Raman scattering: Enhancement optimization using precisely controlled nanostructures. *Journal of Quantitative Spectroscopy and Radiative Transfer* **113**, 2321-2333, doi:10.1016/j.jqsrt.2012.04.025 (2012).
- 158 Champion, A. & Kambhampati, P. Surface-enhanced Raman scattering. *Chemical Society Reviews* **27**, 241-250 (1998).
- 159 Strommen, D. P. & Nakamoto, K. Resonance Raman Spectroscopy. *J Chem Educ* **54** (1977).
- 160 Wu, D.-Y. *et al.* Chemical Enhancement Effects in SERS Spectra: A Quantum Chemical Study of Pyridine Interacting with Copper, Silver, Gold and Platinum Metals. *J Phys Chem C* **112**, 4195-4204 (2008).
- 161 Su, K.-H., Wei, Q.-H. & Zhang, X. Interparticle Coupling Effect on Plasmon Resonances of Nanogold Particles. *Nano Letters* **3**, 1087-1090 (2003).
- 162 Grand, J. *et al.* Role of localized surface plasmons in surface-enhanced Raman scattering of shape-controlled metallic particles in regular arrays. *Phys Rev B* **72**, doi:10.1103/PhysRevB.72.033407 (2005).
- 163 Tian, F., Bonnier, F., Casey, A., Shanahan, A. E. & Byrne, H. J. Surface enhanced Raman scattering with gold nanoparticles: effect of particle shape. *Anal. Methods* **6**, 9116-9123, doi:10.1039/c4ay02112f (2014).
- 164 Moskovits, M. Persistent misconceptions regarding SERS. *Phys Chem Chem Phys* **15**, 5301-5311, doi:10.1039/c2cp44030j (2013).
- 165 Aravind, P. K., Nitzan, A. & Metiu, H. The interaction between electromagnetic resonances and its role in spectroscopic studies of molecules adsorbed on colloidal particles or metal spheres. *Surface Science* **110**, 189-204, doi:[https://doi.org/10.1016/0039-6028\(81\)90595-1](https://doi.org/10.1016/0039-6028(81)90595-1) (1981).

- 166 Fang, Y., Seong, N.-H. & Dlott, D. D. Measurement of the Distribution of Site Enhancements in Surface-Enhanced Raman Scattering. *Science* **321**, 388-392, doi:10.1126/science.1159499 (2008).
- 167 Aroca, R. F., Alvarez-Puebla, R. A., Pieczonka, N., Sanchez-Cortez, S. & Garcia-Ramos, J. V. Surface-enhanced Raman scattering on colloidal nanostructures. *Adv Colloid Interface Sci* **116**, 45-61, doi:10.1016/j.cis.2005.04.007 (2005).
- 168 Ouyang, L., Zhu, L., Jiang, J. & Tang, H. A surface-enhanced Raman scattering method for detection of trace glutathione on the basis of immobilized silver nanoparticles and crystal violet probe. *Anal Chim Acta* **816**, 41-49, doi:10.1016/j.aca.2014.01.046 (2014).
- 169 Rodriguez-Lorenzo, L., Fabris, L. & Alvarez-Puebla, R. A. Multiplex optical sensing with surface-enhanced Raman scattering: a critical review. *Anal Chim Acta* **745**, 10-23, doi:10.1016/j.aca.2012.08.003 (2012).
- 170 Wang, Z. *et al.* SERS-based multiplex immunoassay of tumor markers using double SiO₂@Ag immune probes and gold-film hemisphere array immune substrate. *Colloids and Surfaces A: Physicochemical and Engineering Aspects* **546**, 48-58, doi:10.1016/j.colsurfa.2018.02.069 (2018).
- 171 Balzerová, A., Opletalová, A., Ranc, V. & Zbořil, R. Multiplex competitive analysis of HER2 and EpCAM cancer markers in whole human blood using Fe₂O₃@Ag nanocomposite. *Applied Materials Today* **13**, 166-173, doi:10.1016/j.apmt.2018.08.016 (2018).
- 172 Ravindranath, S. P., Wang, Y. & Irudayaraj, J. SERS driven cross-platform based multiplex pathogen detection. *Sensors and Actuators B: Chemical* **152**, 183-190, doi:10.1016/j.snb.2010.12.005 (2011).
- 173 Zheng, X. S., Jahn, I. J., Weber, K., Cialla-May, D. & Popp, J. Label-free SERS in biological and biomedical applications: Recent progress, current challenges and opportunities. *Spectrochim Acta A Mol Biomol Spectrosc* **197**, 56-77, doi:10.1016/j.saa.2018.01.063 (2018).
- 174 Li, X. *et al.* A SERS nano-tag-based fiber-optic strategy for in situ immunoassay in unprocessed whole blood. *Biosens Bioelectron* **92**, 517-522, doi:10.1016/j.bios.2016.10.070 (2017).
- 175 Grier, D. G. A revolution in optical manipulation. *Nature* **424**, 810-816, doi:10.1038/nature01935 (2003).
- 176 Ashkin, A. & Dziedzic, J. M. Optical Trapping and Manipulation of Viruses and Bacteria. *Science* **235**, 1517-1520, doi:DOI 10.1126/science.3547653 (1987).
- 177 Gosse, C. & Croquette, V. Magnetic tweezers: Micromanipulation and force measurement at the molecular level. *Biophysical Journal* **82**, 3314-3329 (2002).
- 178 Bausch, A. R., Moller, W. & Sackmann, E. Measurement of local viscoelasticity and forces in living cells by magnetic tweezers. *Biophysical Journal* **76**, 573-579 (1999).
- 179 Shi, J. J. *et al.* Acoustic tweezers: patterning cells and microparticles using standing surface acoustic waves (SSAW). *Lab on a Chip* **9**, 2890-2895, doi:10.1039/b910595f (2009).
- 180 Courtney, C. R. P. *et al.* Independent trapping and manipulation of microparticles using dexterous acoustic tweezers. *Applied Physics Letters* **104**, doi:10.1063/1.4870489 (2014).

- 181 Nilsson, J., Evander, M., Hammarstrom, B. & Laurell, T. Review of cell and particle trapping in microfluidic systems. *Anal Chim Acta* **649**, 141-157, doi:10.1016/j.aca.2009.07.017 (2009).
- 182 Neuman, K. C. & Nagy, A. Single-molecule force spectroscopy: optical tweezers, magnetic tweezers and atomic force microscopy. *Nature Methods* **5**, 491-505, doi:10.1038/Nmeth.1218 (2008).
- 183 Hansen, P. M., Bhatia, V. K., Harrit, N. & Oddershede, L. Expanding the optical trapping range of gold nanoparticles. *Nano Lett* **5**, 1937-1942, doi:10.1021/nl051289r (2005).
- 184 Ashkin, A., Dziedzic, J. M. & Yamane, T. Optical trapping and manipulation of single cells using infrared laser beams. *Nature* **330**, 769-771, doi:10.1038/330769a0 (1987).
- 185 Moffitt, J. R., Chemla, Y. R., Smith, S. B. & Bustamante, C. Recent advances in optical tweezers. *Annu Rev Biochem* **77**, 205-228, doi:10.1146/annurev.biochem.77.043007.090225 (2008).
- 186 Moffitt, J. R., Chemla, Y. R., Izhaky, D. & Bustamante, C. Differential detection of dual traps improves the spatial resolution of optical tweezers. *P Natl Acad Sci USA* **103**, 9006-9011, doi:10.1073/pnas.0603342103 (2006).
- 187 Abbondanzieri, E. A., Greenleaf, W. J., Shaevitz, J. W., Landick, R. & Block, S. M. Direct observation of base-pair stepping by RNA polymerase. *Nature* **438**, 460-465, doi:10.1038/nature04268 (2005).
- 188 Myers, C. J., Celebrano, M. & Krishnan, M. Information storage and retrieval in a single levitating colloidal particle. *Nat Nanotechnol* **10**, 886-891, doi:10.1038/nnano.2015.173 (2015).
- 189 Pham, P., Howorth, M., Planat-Chrétien, A. & Tardu, S. Numerical Simulation of the Electric Double Layer Based on the Poisson-Boltzmann Models for AC Electroosmosis Flows. *COMSOL Users Conf. 2007, Grenoble* (2007).
- 190 Stoller, P., Jacobsen, V. & Sandoghdar, V. Measurement of the complex dielectric constant of a single gold nanoparticle. *Optics Letters* **31**, 2474-2476, doi:10.1364/Ol.31.002474 (2006).
- 191 Kukura, P. *et al.* High-speed nanoscopic tracking of the position and orientation of a single virus. *Nat Methods* **6**, 923-927, doi:10.1038/nmeth.1395 (2009).
- 192 Andrecka, J. *et al.* in *Methods in Enzymology* (Academic Press).
- 193 Mao, P. & Han, J. Y. Fabrication and characterization of 20 nm planar nanofluidic channels by glass-glass and glass-silicon bonding. *Lab on a Chip* **5**, 837-844, doi:10.1039/b502809d (2005).
- 194 Decher, G. Fuzzy nanoassemblies: Toward layered polymeric multicomposites. *Science* **277**, 1232-1237, doi:10.1126/science.277.5330.1232 (1997).
- 195 Dootz, R., Nie, J. J., Du, B. Y., Herminghaus, S. & Pfohl, T. Raman and surface enhanced Raman microscopy of microstructured polyethylenimine/DNA multilayers. *Langmuir* **22**, 1735-1741, doi:10.1021/la052739y (2006).
- 196 Pappaert, K., Biesemans, J., Clicq, D., Vankrunkelsven, S. & Desmet, G. Measurements of diffusion coefficients in 1-D micro- and nanochannels using shear-driven flows. *Lab on a Chip* **5**, 1104-1110, doi:10.1039/b505122c (2005).

- 197 Savin, T. & Doyle, P. S. Role of a finite exposure time on measuring an elastic modulus using microrheology. *Phys Rev E Stat Nonlin Soft Matter Phys* **71**, 041106, doi:10.1103/PhysRevE.71.041106 (2005).
- 198 Savin, T. & Doyle, P. S. Static and dynamic errors in particle tracking microrheology. *Biophys J* **88**, 623-638, doi:10.1529/biophysj.104.042457 (2005).
- 199 Neu, M., Fischer, D. & Kissel, T. Recent advances in rational gene transfer vector design based on poly(ethylene imine) and its derivatives. *Journal of Gene Medicine* **7**, 992-1009, doi:10.1002/jgm.773 (2005).
- 200 Smith, S. B., Finzi, L. & Bustamante, C. Direct Mechanical Measurements of the Elasticity of Single DNA-Molecules by Using Magnetic Beads. *Science* **258**, 1122-1126, doi:DOI 10.1126/science.1439819 (1992).
- 201 Strick, T. R., Allemand, J. F., Bensimon, D., Bensimon, A. & Croquette, V. The elasticity of a single supercoiled DNA molecule. *Science* **271**, 1835-1837, doi:DOI 10.1126/science.271.5257.1835 (1996).
- 202 De Vlaminck, I. & Dekker, C. Recent advances in magnetic tweezers. *Annu Rev Biophys* **41**, 453-472, doi:10.1146/annurev-biophys-122311-100544 (2012).
- 203 Noolandi, J., Rousseau, J., Slater, G. W., Turmel, C. & Lalande, M. Self-trapping and anomalous dispersion of DNA in electrophoresis. *Phys Rev Lett* **58**, 2428-2431, doi:10.1103/PhysRevLett.58.2428 (1987).
- 204 Huang, Y. & Pethig, R. Electrode design for negative dielectrophoresis. *Measurement Science and Technology* **2**, 1142-1146, doi:10.1088/0957-0233/2/12/005 (1991).
- 205 Wang, Q. & Moerner, W. E. An Adaptive Anti-Brownian Electrokinetic Trap with Real-Time Information on Single-Molecule Diffusivity and Mobility. *ACS Nano* **5**, 5792-5799 (2011).
- 206 Cohen, A. E. & Fields, A. P. The Cat That Caught the Canary: What To Do with Single-Molecule Trapping. *ACS Nano* **5**, 5296-5299 (2011).
- 207 Rahman, M., Stott, M. A., Li, Y., Hawkins, A. R. & Schmidt, H. Single-particle analysis with 2D electro-optical trapping on an integrated optofluidic device. *Optica* **5**, doi:10.1364/optica.5.001311 (2018).
- 208 Banterle, N. & Lemke, E. A. Nanoscale devices for linkerless long-term single-molecule observation. *Curr Opin Biotechnol* **39**, 105-112, doi:10.1016/j.copbio.2016.02.013 (2016).
- 209 Mahshid, S. *et al.* Development of a platform for single cell genomics using convex lens-induced confinement. *Lab Chip* **15**, 3013-3020, doi:10.1039/c5lc00492f (2015).
- 210 Leslie, S. R., Fields, A. P. & Cohen, A. E. Convex Lens-Induced Confinement for Imaging Single Molecules. *Analytical Chemistry* **82**, 6224-6229 (2010).
- 211 Gerspach, M. A., Mojarad, N., Sharma, D., Pfohl, T. & Ekinici, Y. Nanofluidic lab-on-a-chip trapping devices for screening electrostatics in concentration gradients. *Microelectronic Engineering* **175**, 17-22, doi:10.1016/j.mee.2016.12.017 (2017).
- 212 Tae Kim, J., Spindler, S. & Sandoghdar, V. Scanning-aperture trapping and manipulation of single charged nanoparticles. *Nat Commun* **5**, 3380, doi:10.1038/ncomms4380 (2014).
- 213 Ruggeri, F. & Krishnan, M. Entropic Trapping of a Singly Charged Molecule in Solution. *Nano Lett* **18**, 3773-3779, doi:10.1021/acs.nanolett.8b01011 (2018).

- 214 Conlisk, A. T. *Essentials of Micro- and Nanofluidics: With Applications to the Biological and Chemical Sciences*. (Cambridge University Press, 2013).
- 215 Johnston, I. D., McCluskey, D. K., Tan, C. K. L. & Tracey, M. C. Mechanical characterization of bulk Sylgard 184 for microfluidics and microengineering. *Journal of Micromechanics and Microengineering* **24**, 035017, doi:10.1088/0960-1317/24/3/035017 (2014).
- 216 Michael Adrian Gerspach, N. M., Deepika Sharma, Yasin Ekinci, and Thomas Pfohl. Pneumatically Controlled Nanofluidic Devices for Contact-Free Trapping and Manipulation of Nanoparticles. *Particle & Particle System Characterization*, 1800161, doi:10.1002/ppsc.201800161 (2018).
- 217 Seo, S. *et al.* Performance evaluation of environmentally benign nonionic biosurfactant for enhanced oil recovery. *Fuel* **234**, 48-55, doi:10.1016/j.fuel.2018.06.111 (2018).
- 218 Mastiani, M., Seo, S., Mosavati, B. & Kim, M. High-Throughput Aqueous Two-Phase System Droplet Generation by Oil-Free Passive Microfluidics. *ACS Omega* **3**, 9296-9302, doi:10.1021/acsomega.8b01768 (2018).
- 219 Wang, Z., Volinsky, A. A. & Gallant, N. D. Crosslinking effect on polydimethylsiloxane elastic modulus measured by custom-built compression instrument. *Journal of Applied Polymer Science* **131**, n/a-n/a, doi:10.1002/app.41050 (2014).
- 220 Andreeva, D. V., Fix, D., Möhwald, H. & Shchukin, D. G. Buffering polyelectrolyte multilayers for active corrosion protection. *Journal of Materials Chemistry* **18**, doi:10.1039/b801314d (2008).
- 221 Cho, J. & Caruso, F. Investigation of the interactions between ligand-stabilized gold nanoparticles and polyelectrolyte multilayer films. *Chemistry of Materials* **17**, 4547-4553, doi:10.1021/cm050972b (2005).
- 222 Poptoshev, E. & Claesson, P. M. Forces between Glass Surfaces in Aqueous Polyethylenimine Solutions. *Langmuir* **18**, 2590-2594 (2002).
- 223 Chen, Z., Lv, Z., Sun, Y., Chi, Z. & Qing, G. Recent advancements in polyethyleneimine-based materials and their biomedical, biotechnology, and biomaterial applications. *J Mater Chem B* **8**, 2951-2973, doi:10.1039/c9tb02271f (2020).
- 224 Al-Khatib, O. *et al.* Adsorption of polyelectrolytes onto the oppositely charged surface of tubular J-aggregates of a cyanine dye. *Colloid and Polymer Science* **297**, 729-739, doi:10.1007/s00396-019-04487-5 (2019).
- 225 Liu, Y. *et al.* Polyethylenimine-grafted multiwalled carbon nanotubes for secure noncovalent immobilization and efficient delivery of DNA. *Angew Chem Int Ed Engl* **44**, 4782-4785, doi:10.1002/anie.200500042 (2005).
- 226 Virgen-Ortiz, J. J. *et al.* Polyethylenimine: a very useful ionic polymer in the design of immobilized enzyme biocatalysts. *J Mater Chem B* **5**, 7461-7490, doi:10.1039/c7tb01639e (2017).
- 227 Overbeek, J. T. G. The role of energy and entropy in the electrical double layer. *Colloids and Surfaces* **51** (1990).
- 228 Sharma, D., Lim, R. Y. H., Pfohl, T. & Ekinci, Y. Optimization of Nanofluidic Devices for Geometry-Induced Electrostatic Trapping. *Particle & Particle Systems Characterization* **38**, doi:10.1002/ppsc.202000275 (2021).

- 229 Wong, W. P. & Halvorsen, K. The effect of integration time on fluctuation measurements: calibrating an optical trap in the presence of motion blur. *Optics Express* **14** (2006).
- 230 Jin, S., Haggie, P. M. & Verkman, A. S. Single-particle tracking of membrane protein diffusion in a potential: simulation, detection, and application to confined diffusion of CFTR Cl⁻ channels. *Biophys J* **93**, 1079-1088, doi:10.1529/biophysj.106.102244 (2007).
- 231 Kirby, B. J. & Hasselbrink, E. F., Jr. Zeta potential of microfluidic substrates: 2. Data for polymers. *Electrophoresis* **25**, 203-213, doi:10.1002/elps.200305755 (2004).
- 232 Sze, A., Erickson, D., Ren, L. & Li, D. Zeta-potential measurement using the Smoluchowski equation and the slope of the current–time relationship in electroosmotic flow. *J Colloid Interf Sci* **261**, 402-410, doi:10.1016/s0021-9797(03)00142-5 (2003).
- 233 Delgado, A. V., González-Caballero, F., Hunter, R. J., Koopal, L. K. & Lyklema, J. Measurement and Interpretation of Electrokinetic Phenomena (IUPAC Technical Report). *Pure and Applied Chemistry* **77**, 1753-1805, doi:10.1351/pac200577101753 (2005).
- 234 Overbeek, J. T. G. The role of energy and entropy in the electrical double layer. *Colloids and Surfaces* **51**, 61-75 (1990).
- 235 Stigter, D. Evaluation of the counterion condensation theory of polyelectrolytes. *Biophysical Journal* **69**, 380-388, doi:[https://doi.org/10.1016/S0006-3495\(95\)79910-6](https://doi.org/10.1016/S0006-3495(95)79910-6) (1995).
- 236 Sharma, D., Lim, R. Y. H., Pfohl, T. & Ekinici, Y. Surface-Modified Elastomeric Nanofluidic Devices for Single Nanoparticle Trapping. *Microsystems & Nanoengineering* (2021).
- 237 Napoli, M., Eijkel, J. C. & Pennathur, S. Nanofluidic technology for biomolecule applications: a critical review. *Lab Chip* **10**, 957-985, doi:10.1039/b917759k (2010).
- 238 Lee, P. J., Hung, P. J., Shaw, R., Jan, L. & Lee, L. P. Microfluidic application-specific integrated device for monitoring direct cell-cell communication via gap junctions between individual cell pairs. *Applied Physics Letters* **86**, doi:10.1063/1.1938253 (2005).
- 239 Soler, M. *et al.* Multiplexed nanoplasmonic biosensor for one-step simultaneous detection of *Chlamydia trachomatis* and *Neisseria gonorrhoeae* in urine. *Biosens Bioelectron* **94**, 560-567, doi:10.1016/j.bios.2017.03.047 (2017).
- 240 Fu, J., Schoch, R. B., Stevens, A. L., Tannenbaum, S. R. & Han, J. A patterned anisotropic nanofluidic sieving structure for continuous-flow separation of DNA and proteins. *Nat Nanotechnol* **2**, 121-128, doi:10.1038/nnano.2006.206 (2007).
- 241 Krishnan, M., Monch, I. & Schwille, P. Spontaneous stretching of DNA in a two-dimensional nanoslit. *Nano Letters* **7**, 1270-1275, doi:10.1021/nl0701861 (2007).
- 242 Hamblin, M. N. *et al.* Selective trapping and concentration of nanoparticles and viruses in dual-height nanofluidic channels. *Lab Chip* **10**, 173-178, doi:10.1039/b916746c (2010).
- 243 Chen, L., Wang, T. & Tong, J. Application of derivatized magnetic materials to the separation and the preconcentration of pollutants in water samples. *TrAC Trends in Analytical Chemistry* **30**, 1095-1108, doi:10.1016/j.trac.2011.02.013 (2011).

- 244 Zhao, X., Shi, Y., Cai, Y. & Mou, S. Cetyltrimethylammonium Bromide-Coated Magnetic Nanoparticles for the Preconcentration of Phenolic Compounds from Environmental Water Samples. *Environmental Science & Technology* **42**, 1201-1206 (2008).
- 245 Dong, Y. L. *et al.* Preparation of guanidine group functionalized magnetic nanoparticles and the application in preconcentration and separation of acidic protein. *J Nanosci Nanotechnol* **11**, 10387-10395, doi:10.1166/jnn.2011.5014 (2011).
- 246 Smith, J. E., Sapsford, K. E., Tan, W. & Ligler, F. S. Optimization of antibody-conjugated magnetic nanoparticles for target preconcentration and immunoassays. *Anal Biochem* **410**, 124-132, doi:10.1016/j.ab.2010.11.005 (2011).
- 247 Kim, S. M., Burns, M. A. & Hasselbrink, E. F. Electrokinetic Protein Preconcentration Using a Simple Glass/Poly(dimethylsiloxane) Microfluidic Chip. *Analytical Chemistry* **78**, 4779-4785 (2006).
- 248 Stroink, T., Paarlberg, E., Waterval, J. C. M., Bult, A. & Underberg, W. J. M. On-line sample preconcentration in capillary electrophoresis, focused on the determination of proteins and peptides. *Electrophoresis* **22**, 2374 - 2382 (2001).
- 249 Sykora, D. *et al.* Application of gold nanoparticles in separation sciences. *J Sep Sci* **33**, 372-387, doi:10.1002/jssc.200900677 (2010).
- 250 Sitko, R., Zawisza, B. & Malicka, E. Modification of carbon nanotubes for preconcentration, separation and determination of trace-metal ions. *TrAC Trends in Analytical Chemistry* **37**, 22-31, doi:10.1016/j.trac.2012.03.016 (2012).
- 251 Johnson-Chavarria, E. M., Tanyeri, M. & Schroeder, C. M. A Microfluidic-based Hydrodynamic Trap for Single Particles. *Jove-J Vis Exp*, doi:UNSP e2517 10.3791/2517 (2011).
- 252 Carlo, D. D., Aghdam, N. & Lee, L. P. Single-Cell Enzyme Concentrations, Kinetics, and Inhibition Analysis Using High-Density Hydrodynamic Cell Isolation Arrays. *Analytical Chemistry* **78**, 4925-4930 (2006).
- 253 Ahmad Khalili, A. *et al.* A Microfluidic Device for Hydrodynamic Trapping and Manipulation Platform of a Single Biological Cell. *Applied Sciences* **6**, doi:10.3390/app6020040 (2016).
- 254 Rettig, J. R. & Folch, A. Large-scale single-cell trapping and imaging using microwell arrays. *Analytical Chemistry* **77**, 5628-5634, doi:10.1021/ac0505977 (2005).
- 255 Tan, W. H. & Takeuchi, S. A trap-and-release integrated microfluidic system for dynamic microarray applications. *Proc Natl Acad Sci U S A* **104**, 1146-1151, doi:10.1073/pnas.0606625104 (2007).
- 256 Tayebi, M., Zhou, Y., Tripathi, P., Chandramohanadas, R. & Ai, Y. Exosome Purification and Analysis Using a Facile Microfluidic Hydrodynamic Trapping Device. *Anal Chem* **92**, 10733-10742, doi:10.1021/acs.analchem.0c02006 (2020).
- 257 Narayanamurthy, V., Nagarajan, S., Firus Khan, A. a. Y., Samsuri, F. & Sridhar, T. M. Microfluidic hydrodynamic trapping for single cell analysis: mechanisms, methods and applications. *Anal Methods-Uk* **9**, 3751-3772, doi:10.1039/c7ay00656j (2017).
- 258 Luan, Q., Macaraniag, C., Zhou, J. & Papautsky, I. Microfluidic systems for hydrodynamic trapping of cells and clusters. *Biomicrofluidics* **14**, 031502, doi:10.1063/5.0002866 (2020).

- 259 Pariset, E. *et al.* Anticipating Cutoff Diameters in Deterministic Lateral Displacement (DLD) Microfluidic Devices for an Optimized Particle Separation. *Small* **13**, doi:10.1002/sml.201701901 (2017).
- 260 McGrath, J., Jimenez, M. & Bridle, H. Deterministic lateral displacement for particle separation: a review. *Lab Chip* **14**, 4139-4158, doi:10.1039/c4lc00939h (2014).
- 261 Byram, C., Moram, S. S. B. & Soma, V. R. SERS based detection of multiple analytes from dye/explosive mixtures using picosecond laser fabricated gold nanoparticles and nanostructures. *Analyst* **144**, 2327-2336, doi:10.1039/c8an01276h (2019).
- 262 Ankamwar, B., Sur, U. K. & Das, P. SERS study of bacteria using biosynthesized silver nanoparticles as the SERS substrate. *Anal Methods-Uk* **8**, 2335-2340, doi:10.1039/c5ay03014e (2016).
- 263 Xiao, L., Wei, L., He, Y. & Yeung, E. S. Single Molecule Biosensing Using Color Coded Plasmon Resonant Metal Nanoparticles. *Analytical Chemistry* **82**, 6308-6314 (2010).
- 264 Sooraj, K. P., Ranjan, M., Rao, R. & Mukherjee, S. SERS based detection of glucose with lower concentration than blood glucose level using plasmonic nanoparticle arrays. *Appl Surf Sci* **447**, 576-581, doi:10.1016/j.apsusc.2018.04.020 (2018).
- 265 Laing, S., Gracie, K. & Faulds, K. Multiplex in vitro detection using SERS. *Chem Soc Rev* **45**, 1901-1918, doi:10.1039/c5cs00644a (2016).
- 266 David, C., Guillot, N., Shen, H., Toury, T. & de la Chapelle, M. L. SERS detection of biomolecules using lithographed nanoparticles towards a reproducible SERS biosensor. *Nanotechnology* **21**, 475501, doi:10.1088/0957-4484/21/47/475501 (2010).
- 267 Wang, R. *et al.* Highly Sensitive Detection of Hormone Estradiol E2 Using Surface-Enhanced Raman Scattering Based Immunoassays for the Clinical Diagnosis of Precocious Puberty. *ACS Appl Mater Interfaces* **8**, 10665-10672, doi:10.1021/acsami.5b10996 (2016).
- 268 Wang, Y. *et al.* Duplex microfluidic SERS detection of pathogen antigens with nanoyeast single-chain variable fragments. *Anal Chem* **86**, 9930-9938, doi:10.1021/ac5027012 (2014).
- 269 Sturm, J. C., Cox, E. C., Comella, B. & Austin, R. H. Ratchets in hydrodynamic flow: more than waterwheels. *Interface Focus* **4**, 20140054, doi:10.1098/rsfs.2014.0054 (2014).
- 270 Jauffred, L., Samadi, A., Klingberg, H., Bendix, P. M. & Oddershede, L. B. Plasmonic Heating of Nanostructures. *Chem Rev* **119**, 8087-8130, doi:10.1021/acs.chemrev.8b00738 (2019).
- 271 Zhou, W. *et al.* Gold Nanoparticle Aggregation-Induced Quantitative Photothermal Biosensing Using a Thermometer: A Simple and Universal Biosensing Platform. *Anal Chem* **92**, 2739-2747, doi:10.1021/acs.analchem.9b04996 (2020).
- 272 Capocefalo, A. *et al.* Exploring the Potentiality of a SERS-Active pH Nano-Biosensor. *Front Chem* **7**, 413, doi:10.3389/fchem.2019.00413 (2019).
- 273 Strankowski, M., Włodarczyk, D., Piszczyk, Ł. & Strankowska, J. Polyurethane Nanocomposites Containing Reduced Graphene Oxide, FTIR, Raman, and XRD Studies. *Journal of Spectroscopy* **2016**, 1-6, doi:10.1155/2016/7520741 (2016).
- 274 Larkin, P. in *Infrared and Raman Spectroscopy* 1-5 (2011).

- 275 Duda, V. I., Suzina, N. E., Polivtseva, V. N. & Boronin, A. M. Ultramicrobacteria: Formation of the concept and contribution of ultramicrobacteria to biology. *Microbiology* **81**, 379-390, doi:10.1134/s0026261712040054 (2012).
- 276 Liu, J. *et al.* Occurrence and Fate of Ultramicrobacteria in a Full-Scale Drinking Water Treatment Plant. *Front Microbiol* **9**, 2922, doi:10.3389/fmicb.2018.02922 (2018).
- 277 Larsen, B. & Hwang, J. Mycoplasma, Ureaplasma, and adverse pregnancy outcomes: a fresh look. *Infect Dis Obstet Gynecol* **2010**, doi:10.1155/2010/521921 (2010).
- 278 Sweet, R. L. & Gibbs, R. S. *Infectious diseases of the female genital tract*. (Lippincott Williams & Wilkins, 2009).
- 279 Heegaard, E. D. & Brown, K. E. Human parvovirus B19. *Clin Microbiol Rev* **15**, 485-505, doi:10.1128/cmr.15.3.485-505.2002 (2002).
- 280 Legendre, M. *et al.* Pandoravirus Celtis Illustrates the Microevolution Processes at Work in the Giant Pandoraviridae Genomes. *Front Microbiol* **10**, 430, doi:10.3389/fmicb.2019.00430 (2019).
- 281 Legendre, M. *et al.* Diversity and evolution of the emerging Pandoraviridae family. *Nat Commun* **9**, 2285, doi:10.1038/s41467-018-04698-4 (2018).
- 282 Larsen, H. Halophilic and halotolerant microorganisms-an overview and historical perspective. *FEMS Microbiology Reviews* **39**, 3-7 (1986).
- 283 Amoozegar, M. A., Safarpour, A., Noghabi, K. A., Bakhtiary, T. & Ventosa, A. Halophiles and Their Vast Potential in Biofuel Production. *Front Microbiol* **10**, 1895, doi:10.3389/fmicb.2019.01895 (2019).
- 284 CHRISTIAN, J. H. B. & WALTHO, J. A. The Sodium and Potassium Content of Non-Halophilic Bacteria in Relation to Salt Tolerance. *Microbiology* **25**, 97-102, doi:<https://doi.org/10.1099/00221287-25-1-97> (1961).
- 285 Margesin, R. & Schinner, F. Potential of halotolerant and halophilic microorganisms for biotechnology. *Extremophiles* **5**, 73-83, doi:10.1007/s007920100184 (2001).
- 286 Larcher, W. *Physiological Plant Ecology*. (Springer, 2001).
- 287 Zheng, X. T. *et al.* On-chip investigation of cell-drug interactions. *Adv Drug Deliv Rev* **65**, 1556-1574, doi:10.1016/j.addr.2013.02.001 (2013).
- 288 Chang, C. C., Wang, Z., Sheng, Y. J. & Tsao, H. K. Nanostructure collapse by elasto-capillary instability. *Soft Matter* **10**, 8542-8547, doi:10.1039/c4sm01520g (2014).
- 289 Chini, S. F. & Amirfazli, A. Understanding pattern collapse in photolithography process due to capillary forces. *Langmuir* **26**, 13707-13714, doi:10.1021/la101521k (2010).
- 290 Chung, S. *et al.* Smartphone-Based Paper Microfluidic Particulometry of Norovirus from Environmental Water Samples at the Single Copy Level. *ACS Omega* **4**, 11180-11188, doi:10.1021/acsomega.9b00772 (2019).
- 291 Ashiba, H. *et al.* Detection of norovirus virus-like particles using a surface plasmon resonance-assisted fluoroimmunosensor optimized for quantum dot fluorescent labels. *Biosens Bioelectron* **93**, 260-266, doi:10.1016/j.bios.2016.08.099 (2017).

Publications

List of publications in the context of the work presented in this thesis

1. **Sharma D.**, Lim R.Y.H., Pfohl T., Ekinci Y. Surface-Modified Elastomeric Nanofluidic Devices for Single Nanoparticle Trapping. *Microsystems & Nanoengineering* (2021).
2. **Sharma D.**, Lim R.Y.H, Pfohl T., Ekinci Y. Optimization of Nanofluidic Devices for Geometry-Induced Electrostatic Trapping, *Particle & Particle Systems Characterization*, **38**, 2000275 (2021).
3. Gerspach M. A., Mojarad N., **Sharma D.**, Ekinci Y., Pfohl T., Pneumatically Controlled Nanofluidic Devices for Contact-Free Trapping and Manipulation of Nanoparticles, *Particle & Particle Systems Characterization*, 1800161 (2018).
4. Gerspach M. A., Mojarad N., **Sharma D.**, Pfohl T., Ekinci Y., Soft Electrostatic Trapping in Nanofluidics, *Microsystems & Nanoengineering* **3**, 17051 (2017).
5. **Sharma D.**, Gerspach M.A., Pfohl T., Lim R.Y.H, Ekinci Y. Single positively charged particle trapping in nanofluidic systems. *Microelectronic Engineering*, **175**: 43-49 (2017).
6. Gerspach M. A., Mojarad N., **Sharma D.**, Pfohl T., Ekinci Y., Nanofluidic Lab-on-a-chip Trapping Devices for Screening Electrostatics in concentration gradients, *Microelectronic Engineering*, **175**, 17-22 (2017).

Patent in context of the work presented in this thesis

1. **Sharma D.**, Ekinci Y., Device and Method for Size-Selective Particle Separation, Trapping, and Manipulation of Micro and Nanoparticles for Molecular Detection, *European Patent Application*, EP19192141 (2019).

Further publications and conference proceedings of the author

1. Iacono M. I., Neufeld E., Akinagbe E., Bower K., Wolf J., Oikonomidis I. V., **Sharma D.**, Lloyd B., Wilm B. J., Wyss M., et al. MIDA: a multimodal imaging-based detailed anatomical model of the human head and neck. *Plos one* **10**, e0124126 (2015).
2. Neufeld, E., Kyriakou, A., **Sharma, D.** & Kuster, N. Modeling, effect prediction, and planning for EM-and FUS-based thermal treatment in Antennas and Propagation (EuCAP), 2014 8th European Conference on (2014), 1483–1487.
3. Neufeld, E., Iacono, M. I., Akinagbe, E., Wolf, J., Oikonomidis, I. V., **Sharma, D.**, Wilm, B., Wyss, M., Jakob, A., Cohen, E., et al. Computational platform combining detailed and

- precise functionalized anatomical phantoms with EM-Neuron interaction modeling in General Assembly and Scientific Symposium (URSI GASS), 2014 XXXIth URSI (2014), 1–4.
4. Vogiatzis Oikonomidis, I., Neufeld, E., Wolf, J., **Sharma, D.**, Hamnerius, Y. & Kuster, N. Couple Electromagnetic and Neuronal Dynamics Simulation of Gradient Coil Switching Induced Nerve Stimulation in Proceedings: Joint Annual Meeting ISMRM- ESMRMB 2014 SMRT 23rd Annual Meeting 10-16 May, 2014 Milan Italy (2014).
 5. Kaplas, T., **Sharma, D.** & Svirko, Y. Few-layer graphene synthesis on a dielectric substrate. *Carbon* **50**, 1503–1509 (2012).
 6. Kats, M. A., **Sharma, D.**, Lin, J., Genevet, P., Blanchard, R., Yang, Z., Qazilbash, M. M., Basov, D., Ramanathan, S. & Capasso, F. Ultra-thin perfect absorber employing a tunable phase change material. *Applied Physics Letters* **101**, 221101 (2012).
 7. Mishra, D., Singh, A. K., Shyni, P., **Sharma, D.** & Perumal, A. Enhanced soft magnetic properties in multilayer structured amorphous Fe-Ta-C films. *Journal of Applied Physics* **109**, 07A304 (2011).
 8. Dey, K. K., **Sharma, D.**, Basu, S. & Chattopadhyay, A. Veering the motion of a magnetic chemical locomotive in a liquid. *The Journal of Chemical Physics* **129**, 121101 (2008).

Acknowledgements

“A PhD degree is not just a scientific achievement but also a testimony of the journey that one covers with the help of various people in one’s life, both personally and professionally. A journey that cannot be finished without the support of others who are willing to share their knowledge, experiences, time, motivation, and energy with you for your growth.”

I want to express my gratitude to my supervisors, Dr. Yasin Ekinçi and Prof. Dr. Roderick Lim, for allowing me to expand my scientific knowledge and broaden my expertise in the domain that was little known to me when I joined my doctoral studies. Under their supervision and guidance, I have explored multiple disciplines of scientific research ranging from biophysics, surface chemistry, applied physics, nanofabrication, programming, biosensing, nanofluidics, optics, lithography, particle trapping, etc. The experience helped me to grow both as a scientist on the professional front and as a mature human being on the personal front.

I am grateful to Dr. Thomas Pfohl for his assistance in my scientific journey on micro/nanofluidic devices for particle trapping and his invaluable suggestions, comments, and guidance throughout my PhD. I am thankful to Dr. Celestino Padeste for helping me during my initial phase of the doctoral work on protein patterning and biomimetic nuclear pore complex using state-of-the-art lithography techniques. His knowledge of surface chemistry and his support played a vital role in the direction of my PhD work.

I am thankful to my colleagues from the University of Basel, Dr. Ludovit P. Zweifel, Dr. Kai Schleicher, Dr. Larisa Kapinos, Dr. Philipp Oertle, Dr. Rafael Schoch, Dr. Raphael Wagner, for sharing their experience and knowledge with me and helping me to quick start my research in the field of Biophysics during the first year of my PhD. Additionally, I am grateful to Chantal Rencurel for assisting me in the execution of various lab procedures.

I am thankful to Dr. Michael A. Gerspach for sharing his experience and knowledge in the field of micro/nanofluidics and for being a great team member in our small fluidic research team. His support helped me quickly learn the fluidics field and become an expert in the research area, to work independently.

I am grateful to the Swiss Nanoscience Institute (SNI) for financially supporting this research work and providing me with various opportunities for personal and professional growth. SNI and its members have played a vital role in exposing me to a multidisciplinary research environment and learning from other members of the scientific community. It gave me great scientists to work with and friends for life.

In addition, I am grateful to all my colleagues from the University of Basel, the Swiss Nanoscience Institute (SNI), and the Paul Scherrer Institut, who have made this journey enjoyable and enriching, and all technicians from Biozentrum, University of Basel and LMN,

Acknowledgements

Paul Scherrer Institut for their support throughout my PhD to learn various techniques and methods and to overcome the technical challenges.

This degree would not be possible without the support and contribution of my committee members Dr. Yasin Ekinci, Dr. Roderick Lim, and Dr. Michel Calame. I am highly grateful for their invaluable help, support, and guidance.

Finally, I would like to express my gratitude towards my father, Shri Hari Kishan Sharma, and my mother, Smt. Kaushalya Sharma, my sister Dr. Yogita Sharma, and my husband Dr. Manish Garg, for their constant moral and unwavering support in this journey, irrespective of my parents' hardships due to their critical health issues. Their confidence in me and their strong willpower encouraged me to tackle all ups and downs of this journey. Since childhood, I always dreamt of contributing to research and innovation. The journey of my doctoral studies has made my foundation very strong to continue my journey toward scientific and technical excellence.

"Never stop dreaming; the dream prepares you to start your journey towards your goals and keeps you motivated in the tough time to achieve your targets."

Curriculum Vitae

Ms. DEEPIKA SHARMA

PERSONAL INFORMATION

Date of birth 1st June 1986
Nationality Indian
Hometown Jaipur, Rajasthan, India

EDUCATION

Ph.D.: Nanosciences 2014 – 2018

Paul Scherrer Institut - Villigen, and University of Basel – Basel, Switzerland

Thesis: Development and usage of micro- and nanofluidic devices for nanoparticle trapping, sorting and biosensing.

M.Sc.: Photonics 2010 – 2012

University of Eastern Finland – Joensuu, Finland

Thesis: Chemical vapor deposition of graphene on a dielectric substrate and its characterization.

B.Tech.: Engineering Physics 2006 – 2010

Indian Institute of Technology – Guwahati, India

Thesis: Investigation of temperature dependent magnetic hysteresis of amorphous Fe-Ta-C thin-films and laminated Fe-Ta-C/Ta thin-films.

EXPERIENCES

Product Engineer – Frontend Backend Integration 02/2019 – Present

Hitachi ABB Power Grids – Semiconductors, Lenzburg, Switzerland

ABB – Semiconductors, Lenzburg, Switzerland

Doctoral Student 07/2014 - 10/2018

Laboratory for Micro and Nanotechnology, Paul Scherrer Institut – Villigen, Switzerland

Biozentrum, University of Basel – Basel, Switzerland

Research Associate 07/2013 – 06/2014

IT'IS Foundation, ETH-Zürich, Zürich, Switzerland

Project Assistant Schmid & Partner Engineering AG, Zürich, Switzerland	01/2013 – 05/2013
Visiting Fellow School of Engineering and Applied Sciences, Harvard University – Cambridge, MA, USA	02/2012 – 08/2012
Visiting Student School of Engineering and Applied Sciences, Harvard University – Cambridge, MA, USA	05/2011 – 09/2012
Research Assistant University of Eastern Finland – Joensuu, Finland	09/2010 – 04/2011
Summer Student INRS-Énergie, Matériaux et Télécommunications – Quebec, Canada	05/2009 – 07/2009
Research Assistant Indian Institute of Technology (IIT) – Guwahati, India	05/2007 – 01/2008